FINITE ELEMENT STUDIES

IN INJECTION MOLD FILLING

By

© HARILAOS MAVRIDIS, Dipl. Chem. Eng.

A Thesis

Submitted to the School of Graduate Studies

in Partial Fulfillment of the Requirements

for the Degree

Doctor of Philosophy

McMaster University
April 1988

FINITE ELEMENT STUDIES
IN INJECTION MOLD FILLING

Στους γονείς μου

DOCTOR OF PHILOSOPHY
(Chemical Engineering)

McMASTER UNIVERSITY
Hamilton, Ontario

TITLE: Finite Element Studies in Injection Mold Filling

AUTHOR: Harilaos Mavridis,
Dipl. Chem. Eng. (Aristotle University of Thessaloniki, Greece)

SUPERVISORS: Drs. A.N. Hrymak and J. Vlachopoulos
(Chemical Engineering)

NUMBER OF PAGES: xviii, 182

ABSTRACT

Flow phenomena associated with the injection mold filling process have a significant impact on the microstructure development and hence on the final properties of molded articles. The present work is concerned with the mathematical modeling and numerical simulation of the mold filling process. The aim is to provide in-depth understanding of the flow phenomena involved and investigate their impact on the microstructure of the molded polymer article.

The mold filling process takes place as a rolling-type advancement of the flow front over the mold walls. The flow field behind the advancing flow front is known as fountain flow, and it is the salient feature of mold filling. The fountain flow phenomenon is examined extensively with finite element techniques, both in the steady-state and in the time domain. The u-v-p-h-δ formulation described in the present work is a powerful numerical technique for the simulation of free surface flows, and determines simultaneously the flow field and the free surface shape. Steady-state and transient simulations with Newtonian and shear-thinning fluids in planar and axisymmetric geometries are presented. Various features of fountain flow are described with the aid of velocity vector, pressure, free surface shape, and streamline plots. The general problem of fountain and reverse fountain flow (immiscible liquid displacement) and the collision of two flow fronts to form a weldline are also investigated.

The deformation history experienced by the fluid due to fountain flow is examined on the basis of the numerically computed flow field, by tracking material elements as they move through the flow domain. It is found that material elements from the centerline migrate towards the mold walls, extend in the flow direction and form characteristic V-shapes, fully in agreement with available visualization experiments.

A viscoelastic constitutive equation (multi-mode Leonov model) is introduced in order to investigate the effect of fountain flow on the molecular orientation of injection molded parts, as reflected in available birefringence measurements. A finite element algorithm for the numerical simulation of viscoelastic free surface flows is described. Fountain flow simulations are performed for material properties and processing conditions corresponding to available experiments. Finite element solutions are obtained at high levels of fluid elasticity and they converge with mesh refinement, provided that a slip boundary condition is applied at the wall to alleviate the stress singularities. The finite element results are combined with a simple theory to predict frozen-in stress and birefringence distributions. Computational results are compared to, and agree favorably with, available experimental data. It is demonstrated quantitatively that fountain flow is responsible for the molecular orientation pattern of the surface layer of injection molded parts.

ACKNOWLEDGEMENTS

TABLE OF CONTENTS

TABLE OF CONTENTS (continued)

LIST OF FIGURES

LIST OF FIGURES (continued)

LIST OF TABLES

NOMENCLATURE

a	:	thermal diffusivity, m^2/s
a_T	:	WLF temperature-shift factor, eq. (5.36)
C	:	stress-optical coefficient, Pa^{-1}
C_k	:	elastic strain tensor in the k-mode of the Leonov model
$C_{xx,k}, C_{yy,k}, C_{xy,k}$	:	cartesian components of C_k
C_1, C_2	:	parameters in eq. (5.36)
c_p	:	heat capacity
$d^{(m)}$	:	search direction in the m-th Newton-Raphson iteration
e^i	:	unit vector along the i-th spine
e_x, e_y	:	unit vectors along the x- and y-directions
f	:	function
g	:	gravitational acceleration, m/s^2
g	:	unit vector in the direction of gravity
H	:	half gapwidth
h^i	:	free surface parameter for the i-th spine
h	:	vector of h-parameters
I	:	unit tensor
J	:	Jacobian matrix
k	:	thermal conductivity
ℓ	:	arc length
L	:	mold length
ℓ_j	:	Lagrangian polynomial, defined in eq. (5.34)
L_{stag}	:	length of stagnation flow region
n	:	normal vector
n_x, n_z	:	direction cosines of the normal vector
n	:	refractive index tensor, eq. (5.1)
N	:	number of modes in the Leonov model
N_e	:	number of nodes per element
N_p	:	number of available solutions

NOMENCLATURE (continued)

N_1 : first normal stress difference, eq. (5.8)

N_2 : second normal stress difference, eq. (5.9)

p : parameter, eq. (5.29)

P : pressure

Q_k : auxiliary variable, defined in eq. (5.10)

r : radial coordinate

R : tube radius

R_1, R_2 : radii of curvature of the free surface

R : vector of residuals

R_c^i : continuity residual

R_{CE}^i : constitutive equation residual

R_k^i : kinematic residual at the free surface

R_m^i : momentum residual

R_{mx}^i, R_{my}^i : x- and y- momentum residuals

R_δ^i : residual for δ-variables

s : rheological parameter in the Leonov model

S_μ : auxiliary variable, defined in eq. (2.9c)

t : time

t : tangential vector at the free surface

T : temperature

T_i : injection temperature

T_{ref} : reference temperature

T_w : wall temperature

T_0 : measurement temperature of rheological properties

u : x- or z- velocity component

U : average velocity

u_{avg} : y-averaged x-velocity

u_s : slip velocity

u_x : $\partial u/\partial x$

u_y : $\partial u/\partial y$

NOMENCLATURE (continued)

v	:	y-velocity component
V	:	velocity vector
Vi	:	nodal velocity vector
v_x	:	$\partial v/\partial x$
v_y	:	$\partial v/\partial y$
x	:	x-coordinate direction
x —	:	position vector
X	:	vector of unknowns
X	:	position from gate
x_{FT}	:	x-coordinate of front tip
x_{CL}	:	x-coordinate of contact line
x_ξ	:	$\partial x/\partial \xi$
x_η	:	$\partial x/\partial \eta$
y	:	y-coordinate direction
y_ξ	:	$\partial y/\partial \xi$
y_η	:	$\partial y/\partial \eta$
y	:	vector of time dependent variables
y^j	:	vector of time dependent variables at time t_j
$\dot{y}^j$	:	vector of time derivatives at time t_j
y_c^j	:	corrector at t_j
y_p^j	:	predictor at t_j
z	:	z-coordinate direction
z_{CL}	:	z-coordinate of contact line
z_{FT}	:	z-coordinate of front tip
z_{st}	:	distance between stagnation points
$\underline{w}$	:	velocity in the z-cartesian direction
w_{avg}	:	y-averaged z-velocity
W	:	width of mold

Greek Symbols

α	:	step length in line search

NOMENCLATURE (continued)

β	:	slip coefficient, m/Pa/s
γ	:	surface tension
$\dot{\gamma}$	:	shear rate
δ	:	spine orientation angle
Δn	:	birefringence, defined in eq. (5.2)
ΔP	:	pressure drop
Δt_j	:	time step size
$\Delta(y^j)$	:	truncation error, eq. (4.22)
ε	:	tolerance
$\dot{\varepsilon}_{11}$	:	deformation rate, eq. (3.37)
η	:	local coordinate in the parent finite element
η_x	:	$\partial\eta/\partial x$
η_y	:	$\partial\eta/\partial y$
η_0, η_k	:	shear viscosities in Leonov model
θ	:	contact angle
θ_k	:	relaxation time in Leonov model
λ	:	time constant in Carreau model
μ, μ_0	:	viscosity and reference viscosity
ξ	:	local coordinate in the parent finite element
ξ_x	:	$\partial\xi/\partial x$
ξ_y	:	$\partial\xi/\partial y$
π^i	:	pressure basis function
ρ	:	density
σ	:	total stress tensor
τ	:	deviatoric stress tensor
ϕ^i	:	velocity basis function
Φ	:	modified pressure, eq. (2.17a)
χ	:	parameter in time-step control, eq. (4.23)
ψ	:	streamfunction
Ω	:	flow domain
$\partial\Omega$	:	boundary of flow domain

NOMENCLATURE (continued)

Superscripts

i	:	index
j	:	index
(m)	:	iteration number
T	:	transpose

Subscripts

B	:	base point
CL	:	contact line
F	:	free surface
m	:	momentum
w	:	wall

Overscripts

$\bullet$	:	time derivative
∇	:	upper convected derivative, eq. (5.6)

Dimensionless Groups

B	:	$\beta\mu/H$, measure of slip
Ca	:	capillary number, $\mu U/\gamma$
Re	:	Reynolds number, $\rho UH/\mu$
S^{-1}	:	inverse Stokes number, $\rho g H^2/\mu U$
S_R	:	Stress ratio, defined in eq. (5.37)
Ws	:	Weissenberg number, defined in eq. (5.38)

CHAPTER 1

INTRODUCTION

1.1   The Injection Molding Process

Injection molding is a major polymer processing operation for producing identical articles from a hollow mold. It is an intermittent cyclic process with the following steps: (i) filling stage: a polymer melt is injected into the cold-walled cavity where it spreads under the action of high pressures and fills the mold; (ii) packing stage: high back pressures are maintained after the mold is filled, and additional melt flows into the mold to compensate for density changes (shrinkage) during cooling and ensure accurate reproduction of the mold shape; and (iii) cooling stage: the melt is cooled, and the shaped article is ejected. Further background material on the overall injection-molding process is provided in standard texts (Middleman, 1977; Tadmor & Gogos, 1979; Pearson, 1985).

The filling stage is the most important and complex step of the injection molding cycle. A simple rectangular mold is shown in Figure 1.1. The top view or spreading plane is given in Figure 1.1a. Fluid is injected from the gate and fills the mold advancing to the right. The contours indicate successive flow front positions in the spreading plane. The flow in the transverse plane is shown in Figure 1.1b. As is usually the case, the thickness is much smaller than the other dimensions of the mold. Commercial molds may be highly complex geometrically and involve multiple gates. However, single-gated rectangular and circular molds have been used in both experimental and theoretical work for analytical convenience. The hot melt solidifies as it touches the cold walls forming a "frozen skin". Under severe conditions the frozen polymer may block the flow and the mold will not be filled (short shot). Gate design, among other factors, is crucial for preventing short shots.

(a)

(b)
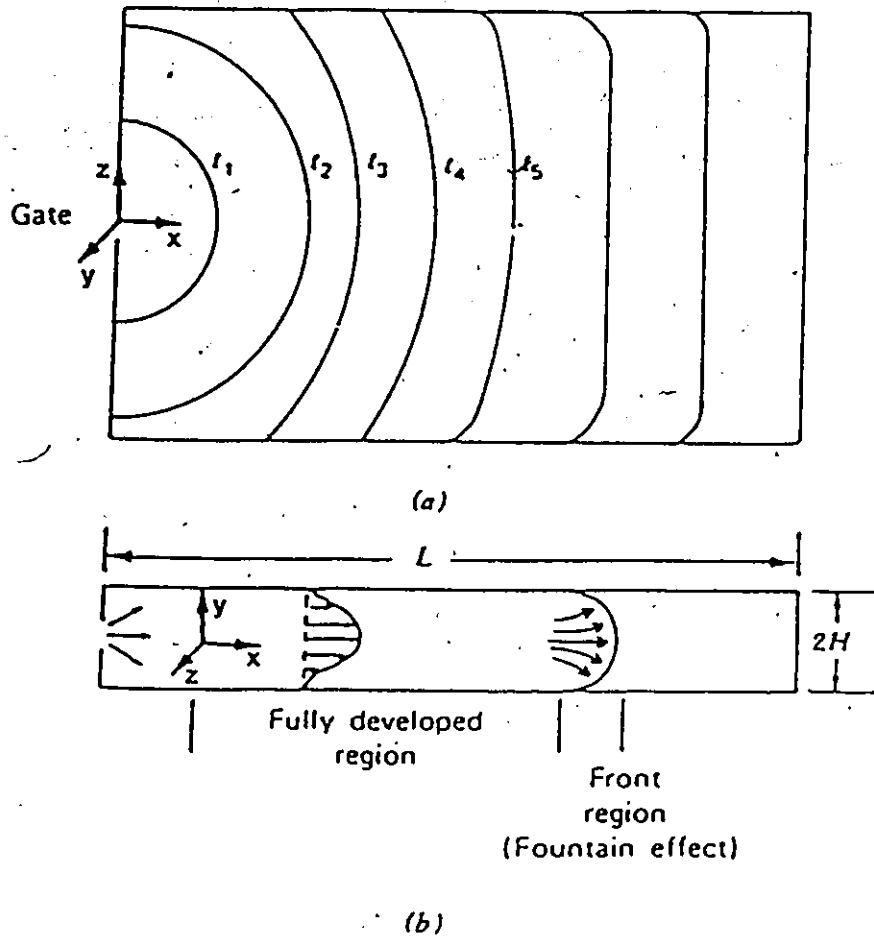
Figure 1.1   Schematic representation of single-gated rectangular cavity:
(a)   top view (spreading plane);
(b)   side view (transverse plane)

As the melt spreads in the mold cavity, air is displaced through the vents. Vents should be placed in positions reached last by the melt, and this requires knowledge about the progression of the flow front. The spreading pattern is also required for the prediction of weldline location. Weldlines, also known as knit lines, result from the meeting of multiple flows injected through separate gates and/or from the recombination of a single flow divided by passage around an insert, for example. In general, both the surface appearance and mechanical properties of the molded articles are affected by the knitting process. The dominant factor affecting the physical, mechanical and optical properties of the article is the microstructure development in the final part (morphology for semicrystalline and molecular orientation for amorphous polymers). Injection molded articles exhibit anisotropic properties associated with their anisotropic microstructure and which originate in the widely different thermal and deformation history experienced by each material particle at different locations of the mold. Recent reviews of microstructure development in semicrystalline and amorphous polymers are offered by Katti & Schultz (1982) and Isayev (1983) respectively.

A comprehensive mathematical model combining (i) mold design and molding conditions, (ii) rheological and physical properties of the polymer melt, (iii) conservation equations for mass, momentum and energy, and (iv) a theory of microstructure development, must be able, in principle, to give a complete picture of the injection molding process. The predictive objective of the mathematical modeling procedure can be conveniently classified into two categories: (i) large scale phenomena: overall quantities that comprise the minimum amount of information necessary to provide a gross design factor (e.g., fill time, pressure drop, cooling requirements); (ii) small scale phenomena: this includes weldline location and molecular orientation distribution and requires detailed information about the spreading pattern, temperature, velocity and stress fields.

The present work concentrates on small scale phenomena. The aim is to provide in-depth understanding of the flow-phenomena associated with the mold filling process, and investigate their interaction with the microstructure development in the final part.

1.2   Objectives

The purpose of this thesis is to develop the mathematical and computer tools that will enable the numerical simulation of mold filling. The objective is to obtain fundamental understanding of the flow phenomena associated with mold filling and their impact on the microstructure development of injection molded parts.

The fluid mechanics of the advancing flow front, known as "fountain flow", is identified as the salient feature of the mold filling process. Efficient finite element techniques are presented that allow simulation of two-dimensional flows of Newtonian, shear-thinning and viscoelastic fluids with a free front, both in the steady-state and in the time domain. Numerical tracking of fluid elements illustrates the deformation experienced by the fluid due to fountain flow. Predictions of frozen-in flow birefringence quantify the impact of mold filling on the molecular orientation of injection molded parts and provide insight into the interrelationship of processing conditions and anisotropic microstructure of injection moldings.

1.3   Thesis Outline

Chapter 2: This chapter describes the implications and the problems related to the mathe-matical modeling of mold filling. It also contains a critical literature survey of the available mathematical and computer-aided techniques for modeling and analysis of mold filling.

Chapter 3: A finite element technique is described for the numerical simulation of viscous free surface flows. The numerical technique is applied to study the fluid mechanics of the

advancing flow front (fountain flow) in the steady state. Newtonian and shear-thinning fluids are considered in planar and axisymmetric geometries. Numerical tracking of material elements is employed to investigate the deformation experienced by the fluid. The general case of two immiscible fluids displacing each other inside a capillary is also examined.

Chapter 4: In this chapter we investigate the transient free surface flows encountered in injection mold filling. A finite element technique suitable for this class of problems is presented and is applied to study the start-up flow of a fluid with a free front, and the collision of two flow fronts to form a weldline.

Chapter 5: In this chapter we investigate the impact of fountain flow on the molecular orientation of injection molded parts. The viscoelasticity of the polymer melt is accounted for with the multi-mode Leonov model. A finite element technique for viscoelastic free surface flows is developed and is applied on the fountain flow problem. The finite element results are combined with a simple theory to predict frozen-in flow birefringence in molded parts. Computational results are compared to available experimental measurements. The effect of fountain flow is clearly demonstrated.

Chapter 6: This chapter summarizes the main results of this thesis and offers some recommendations for future work.

CHAPTER 2

REVIEW OF MATHEMATICAL MODELING

OF INJECTION MOLD FILLING

2.1   Introduction

The fluid mechanics and heat transfer of the injection mold filling stage can be

described by the general conservation equation for mass, momentum and energy:

$$\frac{\partial \rho}{\partial t} + \nabla \cdot (\rho \mathbf{V}) = 0 \qquad\qquad (2.1)$$

$$\rho \left(\frac{\partial \mathbf{V}}{\partial t} + \mathbf{V} \cdot \nabla \mathbf{V} \right) = -\nabla P + \nabla \cdot \tau + \rho \mathbf{g} \qquad\qquad (2.2)$$

$$\rho c_p \left(\frac{\partial T}{\partial t} + \mathbf{V} \cdot \nabla T \right) = \nabla \cdot (k \nabla T) + \tau : \nabla \mathbf{V} \qquad\qquad (2.3)$$

The convective terms in the momentum equation, eq. (2.2), are negligible for polymer melt

flows (creeping flow). Compressibility effects may be present due to the large pressure

variations involved in injection molding. However, it is believed (Tadmor & Gogos, 1979) that

the incompressibility assumption introduces negligible error.

After substituting the appropriate constitutive equation for the deviatoric stress

tensor τ, and imposing the boundary conditions, we have a transient, non-isothermal, three-

dimensional problem with an advancing flow front. Various complicating features of physical

and mathematical nature arise in the above problem:

(i)   Constitutive Equation: the system is not closed until the appropriate constitutive

equation relating stress to the rate-of-strain is introduced. Polymer melts are

shear thinning viscoelastic fluids, and the development of constitutive equations

for this class of fluids is still an active area of research. Recent advances in this area are reviewed in Huilgol & Phan-Thien (1986). The numerical problems associated with the simulation of viscoelastic flows are discussed by Keunings (1987).

(ii)   <u>Non-isothermal flow and freezing at the wall:</u> the mold walls are held at a temperature below the solidification temperature of the polymer. Hot polymer solidifies upon touching the mold walls forming a "frozen skin". This introduces an additional unknown interface (hot melt-solidified polymer) in the flow domain.

(iii)   <u>Unsteady flow, geometric complexity and moving flow front:</u> the flow front (free boundary) location is unknown a priori and must be determined along with the field variables as a solution to the governing nonlinear partial differential equations. The flow front advances in complex three-dimensional regions where splitting and knitting of flow fronts may take place. The physics of fluid/gas interfaces moving over solid boundaries is poorly understood. Modeling the fluid as a continuum along with the no-slip condition at the wall breaks down in the vicinity of the contact line, i.e. the fluid/gas/solid intersection (Huh & Scriven, 1971; Dussan, 1979).

It is readily seen that the most general formulation of injection mold filling results in a very large and complex mathematical problem. All the mathematical models that have appeared thus far either focus on a specific subset of the general problem or involve major simplifications related to the complicating features discussed above. These models are reviewed in the next section.

2.2   Survey of Mathematical Models

2.2.1   Early studies – Unidirectional Models

The first systematic studies on injection molding were introduced by Spencer and Gilmore (Gilmore & Spencer, 1950; Spencer & Gilmore, 1950; Gilmore & Spencer, 1951; Spencer & Gilmore, 1951) and were concerned with flow visualization of mold filling, modeling of the fluid mechanics of the process, pressure and temperature variations during the molding cycle, and orientation and residual stresses in molded parts. In their mold filling studies they considered a simple one-dimensional model and fitted a power-law-type equation relating filling time to the applied pressure drop.

A second generation of studies were presented by Ballman and co-workers (Ballman et al. 1959a,b,c; Ballman & Shusman, 1959; Ballman & Toor, 1960; Toor et al, 1960) including the first non-isothermal modeling of mold filling in thin rectangular cavities and the first computer application for predictive calculations. They also reported experimental measurements and a theory of molecular orientation development in injection molded parts. The effect of mold design and process conditions on the resulting orientation distribution and the effects of orientation on the physical properties of injection moldings were studied.

Pearson (1966) presented a non-isothermal model and proposed a finite-difference solution for the mold filling of a center-gated circular disk. Further computer simulations and experimental studies were presented later by Kamal & Kenig (1972a,b), Berger & Gogos (1973), Wu et al (1974), Williams & Lord (1975), and Lord & Williams (1975). A similar model for rectangular thin cavities was considered in the studies of Harry & Parrott (1970) and Thienel & Menges (1978). Isayev & Hieber (1980) studied an idealized mold filling problem with a viscoelastic constitutive equation.

2.2.2   Two-dimensional models

2.2.2.1   Spreading Plane. Hele-Shaw Approximation

Richardson (1972) suggested that Hele-Shaw flow theory (Schlichting, 1960) may be applied in many mold cavities with large aspect ratios. This approximation reduces the original set of equations considerably, and it has been the basis of the two-dimensional models that appeared in the last decade for modeling the flow in the spreading plane. The formulation given below follows that of Hieber & Shen (1980) and Shen (1984).

Consider the non-isothermal flow of an inelastic generalized Newtonian fluid in a thin gap of arbitrary planar form. The gap thickness 2H in the y-direction is much smaller than the other dimensions, and symmetry is assumed on the center plane. With the Hele-Shaw approximation the mass and momentum equations reduce to:

$$\frac{\partial}{\partial x}\left(H \, u_{avg}\right) + \frac{\partial}{\partial z}\left(H \, w_{avg}\right) = 0 \qquad \qquad \cdot(2.4)$$

$$0 = \frac{\partial}{\partial y}\left(\mu \frac{\partial u}{\partial y}\right) - \frac{\partial P}{\partial x} \qquad \qquad (2.5a)$$

$$0 = \frac{\partial}{\partial y}\left(\mu \frac{\partial w}{\partial y}\right) - \frac{\partial P}{\partial z} \qquad \qquad (2.5b)$$

where u_{avg} and w_{avg} denote the gapwise-average velocities in the x- and z-directions respectively (cf. Figure 1.1). For a generalized Newtonian fluid the viscosity is:

$$\mu = \mu(T, \dot{\gamma}) \qquad \qquad (2.6)$$

where

$$\dot{\gamma} = \left[\left(\frac{\partial u}{\partial y}\right)^2 + \left(\frac{\partial w}{\partial y}\right)^2\right]^{1/2} \qquad \qquad (2.7)$$

Applying the no-slip condition at the wall and symmetry at the centerplane (y = H and y = 0 respectively), eqs. (2.5a,b) give:

$$u(y) = -\frac{\partial P}{\partial x} \int_y^H \frac{y'}{\mu} \, dy' \qquad (2.8a)$$

$$w(y) = -\frac{\partial P}{\partial z} \int_y^H \frac{y'}{\mu} \, dy' \qquad (2.8b)$$

and the average velocities are:

$$u_{avg} = \frac{1}{H} \int_0^H u \, dy = -\frac{\partial P}{\partial x} \frac{S_\mu}{H} \qquad (2.9a)$$

$$w_{avg} = \frac{1}{H} \int_0^H w \, dy = -\frac{\partial P}{\partial z} \frac{S_\mu}{H} \qquad (2.9b)$$

where

$$S_\mu = \int_0^H \frac{y^2}{\mu} \, dy \qquad (2.9c)$$

Substituting eqs. (2.9a,b) into eq. (2.4):

$$\frac{\partial}{\partial x}\left(S_\mu \frac{\partial P}{\partial x}\right) + \frac{\partial}{\partial z}\left(S_\mu \frac{\partial P}{\partial z}\right) = 0 \qquad (2.10)$$

This equation is solved along with the simplified energy equation:

$$\rho c_p\left(\frac{\partial T}{\partial t} + u\frac{\partial T}{\partial x} + w\frac{\partial T}{\partial z}\right) = \frac{\partial}{\partial y}\left(k\frac{\partial T}{\partial y}\right) + \mu \dot{\gamma}^2 \qquad (2.11)$$

The boundary conditions for eq. (2.10) require that at the inflow boundaries the pressure or the normal pressure gradient must be specified. At solid walls the condition of zero normal velocity requires the normal pressure gradient to be zero. At the flow front the pressure must be constant (set to zero as the pressure level) and also:

$$n_x u_{avg} + n_z w_{avg} = n \cdot \frac{\partial x}{\partial t}\bigg|_{F.S.} \qquad (2.12)$$

which is the kinematic condition at the flow front expressing the requirement of no-flow through the free surface.

Equations (2.10) and (2.11) with the above boundary conditions represent the most advanced of the models based on the Hele-Shaw approximation.

This model was employed by the Cornell Injection Molding Group (Wang et al., 1977,1985) and it was solved numerically, with a finite element/finite difference formulation (Hieber & Shen, 1980) and a boundary element formulation (Shen, 1984). Good agreement was found between the predictions and the measurements concerning the shape of the advancing flow front, the location of weldlines, and the temporal pressure trace at various positions in the cavity (Hieber et al.,1983).

It is of interest to examine eq. (2.10). Denoting by ∇_{xz} the two-dimensional gradient operator, eq. (2.10) takes the form:

$$S_\mu \nabla^2_{xz} P + \nabla_{xz} S_\mu \cdot \nabla_{xz} P = 0 \tag{2.13}$$

If it is assumed that the viscosity variation in x- and z-directions (spreading directions) is negligible as compared to the variation in the y-direction (transverse or thickness direction), then the second term in eq. (2.13) vanishes, and eq. (2.13) reduces to:

$$\nabla^2_{xz} P = 0 \tag{2.14}$$

i.e., the Laplace equation in two dimensions, which means that analytical solutions exist for some geometric configurations. This result was pointed out and discussed by White (1975). Kamal et al (1975) and Kuo & Kamal (1976) considered the Laplace equation for pressure coupled with the energy equation and presented analytical solutions for rectangular cavities. Comparison with experiments showed good agreement for pressure variation and flow front position. The same problem was studied by Ryan & Chung(1980) with a conformal mapping technique.

Broyer et al (1975) developed a model based on the thin cavity approximation and employed the Flow Analysis Network method (Tadmor et al, 1974) for the simulations. Flow front progression, temperature and fill time determined experimentally (Krueger & Tadmor, 1980) compared well with the model predictions.

Recently, Couniot & Crochet (1986) presented a front tracking algorithm using finite elements for calculating Hele-Shaw flows in thin molds of arbitrary shape.

It must be pointed out that the computer models of this category are extremely slow and require large computer memory. This is due to the moving boundary which is not only unknown in space but also evolves in time. Elliot & Janovsky (1979,1981) and Elliot (1980) proposed an interesting method to overcome this problem. Assuming validity of the Laplace equation, eq. (2.14), they introduced the transformation (Duvaut, 1973):

$$\Phi(x, z, t) = \int_0^t P(x, z, t')\,dt' \tag{2.15}$$

Then the transformed problem in terms of Φ is:

$$\nabla_{xz}^2 \Phi = 1 \tag{2.16}$$

with boundary conditions:

Inflow:

$$\Phi = \int_0^t P\,dt', \quad \text{when } P \text{ is specified} \tag{2.17a}$$

or

$$\frac{\partial \Phi}{\partial n} = \int_0^t \frac{\partial P}{\partial n}\,dt', \quad \text{when } \frac{\partial P}{\partial n} \text{ is specified} \tag{2.17b}$$

Solid Walls:

$$\frac{\partial \Phi}{\partial n} = 0 \tag{2.17c}$$

Flow Front:

$$\Phi = 0 \quad \text{and} \quad \frac{\partial \Phi}{\partial n} = 0 \tag{2.17d}$$

The advantage of this approach is that it transforms a moving boundary problem to a free boundary problem where time enters as a parameter and the solution can be determined for a
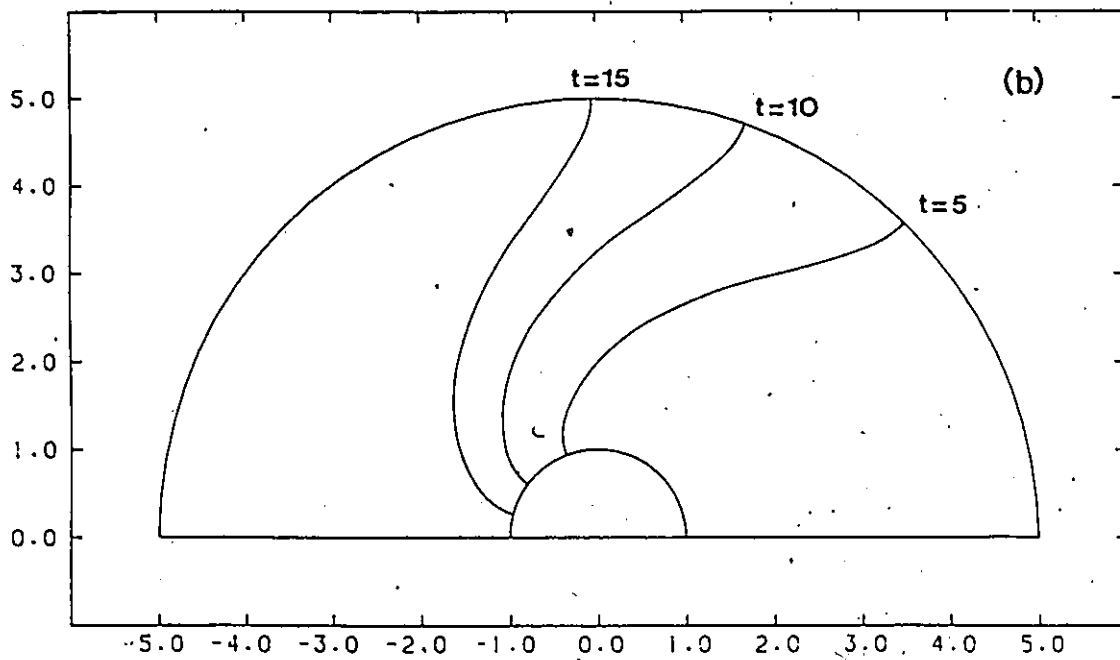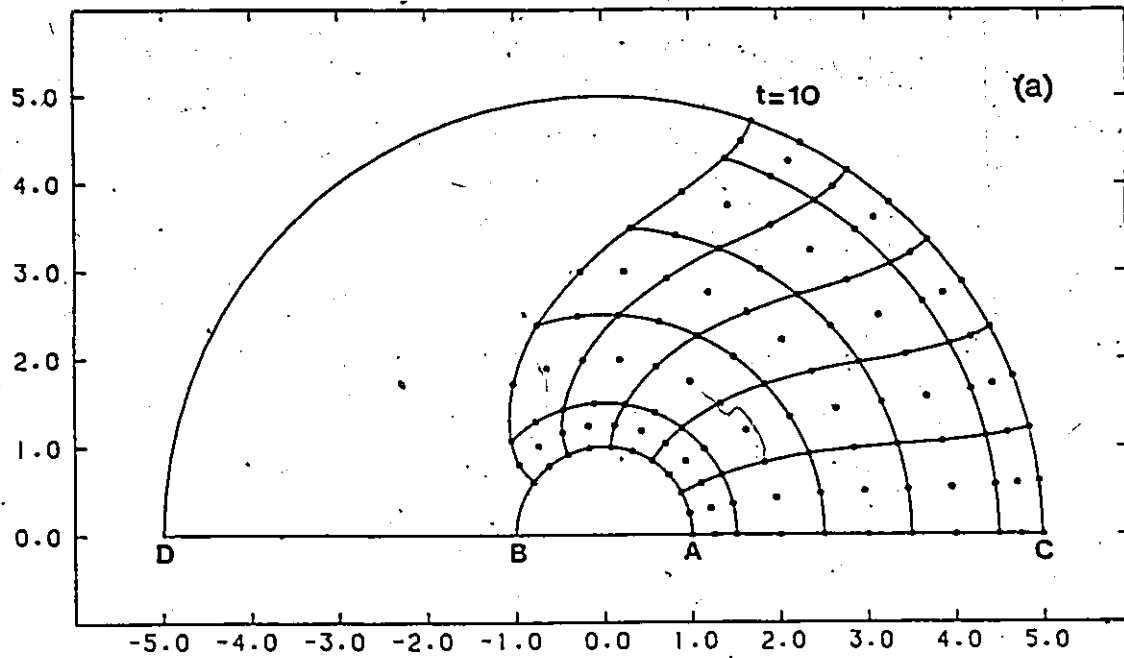
Figure 2.1   Mold filling of a thin cavity:
· (a)   deformed finite element grid
(b)   flow front shape at various times

given time. An example problem, originally solved by Elliot & Janovsky (1979) is shown in Figure 2.1, concerning the flow between the two semicircles AB and CD (Mavridis et al., 1986c). Fluid is injected across the line AC so that the pressure is kept constant at the constant value 1. The results depicted in Figure 2.1 are obtained through a finite element formulation of eqs. (2.16-17) where the transformed variable Φ and the flow front location are determined simultaneously. The deformed finite element grid is shown in Figure 2.1a at $t=10$, and the flow front position at three times is shown in Figure 2.1b. It can be observed that the flow front is normal to the walls. This is an unrealistic prediction and is associated with the limitations of the Hele-Shaw theory.

2.2.2.2 Transverse Plane: Fountain Effect

While models based on the Hele-Shaw (or thin cavity) approximation have been effective in predicting quantities such as pressure, fill time, and weldline position, their limitations must be realized.

For cavities with high aspect ratios the Hele-Shaw approximation holds up to distances of the order of the gapwidth, O(H), from the boundaries (Richardson, 1972). However, it is the phenomena that take place within distances of order O(H) behind the flow front that have a profound effect on the properties of the molded part and must be taken into account.

These phenomena involve the flow kinematics in the transition region between the unidirectional shear flow and the flow front. Fluid elements near the centerline move faster so that they decelerate as they approach the slower moving front. Mass continuity results in a transverse velocity component which drives the fluid elements outward, towards the walls. This motion when viewed from a frame of reference moving with the flow front gives a fountain-like picture (Rose, 1961). The implications of fountain flow in injection molding are

obvious: hot melt from the central core reaches the cold walls passing through a complex shear and elongational flow. At the wall the melt solidifies creating a highly oriented "skin". The present work, to be described in detail in the subsequent chapters, is the first systematic effort to study the fluid mechanics of fountain flow and how it affects the microstructure development in injection molded parts (see also Mavridis et al,1986a,b, 1987, 1988a,b).

2.2.3   Network Models

In this approach the aim is to overcome the mathematical difficulties associated with a rigorous modeling of mold filling. The actual mold is decomposed into a network of basic units of simple geometry (e.g., circular pipe, disk, rectangular channel). In practice each unit is characterized by one spatial dimension. Simplified analytical solutions or macroscopic balances for the quantity of interest (mass, momentum, energy) are derived over each unit. Coupling is determined by requiring continuity at the nodes, i.e., the connections between the units. With this technique a tree structure is obtained that allows prediction of fill times, pressure drop, temperatures, and forces developed in the mold network, within reasonable engineering tolerances.

The development of CAD/CAM technology, interactive work stations, versatile computer graphics, and the methodological simplicity of the network concept made this approach very popular. Various models and commercially available computer packages have appeared thus far (Bernhardt, 1983; Richardson et al., 1980; Bangert & Menges, 1981; Hieber,1982 ; Schacht et al., 1985; Atkinson, 1986).

2.3   Concluding Remarks

The complicating features of a general mathematical modeling of injection mold filling have been discussed. The modeling objectives are classified into large and small scale

phenomena. Small scale phenomena include weldlines and microstructure development and must be captured if product properties are to be predicted. Models based on the network approach and the more rigorous models based on the Hele-Shaw approximation predict large scale phenomena (pressure drop, fill time, cooling requirements) and weldline location. Studies on the transverse plane explain the effect of fountain flow on the microstructure of the final molded part.

CHAPTER 3

STEADY-STATE ANALYSIS OF FOUNTAIN FLOW

This chapter contains the steady-state finite element studies on the fountain-flow problem. It begins with background information and a literature survey on the fountain flow phenomenon. A finite element algorithm is presented for the numerical simulation of free surface flows. The method is employed to study the fountain flow of Newtonian and shear-thinning fluids in planar and axisymmetric geometries. Using the numerically computed flow field an investigation is performed on the effect of fountain flow kinematics on the deformation experienced by the fluid. Computational results are compared to available experimental photographs. Finally, the general problem of fountain and reverse fountain flow is considered. A double-node finite element method appropriate for this problem is proposed and is applied to simulate the immiscible displacement of two different fluids in a capillary tube.

3.1 Introduction

The term "fountain effect" was coined and discussed by Rose (1961), to describe the flow field near a fluid/fluid interface advancing inside a capillary when a moving fluid is displacing another immiscible fluid. A conceptualization of the flow field is shown in Figure 3.1, for the case of steady motion and a frame of reference at rest with respect to the advancing interface, i.e., for an observer riding with the flow front. Rose (1961) introduced the designation "fountain effect" as a term having phenomenological merit, to describe how the advancing fluid particles from the central core space decelerate as they approach the slower

17

FOUNTAIN
FLOW

REVERSE
FOUNTAIN
FLOW
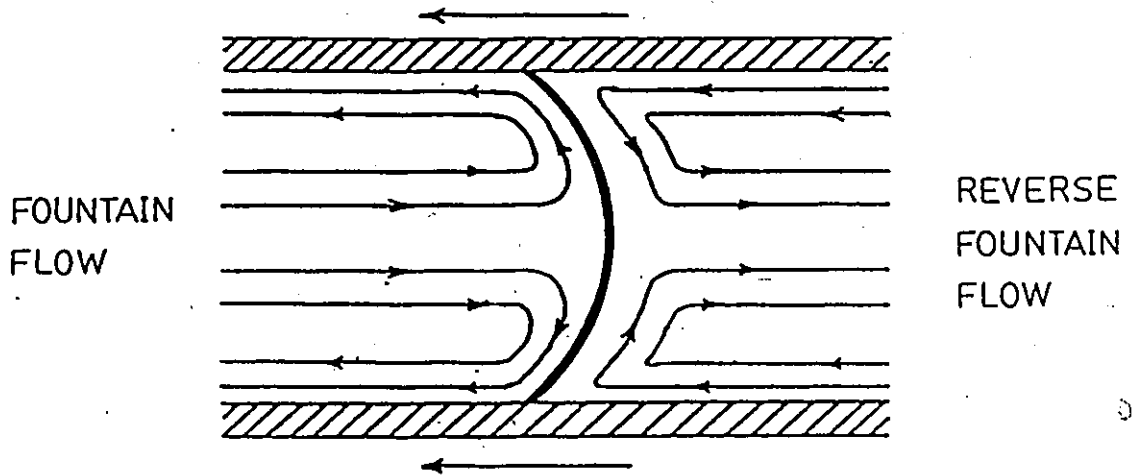
Figure 3.1   Schematic of fountain flow and reverse fountain flow

moving interface region, and acquire an outward component of velocity as they spill towards the wall region vacated by the advancing interface. Correspondingly, a "reverse fountain effect" is seen in the receding fluid ahead of the interface, as fluid is displaced from the wall region and moves towards the centerline.

Fountain flow is associated with the flow rearrangement behind a flow front advancing between solid boundaries and is present in many areas of theoretical and industrial significance: wetting hydrodynamics, mold filling operations (injection and reaction injection molding) and flow through porous media. Earlier observations on this type of flow have been reported by a number of people; West (1911), Yarnold (1938) and Schwartz et al (1964). Ballman and Toor (1960) were also aware of the importance of this phenomenon in injection molding.

Schmidt (1974) found with injection molding visualization experiments that colored pellets introduced along the centerline come out at the surface in contact with the mold walls in reverse order and deformed into characteristic V-shapes. Tadmor (1974) did a semiquantitative study of fountain flow by assuming steady elongational flow near the advancing front and made calculations of some orientation parameters.

The first theoretical attempt to determine the flow field was apparently made by Bhattacharji & Savic (1965). These authors assumed the flow front to be flat and perpendicular to the solid walls and derived analytically a solution for the streamfunction, for the case of a Newtonian fluid in planar and axisymmetric geometries. The solution of Bhattacharji & Savic (1965) was later used by Castro & Macosko (1982) in their model of the reaction injection mold filling process.

The primary and most formidable difficulty in solving the fountain flow problem is associated with the flow front shape which is unknown a priori and must be determined along with the flow field as part of the solution (free boundary or free surface problem). The

unknown free surface shape results in a nonlinear problem that is very intractable analytically. Bigg (1975) attempted a numerical solution utilizing the Marker-and-Cell (MAC) method. The same numerical technique was employed in the studies of Huang (1978), Huang et al (1986) and Kamal et al (1985). Preliminary attempts to simulate the flow with a finite element method were reported by Wang et al (1978). Givler et al (1983) obtained a finite element solution for a Newtonian fluid in their studies of fiber orientation in dilute suspensions.

Detailed finite element simulations with Newtonian and shear-thinning fluids in planar and axisymmetric geometries were reported in an earlier publication based on the present work (Mavridis et al, 1986a). The effect of fountain flow kinematics on the deformation experienced by the fluid was examined in Mavridis et al (1986b); it was shown that fluid elements from the centerline stretch as they move towards the walls and form characteristic V-shapes, fully in agreement with Schmidt's (1974) visualization experiments. Similar results were later found by Coyle et al (1987) and Kamal et al (1988). Behrens et al (1987) studied both theoretically and experimentally the transient free surface flow in a tube.

In all the above studies the receding fluid was considered to be a gas, which to a good approximation is inviscid and inertialess and therefore the reverse fountain flow pattern does not appear. However, it is of interest to examine the general case of two immiscible viscous fluids displacing each other at constant speed. This is the configuration discussed by Rose (1961). Referring to Figure 3.1, it is shown that near the interface the material particles on the advancing liquid side have an outward directed velocity while the material particles on the receding fluid side have an inward directed velocity. Based on this observation Rose (1961) argued that continuity of the two velocity fields at the interface requires that no tangential motion occur along the interface. It can be shown that if the above argument holds then the interface has a constant curvature throughout, or equivalently it is a segment of a

sphere. However, Rose's (1961) argument does not hold. It is based on the crucial assumption that the streamlines very near the interface follow the same pattern as those depicted in Figure 3.1. Dussan (1977) showed with visualization experiments that a recirculating flow occurs adjacent to the interface and inside the less viscous fluid. The double-node finite element technique described in Section 3.4 gives for the first time a complete solution to the general fountain and reverse fountain flow problem. The results, reported earlier in Mavridis et al (1987), demonstrate clearly the existence of the vortex adjacent to the interface, fully in agreement with Dussan's (1977) experimental observations.

3.2   Fountain flow simulations

3.2.1   Mathematical Modeling

Consider an incompressible, isothermal, viscous fluid with a free front advancing at constant speed U between parallel plates or in a capillary tube. Such a flow would appear to be unsteady for a stationary observer (Figure 3.2a). However, for an observer moving at the same speed in the flow direction the walls would appear to move backwards and the flow would be steady (Figure 3.2b). Therefore in this moving frame of reference the problem can be analyzed in the steady-state.

The governing equations include the mass and momentum conservation equations:

$$\nabla \cdot \mathbf{V} = 0 \tag{3.1}$$

$$\text{Re } \mathbf{V} \cdot \nabla \mathbf{V} = \nabla \cdot \boldsymbol{\sigma} + S^{-1}\mathbf{g} \tag{3.2}$$

Variables are made dimensionless as follows: length with the half gapwidth H (or tube radius R), velocity with the average velocity of the fluid U, viscosity with a reference viscosity μ_0 and stress with $\mu_0 U/H$. $\text{Re} = \rho U H/\mu_0$ is the Reynolds number and $S^{-1} = \rho g H^2/\mu_0 U$ is the inverse Stokes number, where ρ is the density and g is the gravitational
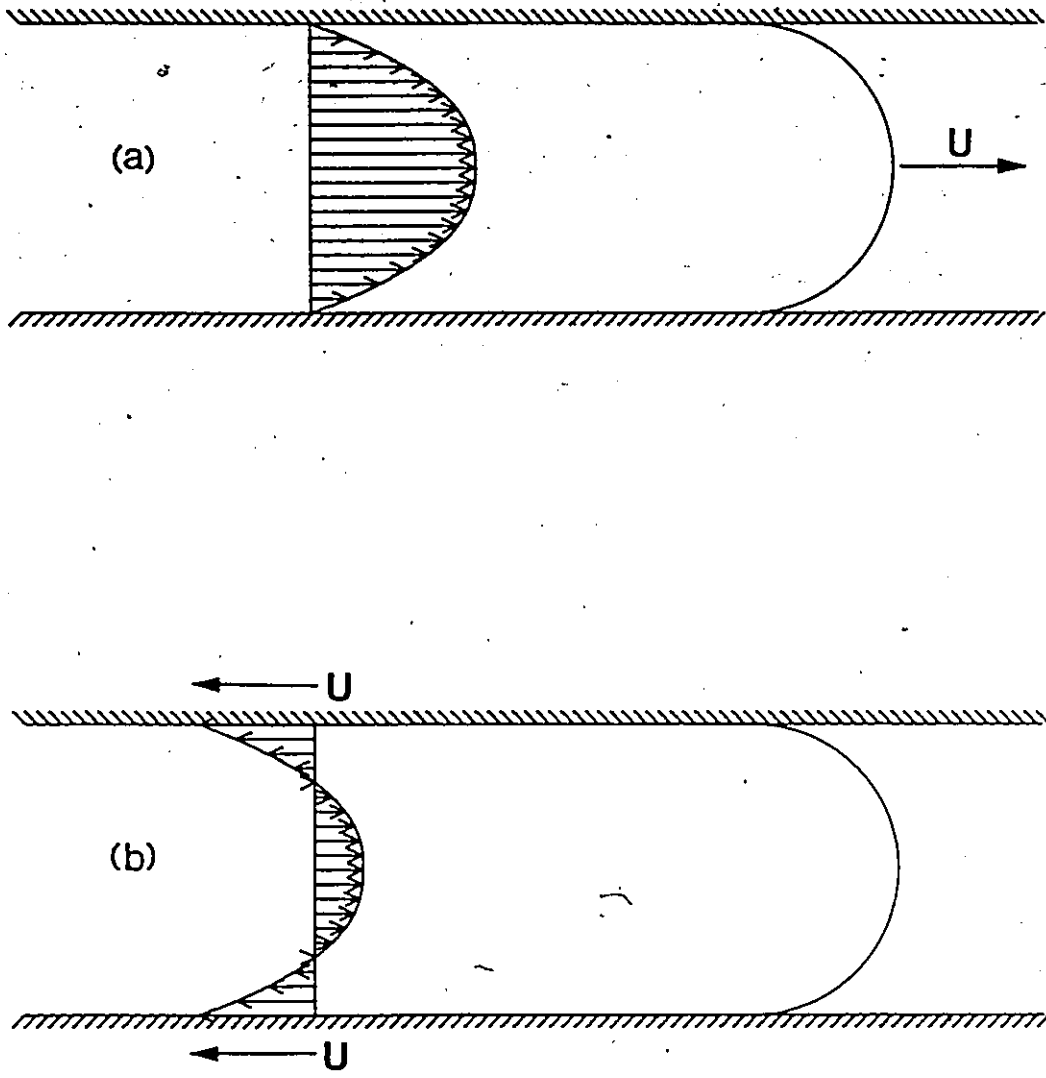
Figure 3.2   (a)   Advancing flow front and stationary walls
                            (b)   Stationary flow front and moving walls

acceleration. Under typical mold filling conditions both Re and S^{-1} are very small (i.e., convective and gravitational effects are negligible compared to viscous effects).

In eqs.(3.1) and (3.2) V is the velocity vector and σ is the total stress tensor, $\sigma = -PI + \tau$, where P is the pressure and τ is the deviatoric (or extra) stress tensor. For viscous fluids $\tau = \mu(\nabla V + \nabla V^T)$.

Referring to Figure 3.3, for the planar geometry we have the following boundary conditions:

On AD: fully developed velocity profile

$$u = f(y), \quad v = 0 \qquad (3.3.1)$$

On AB: symmetry conditions

$$\tau_{xy} = 0, \quad v = 0 \qquad (3.3.2)$$

On CD: no-slip at the wall

$$u/U = -1, \quad v = 0 \qquad (3.3.3)$$

On BC: free surface boundary conditions

Kinematic condition: $\qquad \mathbf{n} \cdot \mathbf{V} = 0 \qquad (3.3.4)$

Dynamic condition : $\qquad \mathbf{n} \cdot \sigma = -P_a \mathbf{n} + \dfrac{1}{Ca}\left(\dfrac{1}{R_1} + \dfrac{1}{R_2}\right)\mathbf{n} \qquad (3.3.5)$

The kinematic condition, eq.(3.3.4) expresses the requirement that no fluid particle crosses the free surface which is a streamline. The dynamic condition, eq.(3.3.5) expresses the balance of viscous, pressure and surface tension forces. The capillary number, $Ca = \mu U / \gamma$ is a dimensionless group that measures the relative importance of viscous over surface tension forces, and γ is the surface tension. Polymer melts are very viscous and Ca is typically very large (i.e., negligible surface tension effects). P_a is the ambient pressure, usually set to zero as the pressure datum. $\mathbf{n}$ is the unit vector normal to the free surface and R_1, R_2 are the principal radii of curvature of the free surface. For a two-dimensional surface $1/R_2 = 0$ and
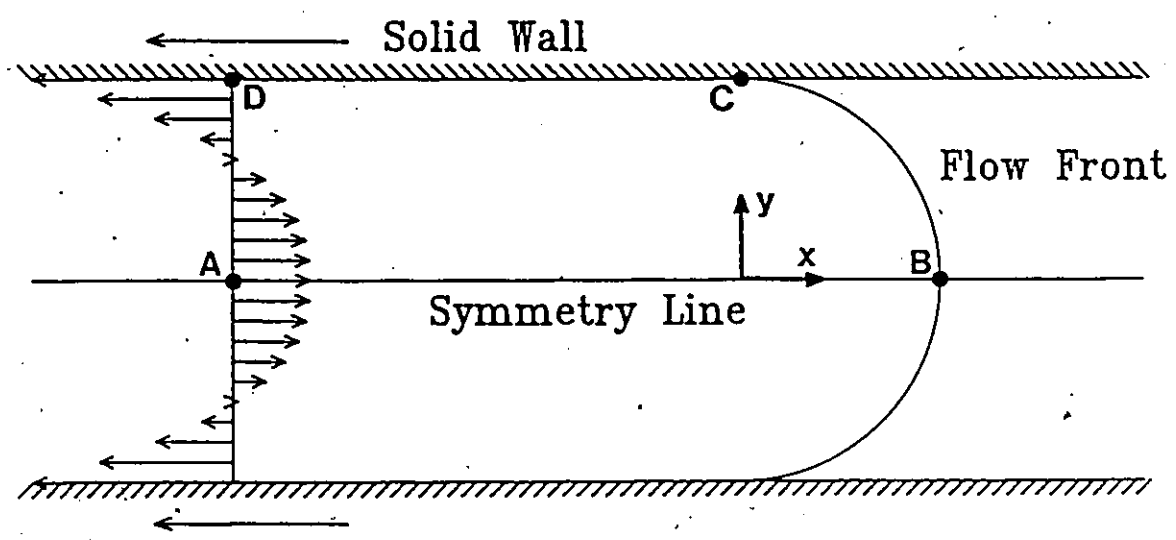
Figure 3.3   Definition sketch for the fountain flow problem

$$\frac{1}{R_1} n = n \cdot \frac{dt}{d\ell} \tag{3.4}$$

where ℓ is the arc length along the free surface and t is the unit tangent vector in the direction of increasing ℓ.

By inspection of the boundary conditions, eqs.(3.3) it is seen that at known portions of the flow domain there exist only two scalar boundary conditions while at the free surface the available boundary conditions are three (two scalar boundary conditions resulting from the dynamic condition, eq.(3.3.5) and the kinematic condition, eq.(3.3.4)). This is the very characteristic of free surface flows and arises due to the unknown free surface shape. The associated nonlinearity of the problem is apparent from eqs.(3.3.4), (3.3.5); the unknown unit vector n results in nonlinear terms in the boundary conditions, even if the governing equations are linear (e.g. creeping Newtonian flow). A finite element technique suitable for this class of flows is considered in the next section.

3.2.2   Finite element formulation

The Finite Element Method belongs to the general class of weighted residual methods (Finlayson, 1972) and is a powerful technique for solving partial differential equations. Strang & Fix (1973) present the mathematical foundations of the method while further background and applications oriented material is provided in standard texts (Zienkiewicz, 1977; Huebner & Thornton, 1982; Crochet et al, 1984). The following describes the basics of the finite element method as applied to free surface flow problems.

The finite element method begins by expanding the primitive variables (velocity components and pressure) in a suitable set of basis functions:

$$V = \sum_i V^i \phi^i(\xi, \eta), \quad P = \sum_i P^i \pi^i(\xi, \eta) \tag{3.5}$$

where V^i, P^i are nodal variables, $\phi^i(\xi,\eta)$, $n^i(\xi,\eta)$ are the associated basis functions and ξ,η are the local coordinates in the element. Elements used in this work are the 9-node quadrilateral and 6-node triangular isoparametric elements with $C^0 - P^2$ approximation for velocity and $C^0 - P^1$ for pressure (see appendix A).

The finite element approximations, eqs.(3.5), are inserted into the governing equations, eq.(3.1) and (3.2). In general, the finite element approximations do not satisfy the governing equations exactly and there will be a momentum and continuity residual. The resulting momentum residuals are weighted with the velocity basis functions and the continuity residuals are weighted with the pressure basis functions. The weighted residuals are integrated over the solution domain Ω and set to zero (Galerkin formulation):

$$R^i_m = \int_\Omega \left\{ Re\, V \cdot \nabla V - \nabla \cdot \sigma - S^{-1} g \right\} \phi^i d\Omega = 0 \qquad (3.6)$$

$$R^i_c = \int_\Omega \nabla \cdot V\, n^i d\Omega = 0 \qquad (3.7)$$

The stress term in eq.(3.6) is integrated by parts (i.e., applying the divergence theorem):

$$R^i_m = \int_\Omega \left\{ \phi^i\, Re\, V \cdot \nabla V + \nabla \phi^i \cdot \sigma - \phi^i S^{-1} g \right\} \phi^i d\Omega - \int_{\partial\Omega} n \cdot \sigma\, \phi^i\, d\ell = 0 \qquad (3.8)$$

where $\partial\Omega$ is the boundary curve enclosing the solution domain Ω and ℓ is the arc length along $\partial\Omega$. Note that in the above formulation, eq.(3.8), the dynamic (stress) boundary conditions arise naturally as boundary integrals in the momentum residuals.

Eq. (3.7) and (3.8) when applied at the nodes of the discretized flow domain along with the appropriate boundary conditions provide as many algebraic equations as there are unknown velocity and pressure nodal degrees of freedom.

The complicating feature of free surface flows is that part of the flow boundary $\partial\Omega$ is unknown (free boundary) and must be determined as part of the solution. The earliest

application of the finite element method to free surface flows was that of Nickell et al (1974), in which the determination of the free surface and the flow field were decoupled through a Picard-like iteration. A similar method has been used by many workers (Reddy & Tanner, 1978; Crochet & Keunings, 1980; Mitsoulis & Vlachopoulos, 1985) and in the early stages of this work (Mavridis et al, 1986a, 1987). However, the decoupling technique exhibits slow convergence and does not converge at all over certain parameter ranges (Silliman & Scriven, 1980; Mavridis et al, 1987). The technique adopted in this work is a version of the so-called u-v-p-h formulation (Kistler & Scriven, 1983). The u-v-p-h-δ formulation described below is a fast and robust method for free surface flows and is easily extended to transient flows (Mavridis et al, 1988a and Chapter 4) and viscoelastic flows (Mavridis et al, 1988b and Chapter 5).

In the u-v-p-h-δ formulation the free surface is represented by piecewise quadratic line segments each of which forms one side ($-1 \leq \xi \leq 1$, $\eta = 1$) of an isoparametric 9-node quadrilateral element, as shown in Figure 3.4. A free surface segment is defined uniquely by the coordinated of three nodal points, two end points and the midside point. Every free surface node x_F^i moves along a spine, a straight line which is characterized by a base point x_B^i and a unit vector $e^i = e_x \cos\delta^i + e_y \sin\delta^i$, where $\cos\delta^i$ and $\sin\delta^i$ are the direction cosines of e^i. The position of x_F^i is determined as the distance along the spine (cf. Figure 3.4):

$$x_F^i = x_B^i + h^i e^i \qquad (3.9)$$

If x_F^{i-1}, x_F^i, x_F^{i+1} are the three nodes that define a free surface segment, the free surface is represented as:

$$x = \sum_{i-1}^{i+1} x_F^j \phi^j (\xi, \eta = 1) \qquad (3.10)$$

In general there are two position parameters corresponding to every free surface node x_F^i; h^i that is associated with distance and δ^i that is associated with orientation. The δ^i parameters corresponding to free surface segment end-points are fixed (input data) while
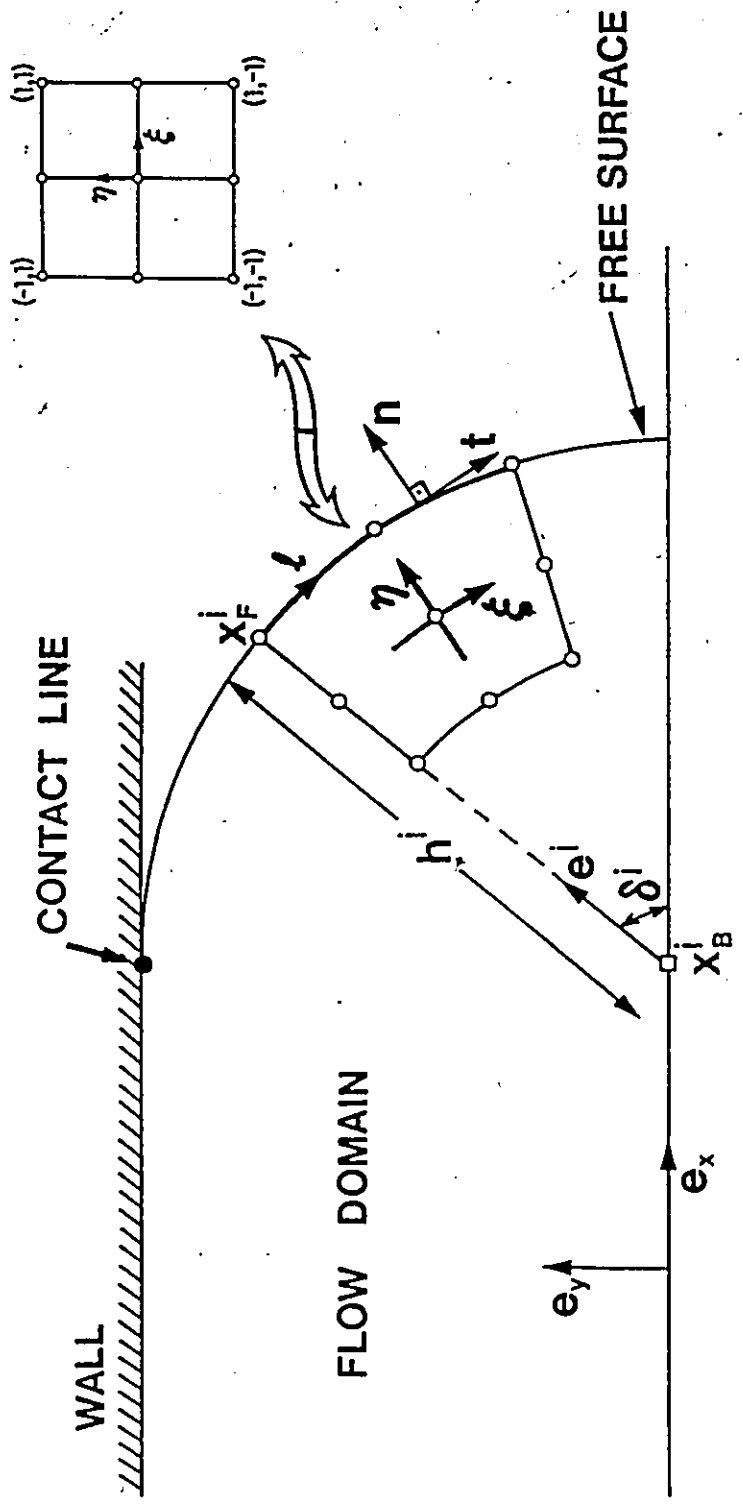
Figure 3.4   Free surface parametrization

those corresponding to midside nodes enter the set of unknowns. The latter δ^i are determined on the requirement that the midside node be located at the midpoint of the free surface arc. The variable midside spine direction is especially useful in transient flows (see Chapter 4). The mathematical expression of the above expression is a follows: assume that free surface segment is mapped on the $-1 \leq \xi \leq 1$, $\eta = 1$ side of the standard $\xi - \eta$ square. The corner and midside nodes are at $\xi = -1, 1$ and 0 respectively. The differential arc length $d\ell$ is

$$d\ell = \left(x_\xi^2 + y_\xi^2 \right)^{1/2} \Bigg|_{\eta=1} d\xi \tag{3.11}$$

and the condition that the midside node is located at the midpoint of the arc is:

$$\int_{\xi=-1}^{\xi=0} d\ell = \int_{\xi=0}^{\xi=1} d\ell \tag{3.12a}$$

or

$$\int_{-1}^{0} \left(x_\xi^2 + y_\xi^2 \right)^{1/2} \Bigg|_{\eta=1} d\xi = \int_{0}^{1} \left(x_\xi^2 + y_\xi^2 \right)^{1/2} \Bigg|_{\eta=1} d\xi \tag{3.12b}$$

The h^i unknowns are linked with the kinematic residuals at the free surface, i.e.

$$R_k^i = \int_{F.S.} \mathbf{n} \cdot \mathbf{V} \phi^i (\xi, \eta = 1) d\ell = 0 \tag{3.13}$$

In summary, the unknowns and the corresponding weighted residuals in the u-v-p-h-δ formulation for free surface flows are

$$V^i: R_m^i = \int_\Omega \left\{ \phi^i \, \mathrm{Re} \, \mathbf{V} \cdot \nabla \mathbf{V} + \nabla \phi^i \cdot \sigma - \phi^i S^{-1} g \right\} \phi^i \, d\Omega - \int_{\partial\Omega} \mathbf{n} \cdot \sigma \, \phi^i \, d\ell = 0 \tag{3.14}$$

$$P^i: R_c^i = \int_\Omega \nabla \cdot \mathbf{V} \, \pi^i \, d\Omega = 0 \tag{3.15}$$

$$h^i: R_k^i = \int_{F.S.} \mathbf{n} \cdot \mathbf{V} \phi^i (\xi, \eta = 1) d\ell = 0 \tag{3.16}$$

$$\delta^i: R_\delta^i = \int_{-1}^{0} \left(x_\xi^2 + y_\xi^2 \right)^{1/2} \Bigg|_{\eta=1} d\xi - \int_{0}^{1} \left(x_\xi^2 + y_\xi^2 \right)^{1/2} \Bigg|_{\eta=1} d\xi = 0 \tag{3.17}$$

Organizing the unknowns into the vector X

$$X^T = [V^T, P^T, h^T, \delta^T] \qquad (3.18)$$

and the weighted residuals into the vector R

$$R^T = [R_m^T, R_c^T, R_k^T, R_\delta^T] \qquad (3.19)$$

the system of algebraic equations to be solved is

$$R(X) = 0 \qquad (3.20)$$

This system is solved with Newton-Raphson iteration, i.e.

$$X^{(m+1)} = X^{(m)} + d^{(m)} \qquad (3.21)$$

$$J^{(m)} d^{(m)} = -R^{(m)} \qquad (3.22)$$

where $J = \partial R/\partial X$ is the Jacobian matrix of the algebraic system, eq.(3.20). Typically, the Newton-Raphson iteration exhibits quadratic convergence as shown in Figure 3.5. Theoretically, the Newton-Raphson scheme exhibits quadratic convergence near regular points of the solution and for sufficiently good initial solution estimate (Isaacson & Keller, 1966). For the problems examined in this chapter three to five iterations were sufficient to reduce the maximum relative update in eq.(3.21) below 10^{-4}. It must be noted that the correct evaluation of the Jacobian matrix in eq.(3.22) is crucial for the successful application of the Newton-Raphson scheme. In fact, imposing a strict convergence criterion and insisting on quadratic convergence proved to be a good test of the correctness of the Jacobian matrix, which is particularly complicated due to the presence of the free surface derivatives. Detailed derivations of the finite element equations and the Jacobian matrix are given in appendix A.

Once a converged solution is obtained the flow field can be visualized with velocity vector and various contour plots. A useful contour plot is the streamfunction contour plot which provides the streamlines. The streamfunction ψ is defined as:

$$u = \partial\psi/\partial y, \quad v = -\partial\psi/\partial x \qquad (3.23)$$

The streamfunction can be determined a posteriori by solving the Poisson equation:
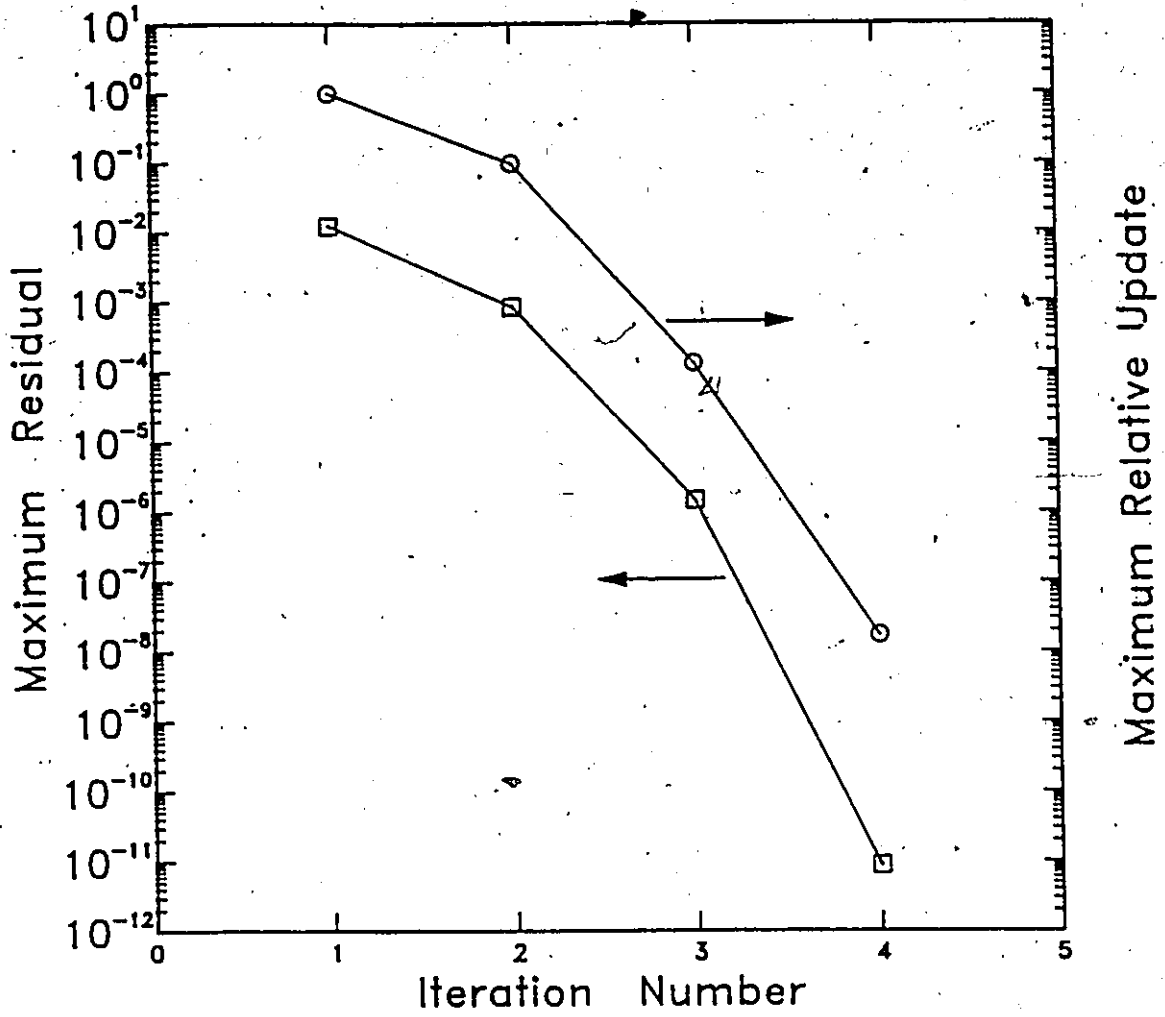
Figure 3.5   Behavior of Newton-Raphson iteration

$$\frac{\partial^2 \psi}{\partial x^2} + \frac{\partial^2 \psi}{\partial y^2} = u_y - v_x \tag{3.24}$$

The above equation is solved on the same finite element grid by expanding the streamfunction in the following set of basis functions:

$$\psi = \sum_i \psi^i \phi^i(\xi, \eta) \tag{3.25}$$

and the nodal streamfunction values ψ^i are determined by solving the following linear system, which results from the Galerkin/finite element discretization of eq.(3.24):

$$A_{ij} \psi^j = B_i \tag{3.26}$$

$$A_{ij} = \int_\Omega (\phi_x^i \phi_x^j + \phi_y^i \phi_y^j) \, d\Omega \tag{3.27}$$

$$B_i = \int_\Omega (v_x - u_y) \phi^i \, d\Omega \tag{3.28}$$

3.2.3 Newtonian Fluids

3.2.3.1 Planar Geometry

The problem of fountain flow of a Newtonian fluid in planar geometry was considered first. A fully developed velocity profile was imposed at the inflow plane (AD in Figure 3.3):

$$u/U = \frac{3}{2} [1 - (y/H)^2] - 1 \tag{3.29}$$

and the finite element method of Section 3.2.2 was applied to obtain the flow field and the flow front shape.

Three successively refined finite element meshes were used in the calculations. These meshes are plotted in Figure 3.6 and their characteristics are listed in Table 3.1. Computations with the three meshes showed close agreement of the results. The results with MESH 2 and MESH 3 agreed within three to four significant figures away from the contact

MESH 1
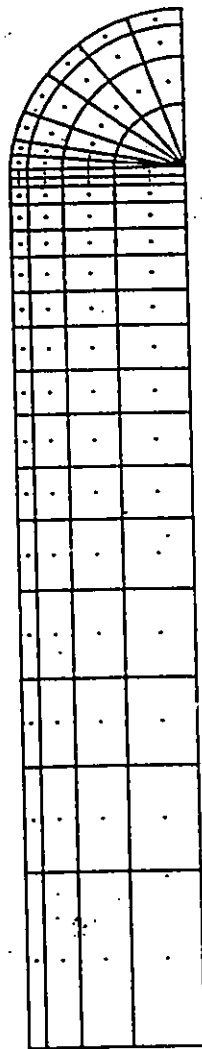
MESH 2
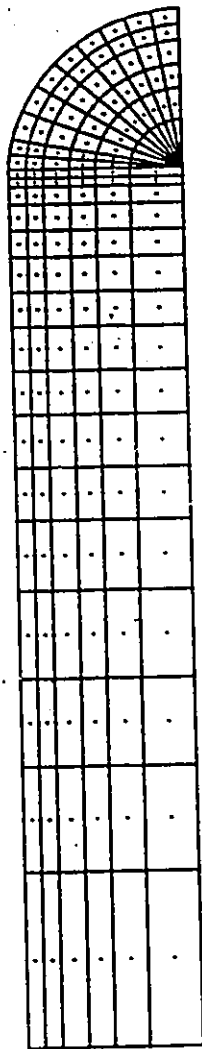
MESH 3
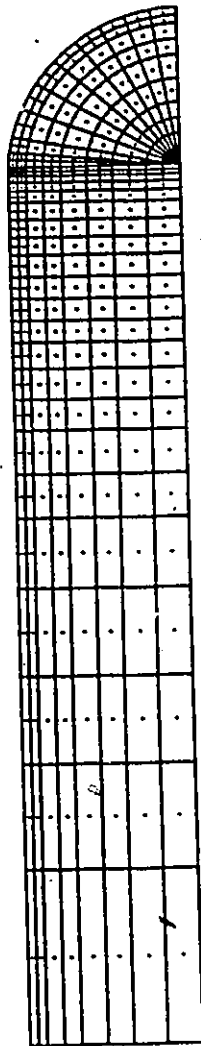
Figure 3.6   Finite element meshes for Newtonian fountain flow

line, i.e. the free surface/wall intersection. As an assessment of the accuracy of the results at this level of mesh refinement consider the following measure of the relative difference of the solutions with MESH 2 and MESH 3 along the free surface:

$$\frac{1}{N_u} \left[\sum_{i=1}^{N_u} \left(\frac{u_{(3)}^i - u_{(2)}^i}{u_{(3)}^i} \right)^2 \right]^{1/2} = 0.021$$

$$\frac{1}{N_v} \left[\sum_{i=1}^{N_v} \left(\frac{v_{(3)}^i - v_{(2)}^i}{v_{(3)}^i} \right)^2 \right]^{1/2} = 0.0156$$

$$\frac{1}{N_p} \left[\sum_{i=1}^{N_p} \left(\frac{p_{(3)}^i - p_{(2)}^i}{p_{(3)}^i} \right)^2 \right]^{1/2} = 0.039$$

$$\frac{1}{N_h} \left[\sum_{i=1}^{N_h} \left(\frac{h_{(3)}^i - h_{(2)}^i}{h_{(3)}^i} \right)^2 \right]^{1/2} = 0.00053$$

where N_u, N_v, N_p, N_h are the number of x-velocity, y-velocity, pressure and free surface unknowns respectively at the free surface. The comparison indicates that a sufficient accuracy has been reached at this level of mesh refinement. MESH 2 was selected as the basis finite element grid for all subsequent calculations.

Table 3.1 Finite element meshes for Newtonian fountain flow

	Elements	Nodes	Unknowns	CPU sec/iteration (VAX 8600)
MESH 1	92	402	856	11.7
MESH 2	156	659	1437	23.7
MESH 3	264	1106	2418	48.6

The velocity vectors for a moving frame of reference are shown in Figure 3.7. This figure shows clearly that an observer traveling with the average velocity of the fluid will see the fluid particles approaching the flow front to decelerate, spill over and go backwards. The streamlines are plotted in Figure 3.8 illustrating the characteristic fountain flow pattern, with the streamlines resembling a series of nested loops.

The instantaneous velocity vectors, for a fixed frame of reference are plotted in Figure 3.9. These are constructed from the velocity vectors of Figure 3.7 by adding the average velocity of the fluid to the x-component of velocity. The velocity profile is parabolic in the fully developed flow region (upstream). Near the flow front the deceleration of fluid particles results in the development of a transverse velocity component and the velocity vectors are directed outward towards the walls. This is better illustrated in Figure 3.10, which shows the streamlines in the fixed frame of reference. The streamlines of Figure 3.10 is the picture that would be seen with a fixed camera in a visualization experiment. It is shown that upstream the streamlines are parallel to the wall while at the flow front they bend towards the walls corresponding to the outward motion of the fluid particles in that region. Both Figures 3.9 and 3.10 demonstrate clearly that for a fixed frame of reference, i.e. in a physical flow experiment the fluid particles never turn back, but they merely move outward entering regions of lower velocity and thus appearing to move backwards for an observer traveling with the (greater) average velocity of the fluid.

The variation of velocity along the centerline is given in Figure 3.11. It can be observed that the region over which the deceleration takes place extends only a small distance behind the flow front. At $x/H = -0.815$ the velocity is $u/U = 0.495$ (99% of $u_{max}/U = 0.5$) and upstream of this position the flow can be considered as fully developed pressure driven flow. Contours of total fluid velocity (i.e. $(u^2 + v^2)^{1/2}$) given in Figure 3.12
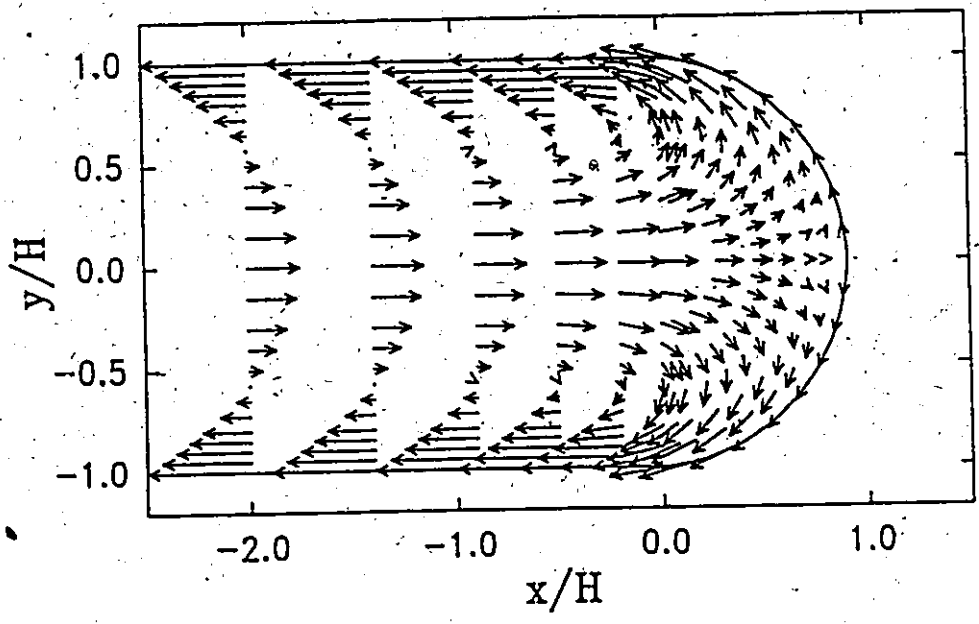
Figure 3.7   Velocity vectors in the moving frame of reference
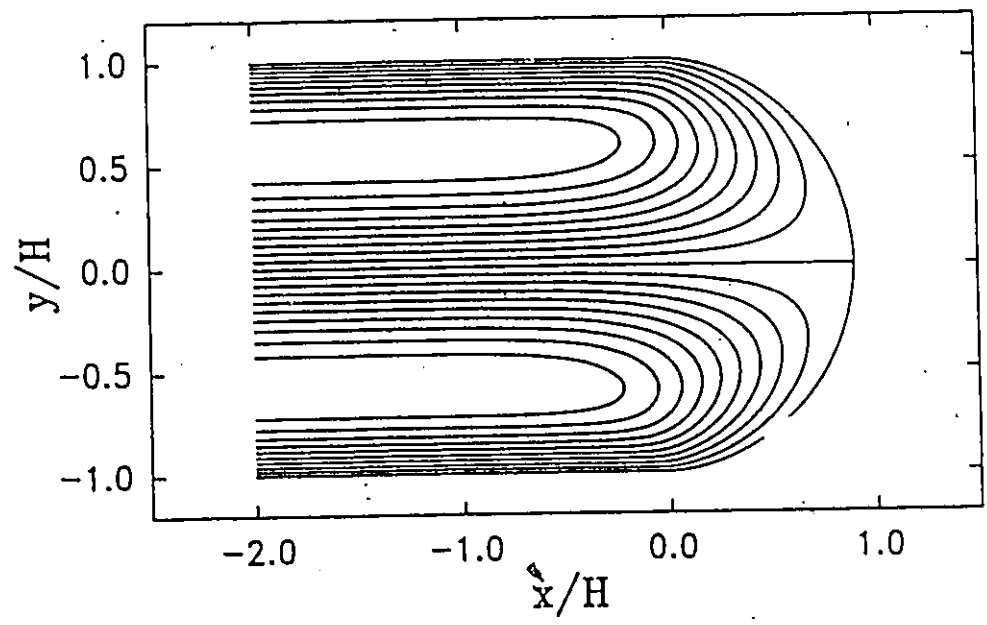
Figure 3.8   Streamlines in the moving frame of reference
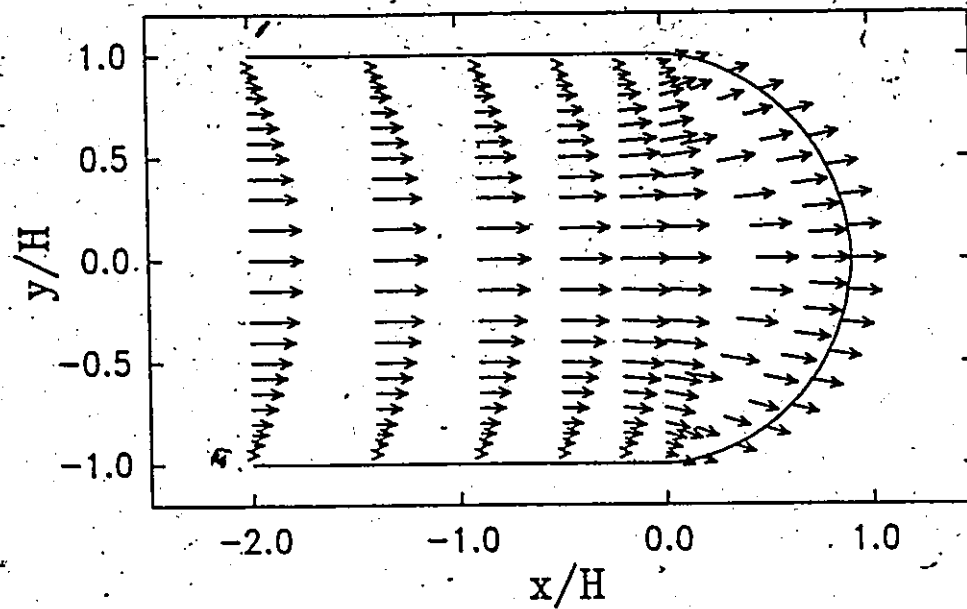
Figure 3.9   Velocity vectors in the fixed frame of reference
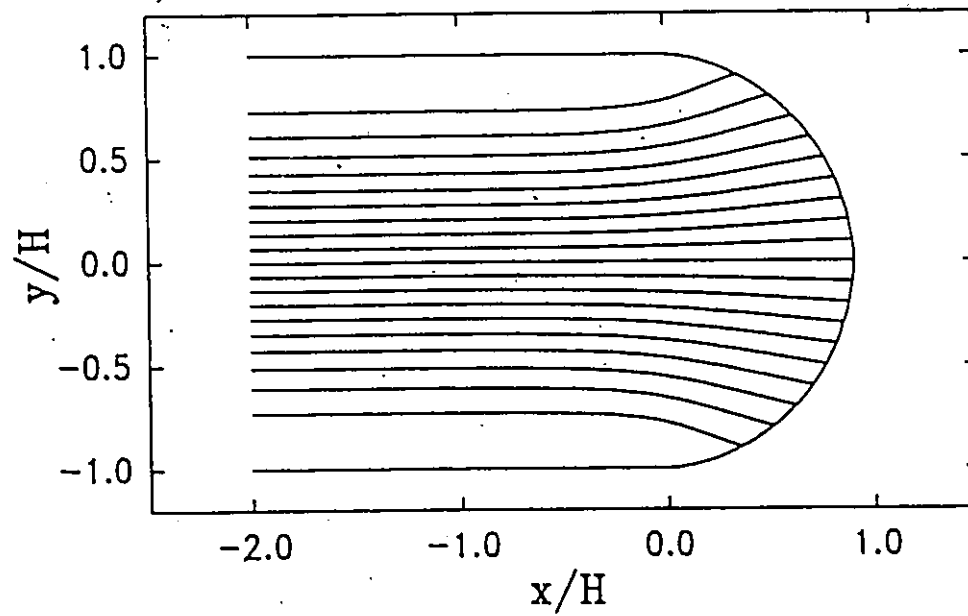
Figure 3.10   Streamlines in the fixed frame of reference
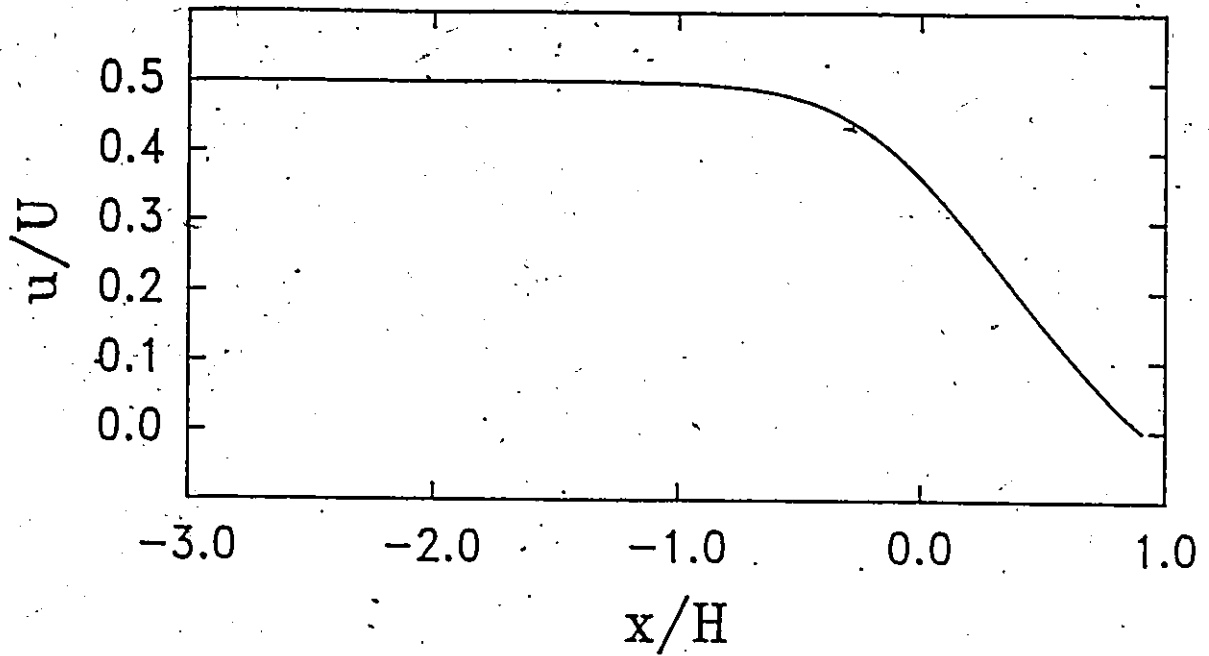
Figure 3.11   Velocity variation along the centerline
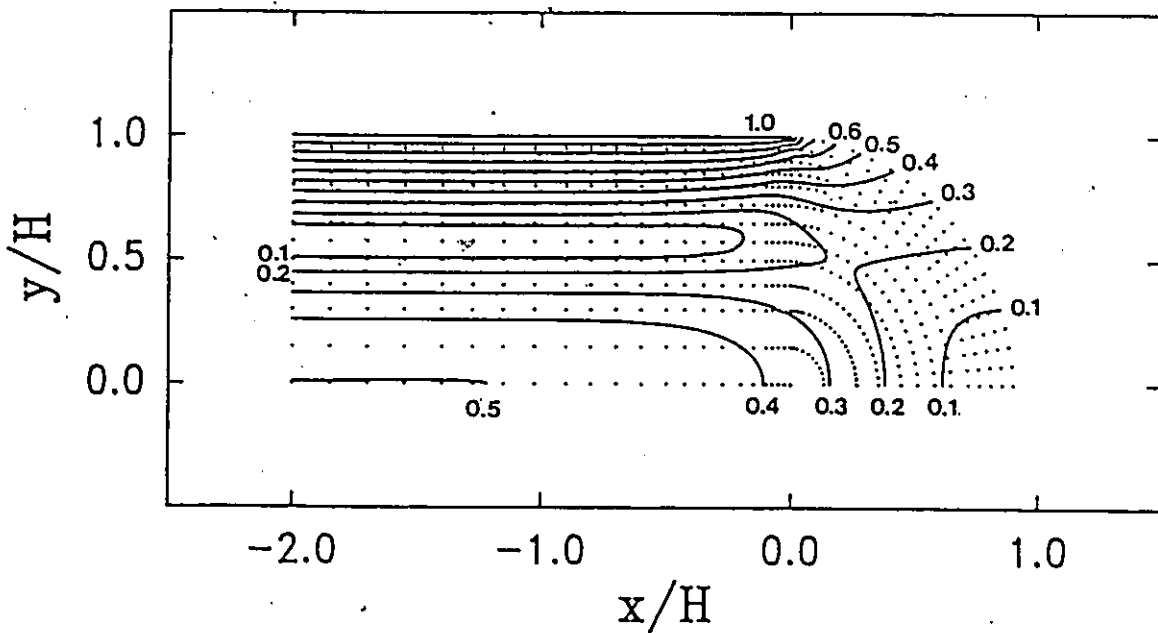
Figure 3.12   Contours of total fluid velocity $(u^2 + v^2)^{1/2}$, in the moving frame of reference

show the velocity variation over the flow domain and the stagnation flow region in the immediate vicinity of the front tip.

The pressure variation along the centerline and along the wall and free surface is given in Figures 3.13a and 3.13b respectively. The pressure drops linearly in the upstream region and is smooth along the centerline, while it exhibits an anomalous behavior near the contact line, due to a singularity in that region. In fact, all stress components are singular at the contact line. It is well known (Huh & Scriven, 1971; Dussan, 1979) that the continuum approach along with the no-slip condition breaks down in the vicinity of contact lines giving rise to singular stresses. Singular stresses can be tolerated, however, as long as they are integrable, i.e. the total drag exerted on the wall remains finite. In the present case the contact angle is 180° and the stress singularity is integrable (Pismen & Nir, 1982). It is possible to alleviate the stress singularity with a slip boundary condition. This remedy is investigated in the next section.

It is of interest to note the extra pressure drop due to the fountain flow. We define:

$$\Delta P_{extra} \equiv \Delta P(-L) - \Delta P_0(-L) \tag{3.30}$$

where $\Delta P(-L)$ is the calculated pressure drop over a length L behind the contact line and $\Delta P_0(-L)$ is the pressure drop that would be observed in Poisseuille flow over the same length. It was found that $\Delta P_{extra} = 0.6$ in units of $\mu_0 U/H$. This amounts to 10% of the pressure drop over a unit gapwidth and is too small to be significant in the actual mold filling process. Global quantities as the pressure drop are little affected by fountain flow whose main effect is on small scale phenomena (flow induced deformation of the material) as it will be shown in subsequent sections.
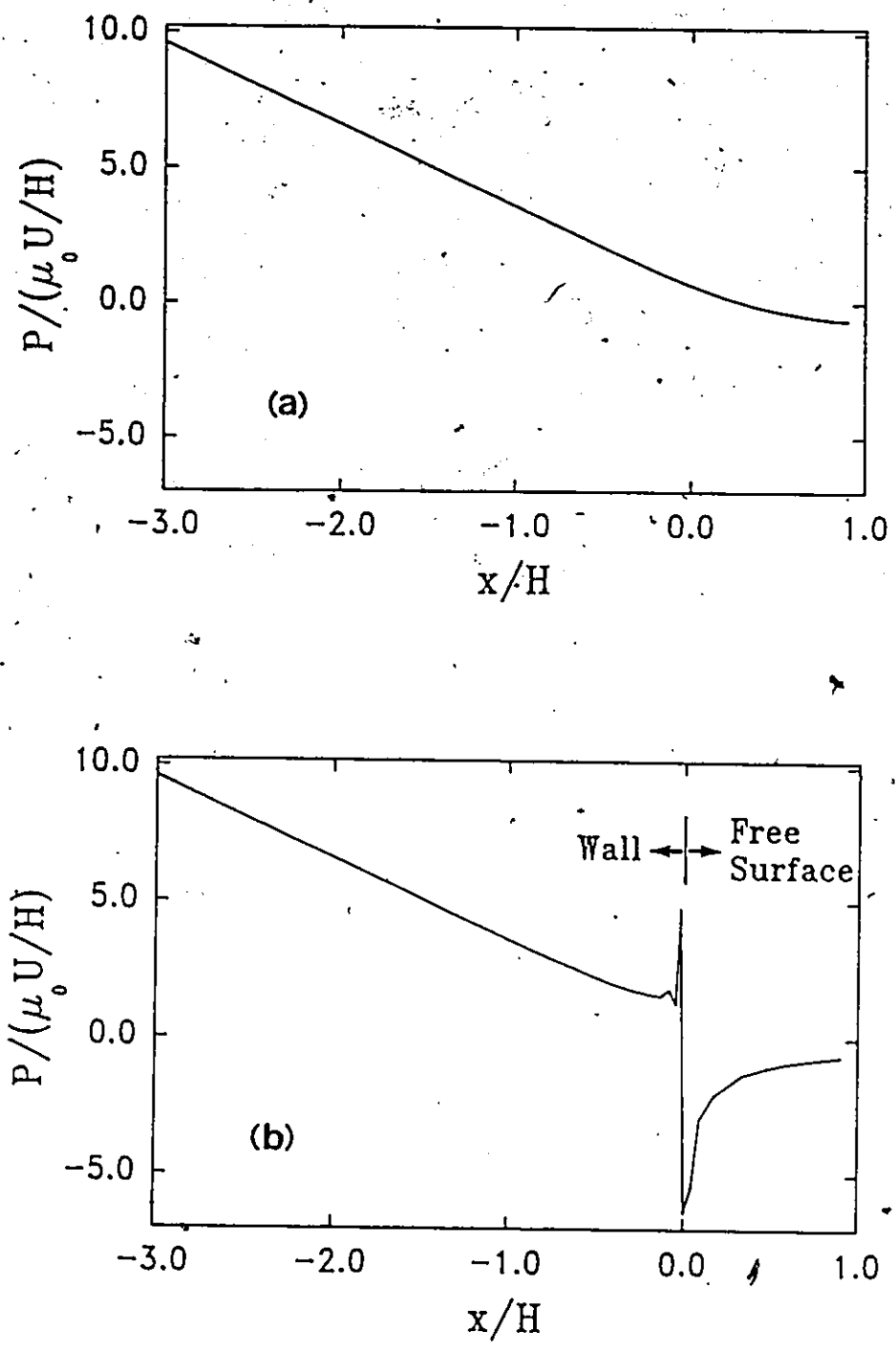
Figure 3.13   Pressure variation along the centerline, (a), and along the wall and free surface, (b)

3.2.3.2 Effect of slip boundary condition

The use of a slip boundary condition has been suggested by several researchers (Huh & Scriven, 1971; Huh & Mason, 1977; Dussan, 1979; Silliman & Scriven, 1980) to alleviate the stress singularity at the contact line. The slip boundary condition is a kind of an interfacial constitutive equation that relates the magnitude of the slip velocity u_s to the applied wall stress τ_w. The simplest approach is the Navier boundary condition:

$$u_s = \beta \tau_w \tag{3.31}$$

where β is the slip coefficient in units of m/Pa·s. The product $\beta\mu$, where μ is the viscosity of the fluid defines a length scale that measures extent of wall surface over which slip is significant. The ratio $B = \beta\mu/H$, where H is the length scale of the flow problem (here the half-gapwidth) is a dimensionless measure of slip, which is typically a small number below unity. For example, Ramamurthy (1986) measured slip velocities in the order of $u_s \approx 10^{-3}$ m/s for wall stress $\tau_w \approx 10^5$ Pa. Based on these measurements, the Navier boundary condition, eq.(3.31), gives a slip coefficient $\beta = 10^{-8}$ m/Pa·s. For a typical melt viscosity of $\mu = 10^3$ Pa·s and a half-gapwidth of $H = 10^{-3}$ m, the dimensionless slip group is $B = \beta\mu/H = 0.01$.

Other options for the slip boundary condition, usually power-law modifications of eq.(3.31) empirically fitted to experimental data, are also available (Chauffoureaux et al, 1979; Lau & Schowalter, 1986). Recently, the subject of slip at the wall received special attention due to its relevance in polymer flow instabilities (Ramamurthy, 1986; Kalika & Denn ,1987) and the breakdown of viscoelastic computations (Lipscomb et al, 1987).

In the present work the linear form of the slip boundary condition, eq.(3.31), was used. The power-law version can easily be implemented by treating the slip coefficient β as a nonlinear parameter instead of a constant. The dimensionless form of the slip condition as applied to the fountain flow problem is:

$$\tau_{xy}(y/H = 1) = -\frac{1}{B}(u + 1) \tag{3.32}$$

This condition is implemented in the finite element algorithm as follows. The x-momentum residual is (from eq.3.14):

$$R^i_{mx} = \int_\Omega \left\{ \phi^i \, Re\,(uu_x + vu_y) + (-P + 2\mu u_x)\phi^i_x + \mu(u_y + v_x)\phi^i_y \right.$$
$$\left. - \phi_i S^{-1}g_x \right\} d\Omega - \int_{\partial\Omega} \tau_{xy} \phi^i \, d\ell = 0$$

(3.33)

When the no-slip condition is applied this residual is deleted and the u-velocity is fixed with an essential boundary condition. When the slip boundary condition is applied the u-velocity at the wall is unknown. The τ_{xy} term in eq.(3.33) is substituted from eq.(3.32):

$$R^i_{mx} = \int_\Omega \left\{ \phi^i \, Re\,(uu_x + vu_y) + (-P + 2\mu u_x)\phi^i_x + \mu(u_y + v_x)\phi^i_y \right.$$
$$\left. - \phi_i S^{-1}g_x \right\} d\Omega + \int_{\partial\Omega} \frac{1}{B}(u + 1)\,\phi^i \, d\ell = 0$$

(3.34)

The above provides as many algebraic equations as there are nodal points along the wall, for the determination of the nodal slip velocities.

The appropriate velocity profile to be specified at the inlet boundary is:

$$u(y)/U = \frac{B}{B + 1/3} + \frac{1}{1 + 3B} \frac{3}{2} [1 - (y/H)^2] - 1$$

(3.35)

It can be seen from eq.(3.35) that the limit $B \to 0$ recovers the well-known Poiseuille profile (no-slip) while the limit $B \to \infty$ gives a plug velocity profile (perfect slip).

Finite element calculations were performed with MESH 2 (Figure 3.6) and the parameter B was varied in the range $10^{-4} - 10^{-1}$. A representative plot of the behavior of the computed solution with B is given in Figure 3.14. This figure shows the effect of slip on the calculated pressure value at the contact line and on the calculated front tip position (i.e., the flow front / centerline intersection). Up to B = 0.005 the results are unaffected by the slip condition. Increasing further the amount of slip decreases the pressure peak at the contact line, alleviating the stress singularity and also flattens the flow front shape (decreasing front tip position). Particularly important is the result that for a reasonable amount of slip (e.g. B
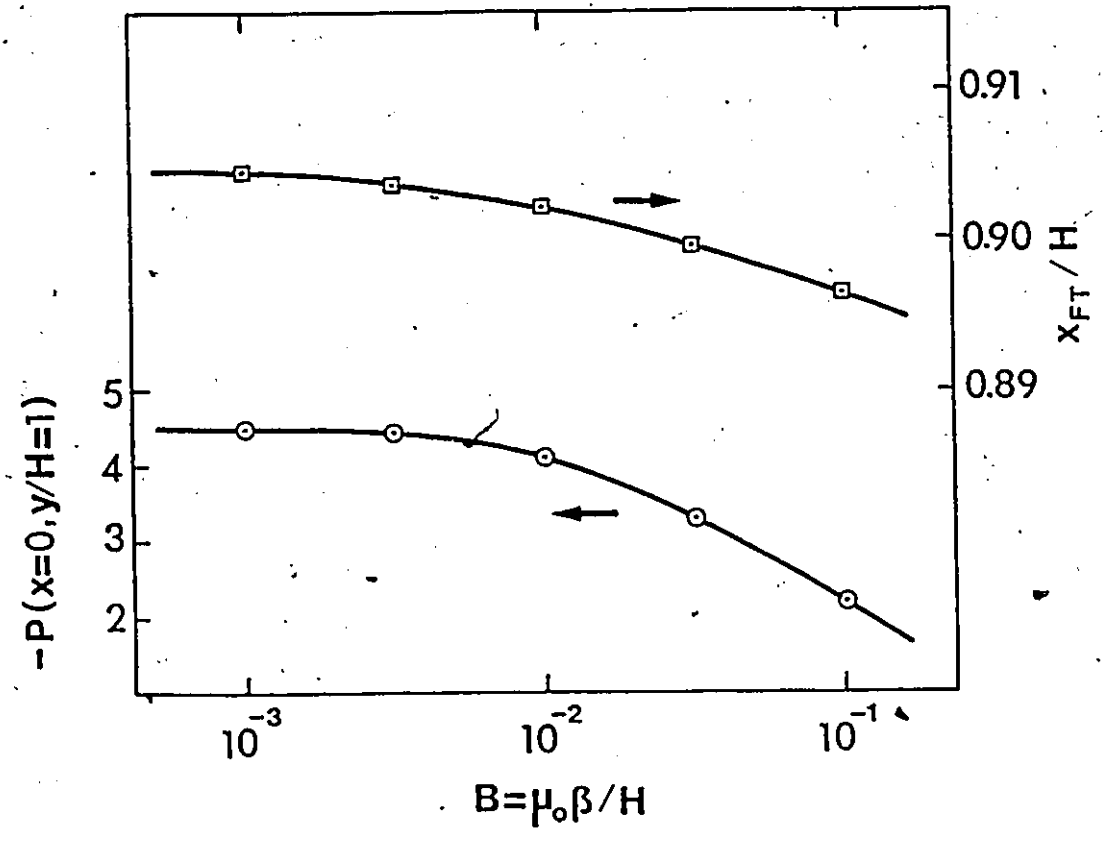
Figure 3.14   Effect of slip on the calculated pressure at the contact line, and on the front tip position

< 0.01) incorporation of a slip boundary condition does not affect the results, thus eliminating the need to account for an additional (and uncertain) parameter as the slip coefficient. Consequently, all further computations were performed with the no-slip condition.

3.2.3.3   Axisymmetric Geometry

Fountain flow simulations were also performed for axisymmetric tube flow. A fully developed velocity profile was imposed at the inflow plane (AD in Figure 3.3):

$$u/U = 2[1 - (r/R)^2] - 1 \tag{3.36}$$

and the finite element method of Section 3.2.2, properly modified for an axisymmetric coordinate system, was applied to obtain the flow field and the free surface shape.

The results were qualitatively the same as those for planar flow. The deformed finite element grid and the streamlines are given in Figure 3.15. The flow becomes fully developed (i.e. the velocity at the centerline attains 99% of the upstream value) at $z/R = 0.786$ behind the contact line. The calculated shapes of the flow front for the planar and axisymmetric geometry are compared to a circular shape in Figure 3.16. Table 3.2 lists the coordinates of the nodal points defining the flow front shape.

A characteristic measure of the flow front shape is the axial distance between the contact line and the front tip. Table 3.3 lists the values calculated by various investigators. The reported values show some variation from each other, probably due to the different meshes employed and the iterative techniques for free surface determination. The present results have been verified with mesh refinement and both u-v-p-h-δ (present work) and u-v-p (Mavridis et al, 1986a) formulations. It is noted that for the axisymmetric case there is good agreement with the experimental results of Behrens et al (1987).
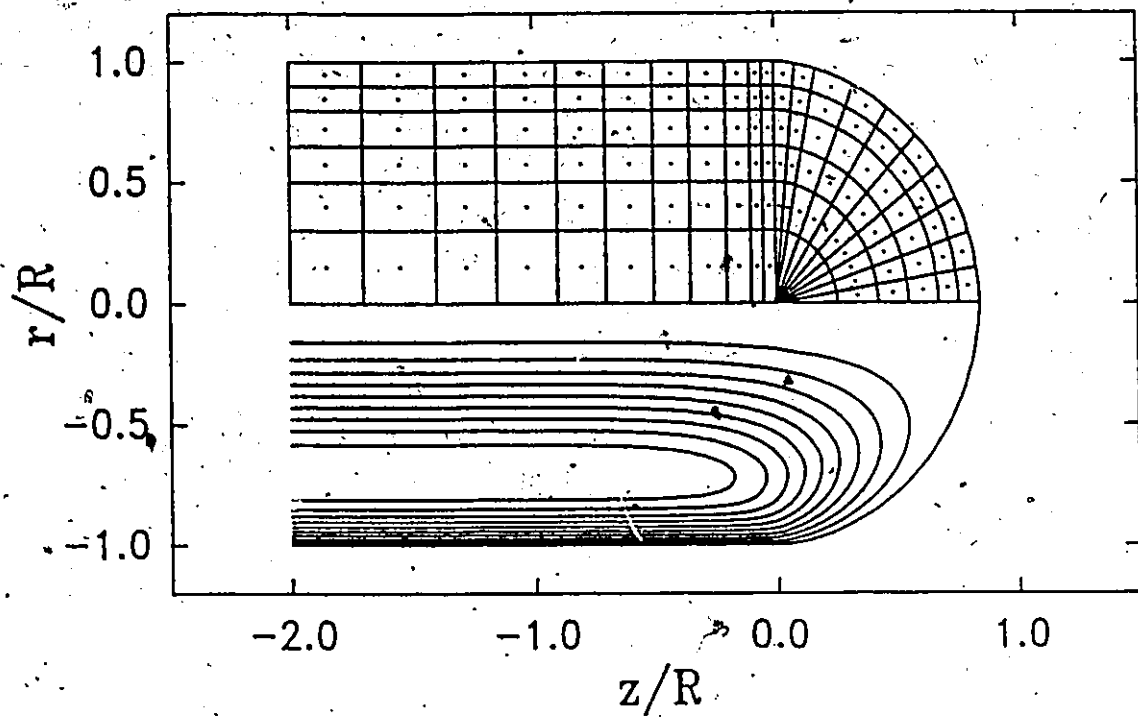
Figure 3.15   Finite element grid and streamlines for axisymmetric fountain flow
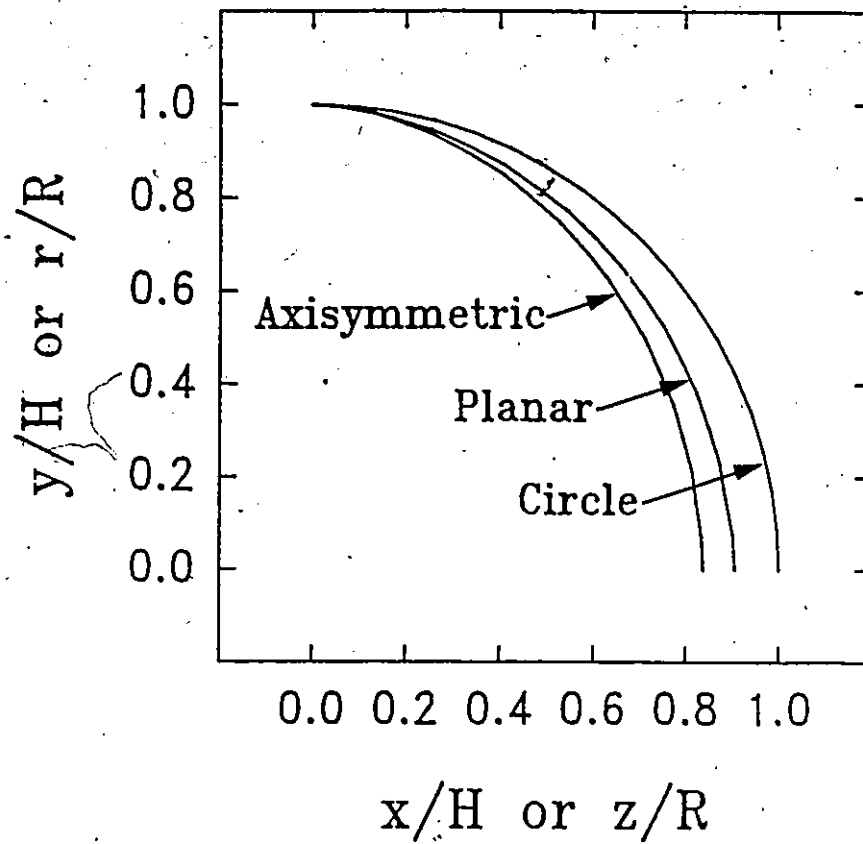
Figure 3.16   Flow front shape in planar and axisymmetric geometry (Newtonian fluid)

Table 3.2 Polar coordinates of the flow front for planar and axisymmetric fountain

flow (Newtonian fluid, MESH 2 of Fig. 3.6)

Angle, degrees	Polar Radius	
	Planar	Axisymmetric
0	0.90516	0.83762
5	0.90357	0.83700
10	0.89870	0.83508
15	0.90281	0.84103
20	0.90271	0.84361
25	0.90821	0.85229
30	0.91047	0.85791
35	0.91736	0.86903
40	0.92152	0.87734
45	0.92970	0.89059
50	0.93540	0.90104
55	0.94465	0.91594
60	0.95159	0.92799
65	0.96150	0.94352
70	0.96899	0.95576
75	0.97909	0.97086
80	0.98675	0.98237
85	0.99378	0.99210
90	1.0	1.0

Table 3.3 Axial (Front Tip - Contact Line) distance for planar and axisymmetric geometries.

Investigator	Geometry	Method	$(x_{FT}-x_{CL})/H$ or $(z_{FT}-z_{CL})/R$
Present Work	Planar	FEM, u-v-p-h-δ	0.905
Mavridis et al,1986a	Planar	FEM, u-v-p	0.90
Behrens et al,1987	Planar	FEM, u-v-p	0,94
Givler et al,1983	Planar	FEM, u-v-p	0.96
Wang et al,1978	Planar	FEM, u-v-p	1.04
Wang et al,1979	Planar	FEM, u-v-p	0.84
Present Work	Axisymm.	FEM, u-v-p-h-δ	0.837
Mavridis et al,1986a	Axisymm.	FEM, u-v-p	0.83
Behrens et al,1987	Axisymm.	FEM, u-v-p	0.82
Behrens et al,1987	Axisymm.	Experiment	0.83 $\pm$ 0.04

Behrens et al (1987) used the results of their finite element calculations to evaluate Tadmor's (1974) stagnation flow model behind the flow front. Tadmor (1974), in his semiquantitative study of the effect of fountain flow on molecular orientation, was interested in obtaining an estimate of the elongational deformation in the deceleration region behind the flow front. In that region the velocity along the centerline drops smoothly from its maximum value upstream to its average value at the front tip (Figure 3.17). Tadmor (1974) suggested modeling this flow region as stagnation flow over some distance L_{stag} behind the flow front. In this approximation the velocity drops linearly from its maximum value at $x_{FT}-L_{stag}$ to its average value at x_{FT}, as shown schematically in Figure 3.17. Then, the
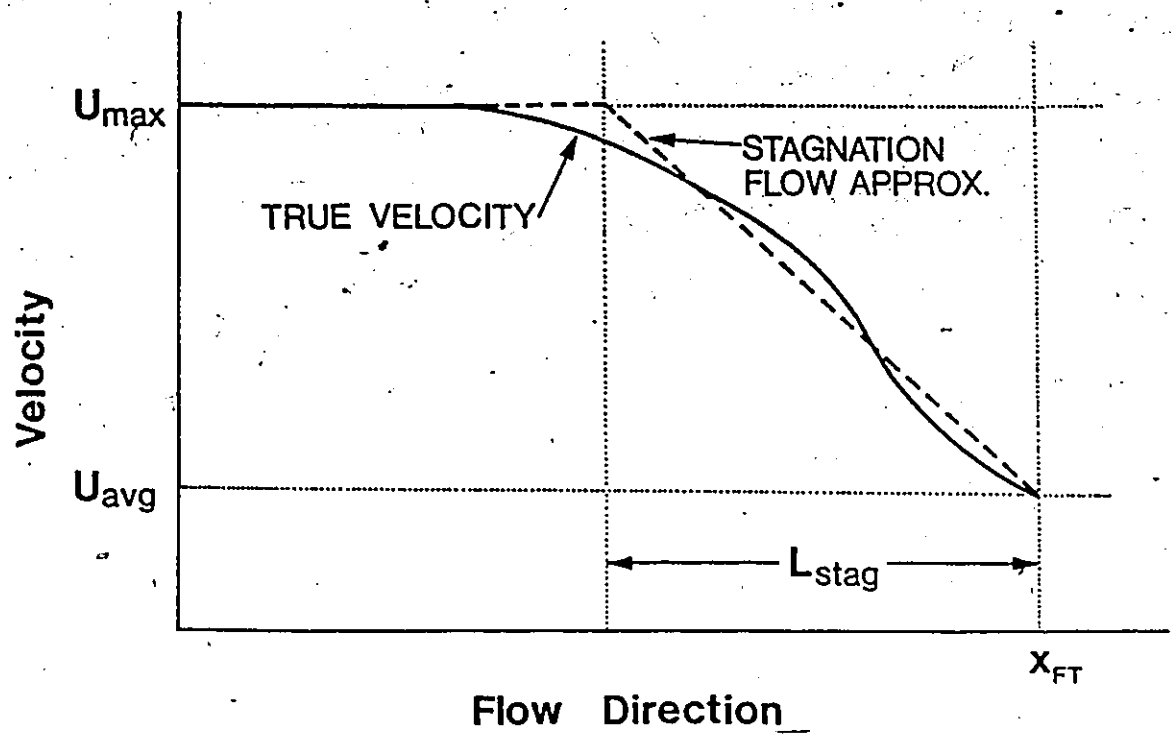
Figure 3.17   Definition sketch for stagnation flow model

elongational deformation $-\dot{\varepsilon}_{11} = du/dx$ is:

$$\dot{\varepsilon}_{11} = \frac{U_{max} - U}{L_{stag}} \qquad (3.37)$$

Tadmor (1974) assumed L_{stag} to be equal to the gapwidth 2H ($L_{stag} = 2R$, the tube diameter in the axisymmetric case). Then for a Newtonian fluid ($U_{max} = 1.5U$ for planar and $U_{max} = 2U$ for axisymmetric flow) eq.(3.37) is simply:

Planar   geometry   : $\dot{\varepsilon}_{11} = 0.25$ U/H   (3.38a)

Axisymm.   geometry   : $\dot{\varepsilon}_{11} = 0.50$ U/R   (3.38b)

Behrens et al (1987) compared eqs.(3.38) with their finite element predictions and found that eqs.(3.38) provide a reasonable approximation after some adjustment of the numerical coefficients. The adjustment is based on the computed velocity field and front tip position. Referring to Figure 3.17, and with the velocity curve known, the only adjustable parameter of the stagnation flow model is the extent of the stagnation flow region L_{stag}. This can be determined by equating the areas under the two velocity curves in Figure 3.17. Based on the results of the present work this calculation gives:

Planar   Geometry   : $L_{stag} = 1.322$ H

Axisymm.   Geometry   : $L_{stag} = 1.302$ R

and the adjusted form of eq.(3.38) is:

Planar   Geometry   : $\dot{\varepsilon}_{11} = 0.378$ U/H   (3.39a)

Axisymm.   Geometry   : $\dot{\varepsilon}_{11} = 0.768$ U/R   (3.39b)
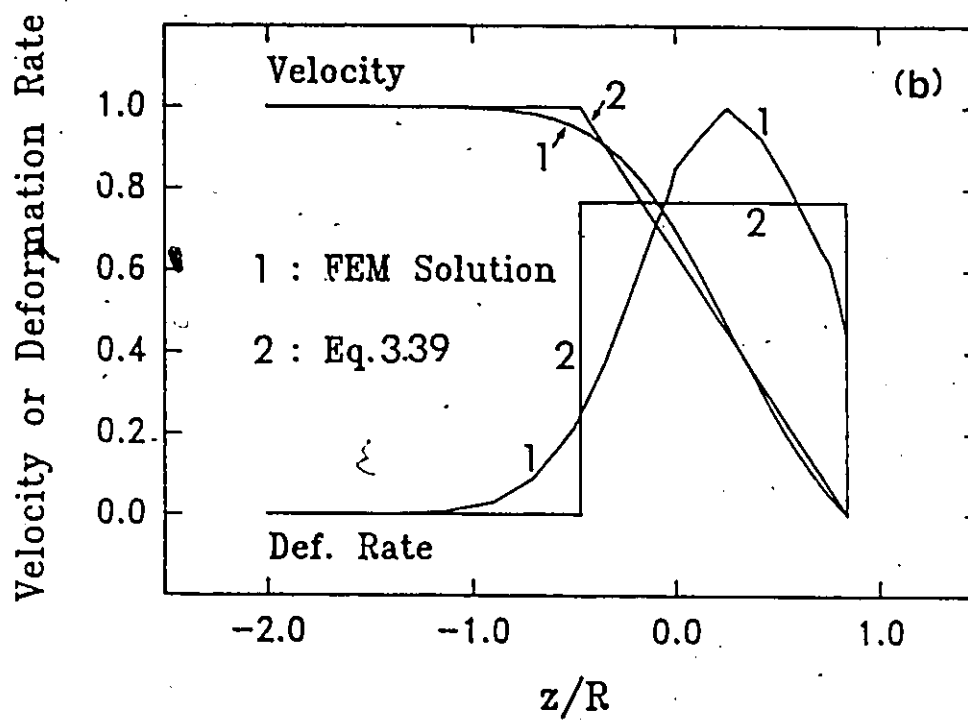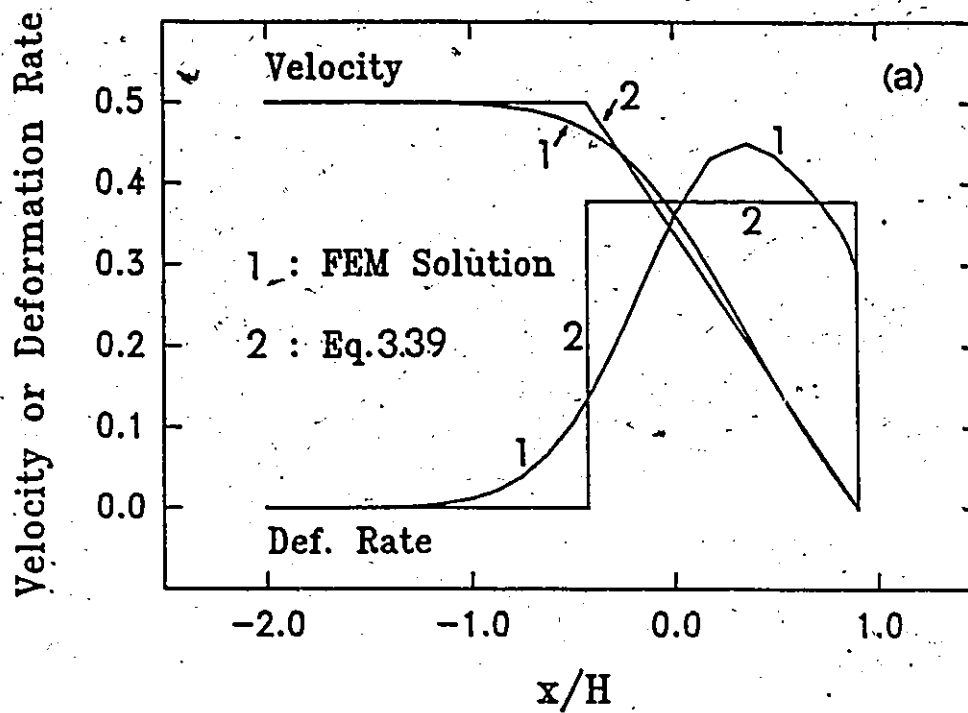
Figure 3.18   Evaluation of stagnation flow model:
(a) planar, (b) axisymmetric geometry

The adjusted numerical coefficients 0.378 and 0.768 in eqs.(3.39) compare very well with those reported by Behrens et al (1987); 0.38 and 0.75 respectively. A graphical comparison of the calculated profiles (finite element method, present work) and the stagnation flow approximations (eqs.3.39) is shown in Figures 3.18a and 3.18b, for planar and axisymmetric flow respectively. It can be seen that while the velocity is reasonably well approximated by stagnation flow, the deformation rate predicted by eqs.(3.39) provides only an average estimate of a complex deformation rate profile. The strength of the present finite element approach is that it can provide detailed information about both the kinematics and the dynamics of the flow with no need to resort to simplifying approximations. This will be demonstrated more clearly in Section 3.3 when investigating the deformation experienced by the fluid and further in Chapter 5, where the impact of fountain flow on molecular orientation is examined.

3.2.4 Shear-Thinning Fluids

Fountain flow simulations were also performed with a shear-rate dependent viscosity to investigate the effect of shear thinning. The Carreau viscosity model (Bird et al, 1977) was used:

$$\mu/\mu_0 = \left[1 + (\lambda\dot{\gamma})^2 \right]^{(n-1)/2} \tag{3.40}$$

with the material constants:

$$\mu_0 = 9500 \, \text{Pa}-\text{s}$$

$$\lambda = 1.148 \, \text{s} \tag{3.41}$$

$$n = 0.5$$

The viscosity function eq.(3.40) with the constants of eq.(3.41) describes the behavior of a typical polymer melt (polystyrene, Dow Styron 678U, at 180°C) over four decades of shear rates (Mitsoulis, 1984). The viscosity curve is plotted in Figure 3.19. The

$$\mu/\mu_0 = \left[1+(\lambda\dot{\gamma})^2\right]^{(n-1)/2}$$

CARREAU MODEL

Viscosity, μ/μ_0

Shear Rate, $\dot{\gamma}$, s^{-1}
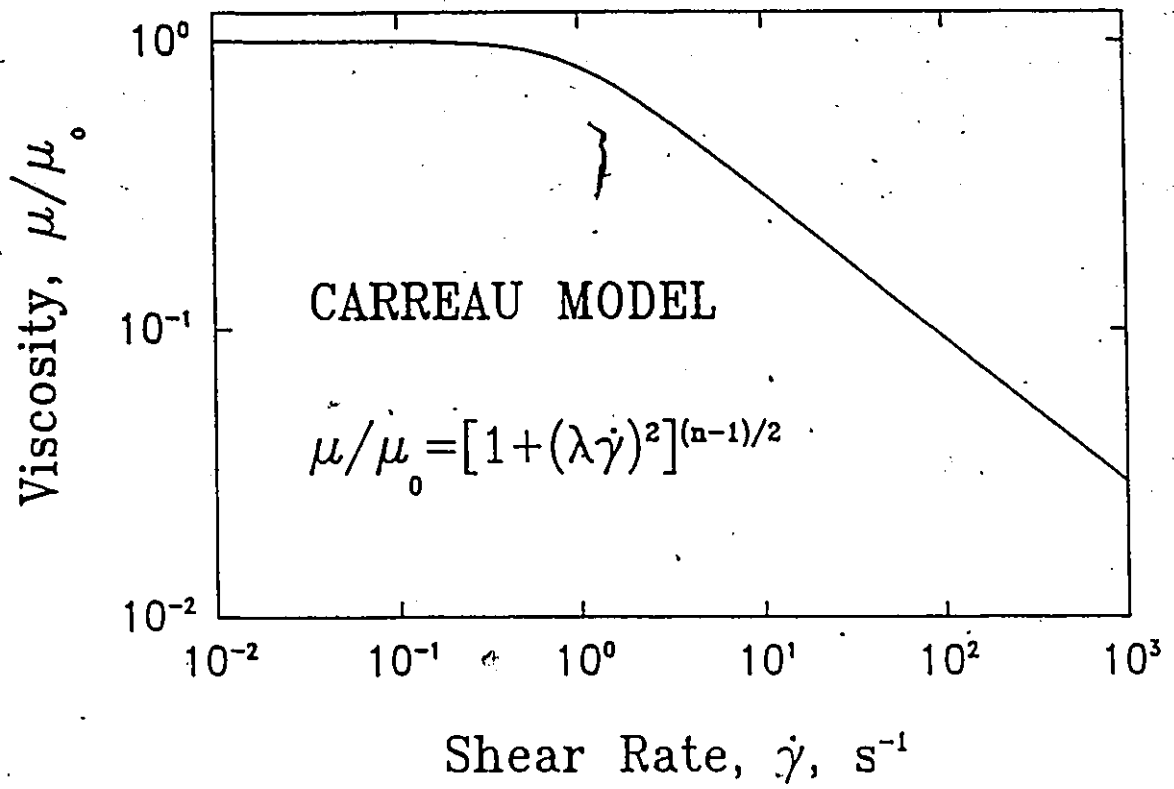
Figure 3.19   Viscosity curve for a Carreau fluid (parameters of eq.3.41)
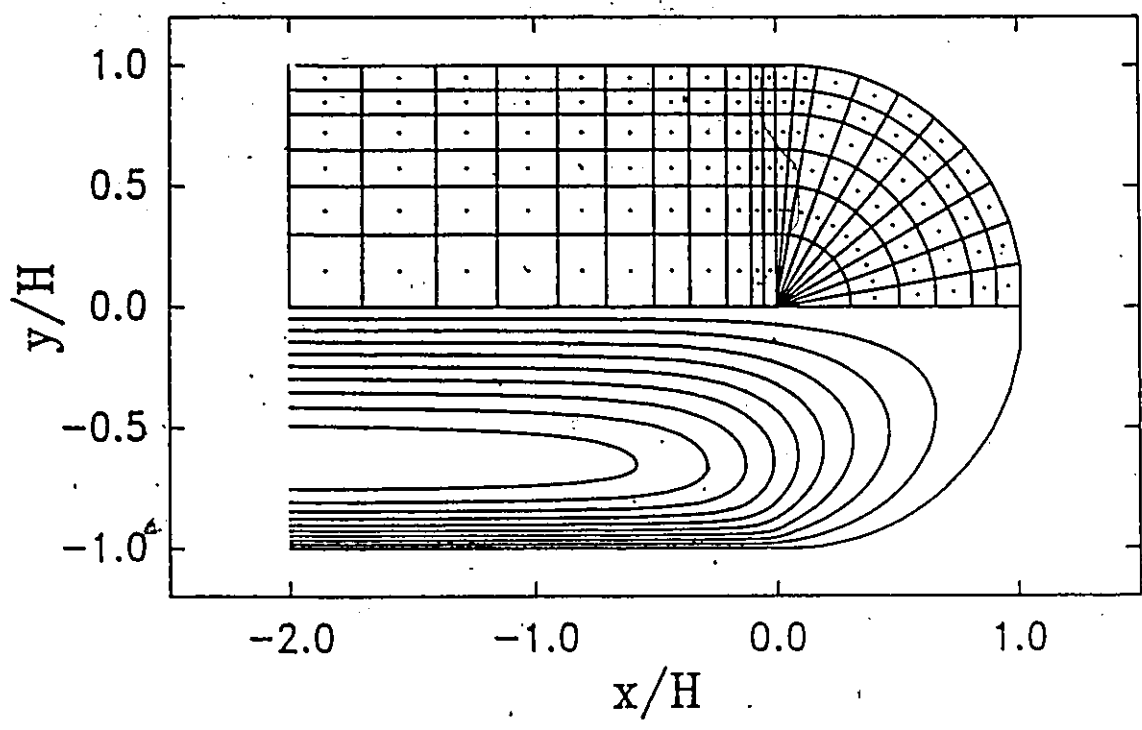
Figure 3.20   Finite element grid and streamlines for fountain flow of a Carreau fluid ($\dot{\gamma}_w = 100$ s^{-1}, planar geometry, parameters of eq.3.41)
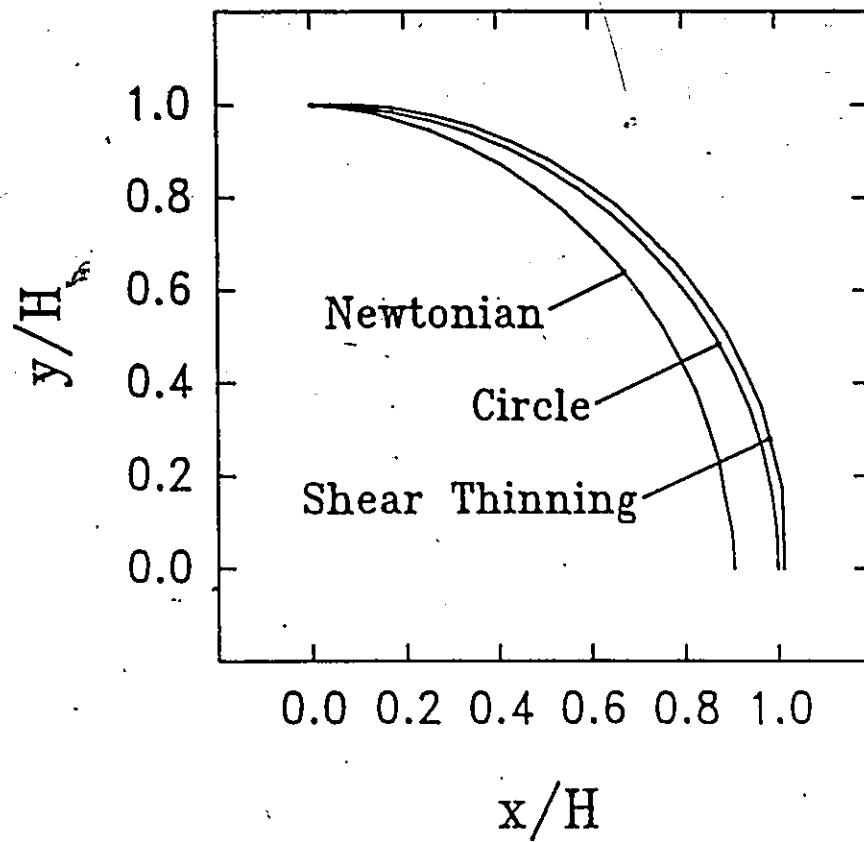
Figure 3.21   Flow front shape for Newtonian and shear-thinning fluid (planar geometry, shear-thinning parameters as in Figure 3.20)

material is Newtonian at low shear rates and exhibits a power-law behavior at high shear rates. A smooth transition is observed at $\dot{\gamma} \approx 1\,\mathrm{s}^{-1}$.

Finite element calculations with the Carreau viscosity function were performed on MESH 2 (Figure 3.6) for wall shear rates in the range $\dot{\gamma}_w = 10^{-2} - 10^3\,\mathrm{s}^{-1}$. Up to $\dot{\gamma}_w = 1$ s^{-1} (transition region of the viscosity function) the results were indistinguishable from the Newtonian solution. Observable differences were noted only for high shear rates (in the power—law region). Figure 3.20 shows the deformed finite element grid and the streamlines for a wall shear rate of $\dot{\gamma}_w = 100\,\mathrm{s}^{-1}$. The same qualitative features of fountain flow as for Newtonian fluids were observed over the whole range of shear rates. Figure 3.21 shows a comparison of the flow front shape for a Newtonian and a shear thinning fluid (Carreau model, $\dot{\gamma}_w = 100\,\mathrm{s}^{-1}$). The shape for the shear thinning fluid is very close to a circle (the maximum deviation is 2%) as suggested by Tadmor (1974).

3.3 Deformation and Orientation of Fluid Elements Behind an Advancing Flow Front

3.3.1 Introduction

Extensive injection mold filling visualization experiments were reported by Schmidt (1974,1977,1981). He developed a special mold and tracer technique (Schmidt, 1974) that allowed on-line monitoring of the injection mold filling process. Schmidt applied this technique (Schmidt, 1977,1981) to investigate the flow patterns and the velocity and deformation of fluid elements in the mold cavity. The experimental apparatus consisted of a rectangular mold with glass walls attached to the reservoir of an Instron Capillary Rheometer. A cylindrical polymeric rod with color tracers inserted at specific locations along its centerline was loaded into the reservoir and injected into the mold. A schematic diagram of the experimental configuration and the mold geometry used by Schmidt is shown in Figure
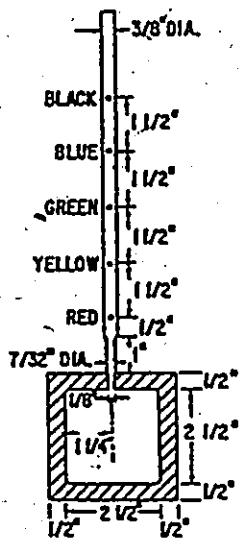
(a)
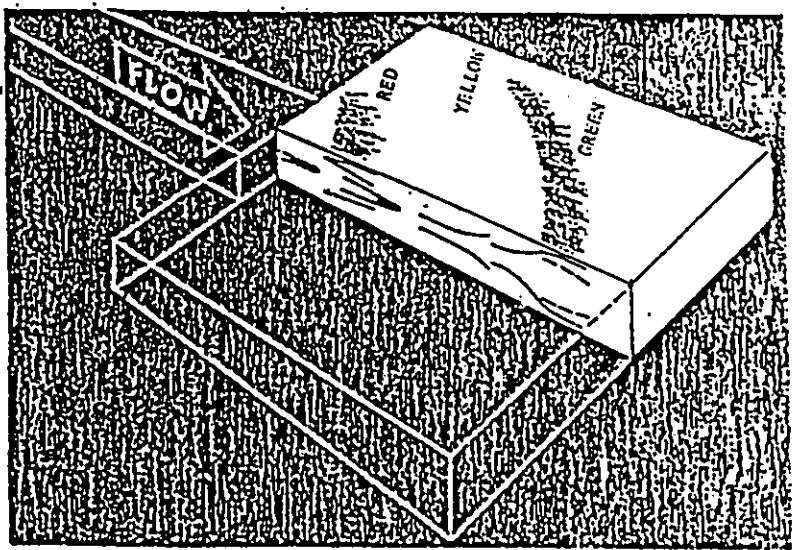
(b)

Figure 3.22   Schematic of (a) experimental apparatus, and (b) mold geometry, in Schmidt's (1974) experiments
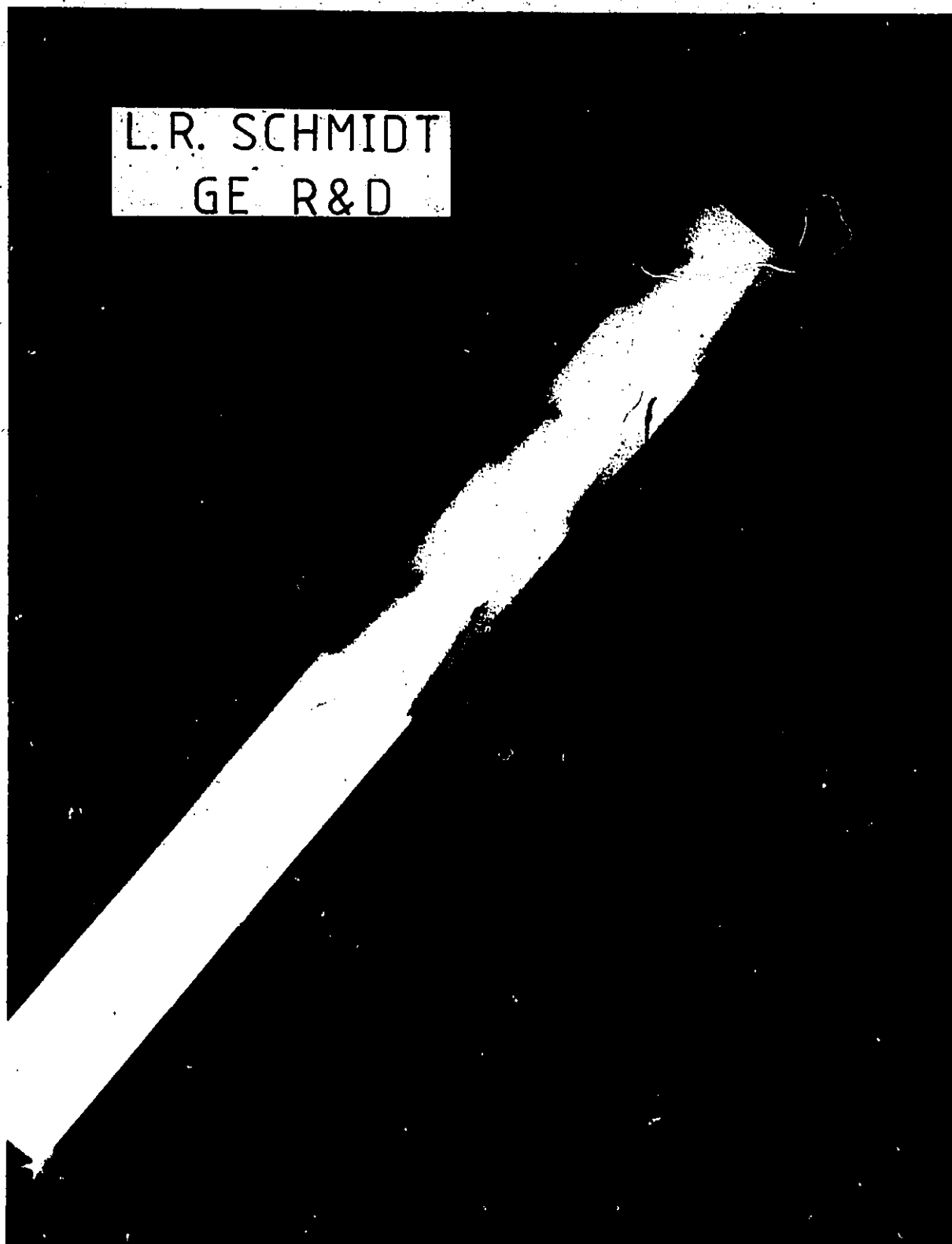
Figure 3.23   Cross section of molded plaque illustrating V-shaped color tracers. Flow was from left to right (Courtesy of L.R. Schmidt)

3.22. Typical results of the visualization experiments of Schmidt (1974) are shown in Figure 3.23, which is an experimental photograph of the cross-section of the molded plaque (thickness direction). The photograph shows that the color tracers, originally placed along the centerline, are split symmetrically and found at the outer surfaces of the mold deformed into characteristic V-shapes, with the tip of the V-mark pointing towards the gate.

Schmidt (1974) acknowledged the importance of fountain flow on the observed deformation of the color tracers. The Marker-and-Cell simulations of Huang (1978) and Huang et al (1986) captured the fluid element deformation but attributed the V-shape formation to freezing at the cold wall. The numerical tracking investigations of the present work showed for the first time (Mavridis et al, 1986b) that fountain flow is responsible for the observed tracer deformation: the V-shape formation is primary and the freezing at the wall that immobilizes the tracers is secondary. The numerical tracking of fluid elements is considered below.

3.3.2   Numerical Tracking of Fluid Elements

The finite element solution of the fountain flow problem provides the detailed velocity field in terms of velocity components at the nodes of the discretized flow domain. Tracking of a material point, or a material element in general, as it moves through the flow field is a simple post-processing operation based on the computed velocity field.

Consider a material point P which at time t=0 is at position (x_{P0}, y_{P0}). The coordinates (x,y) refer to the moving frame of reference. The trajectory of the material point, in the moving frame of reference, can be described mathematically by the initial value problem:

$$\frac{d}{dt}\begin{pmatrix} x \\ y \end{pmatrix} = \begin{pmatrix} u \\ v \end{pmatrix} \tag{3.42}$$

$$\begin{pmatrix} x_P \\ y_P \end{pmatrix} = \begin{pmatrix} x_{Po} \\ y_{Po} \end{pmatrix} \text{ at } t = 0 \tag{3.43}$$

where u,v are the x- and y-components of velocity in the moving frame of reference. The trajectory of the material point P in the fixed frame of reference can be obtained from:

$$x_{fP}(t) = x_P(t) + Ut \tag{3.44}$$

$$y_{fP}(t) = y_P(t)$$

To obtain the trajectory of point P the system of eqs.(3.42) must be integrated numerically in time. The integration can be performed with any library routine for ordinary differential equations. The only complication is that the velocities in eqs.(3.42) are not known as continuous functions of position but as discrete values at the nodal points. For a given point $(x_P(t), y_P(t))$ at time t, the velocity components $u(x_P, y_P)$, $v(x_P, y_P)$ are evaluated through the following procedure:

(i)   A loop is made over all elements in order to identify the finite element the contains the given point (x_P, y_P). For this element the coordinates of the nodal points (x^i, y^i) and the corresponding velocity components (u^i, v^i) , $i = 1, N_e$ (where N_e is the number of nodes in the current element) are retrieved from the global list of nodal values.

(ii)   The local coordinates (ξ_P, η_P) of point P are found by solving:

$$x_P - \sum_{i=1}^{N_e} \phi^i (\xi_P, \eta_P) x^i = 0 \tag{3.45}$$

$$y_P - \sum_{i=1}^{N_e} \phi^i (\xi_P, \eta_P) y^i = 0$$

(iii)   The velocities at (x_P, y_P) are computed from:

$$u(x_p, y_p) = \sum_{i=1}^{N_e} \phi^i (\xi_p, \eta_p) u^i$$

$$v(x_p, y_p) = \sum_{i=1}^{N_e} \phi^i (\xi_p, \eta_p) v^i$$

(3.46)

For a fluid element the complete deformation history can be obtained by applying eqs.(3.42) for a large number of material points along the surface enclosing the element.

3.3.3 Results and Discussion

Results are shown in Figure 3.24 for a moving frame of reference. The half-gapwidth H is used a the length scale and H/U is used as the time scale, where U is the average velocity of the fluid. Figure 3.24 shows two symmetrically located fluid elements (with respect to the centerline) which become distorted and stretched as they move towards the wall, fully in agreement with Tadmor's (1974) sketch for a moving frame of reference. This figure also shows the characteristic splitting pattern of a fluid element along the centerline as it approaches the flow front. Material particles near the centerline decelerate as they approach the slower moving front. Mass continuity results in the development of a transverse (outward directed) velocity component that splits the fluid element and drives the symmetric parts away from the centerline. The deformed fluid elements move towards the wall following the flow front shape in a curved path. When they reach the walls they are extremely stretched and oriented in the flow direction, while the trailing edge forms the characteristic V-shapes observed in the experiments of Schmidt (1974).

The exact time and location for V-shape formation depends on the original size and position of the tracer element. Results for smaller fluid elements are shown in Figure 3.25, for a fixed frame of reference. The fluid elements deform as they approach the front (t=0 to t=8). The material point that was closer to the centerline moves faster, so it reaches first the
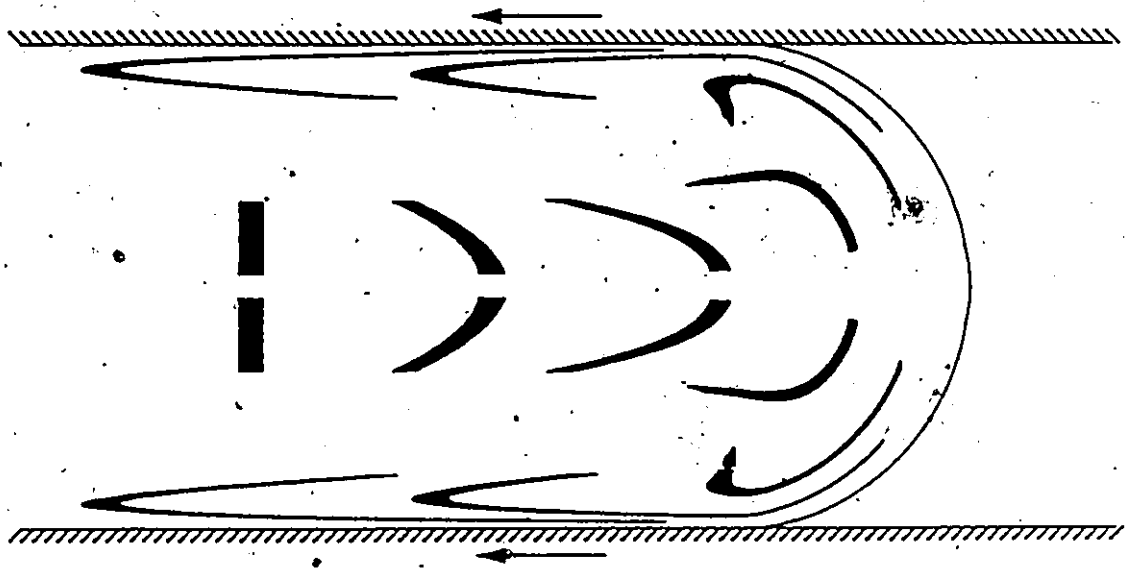
Figure 3.24   Deformation history of fluid elements in fountain flow (Newtonian fluid, moving frame of reference). Time interval between successive shapes is 2, in units of H/U
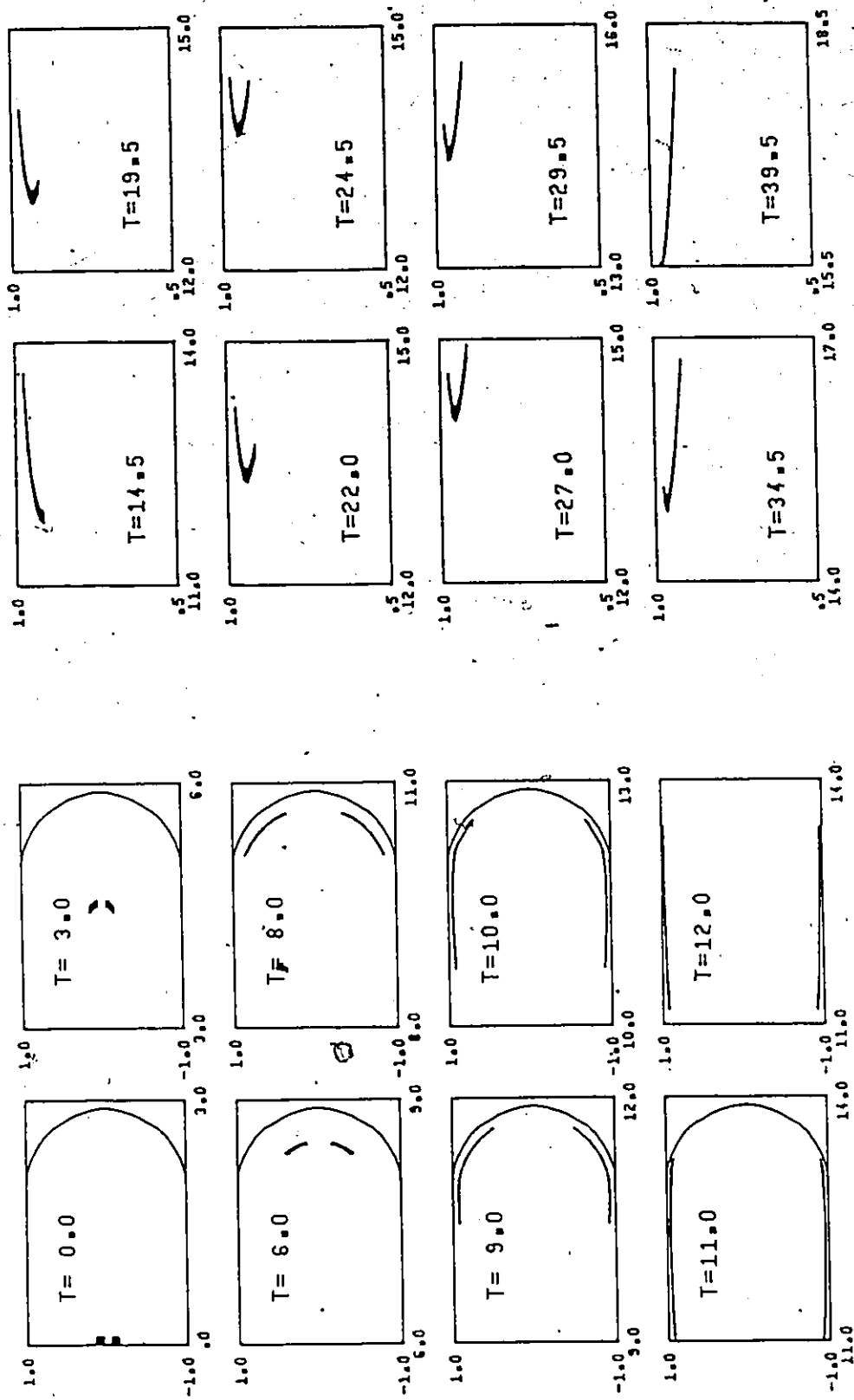
Figure 3.25 Deformation history of fluid elements in the fixed frame of reference (after 14.5 only the upper part is plotted, and the vertical scale is exaggerated by a factor of four)

(a)

(b)

TRANSVERSE DIRECTION

1.0

0.8

FLOW DIRECTION

14.25

15.75
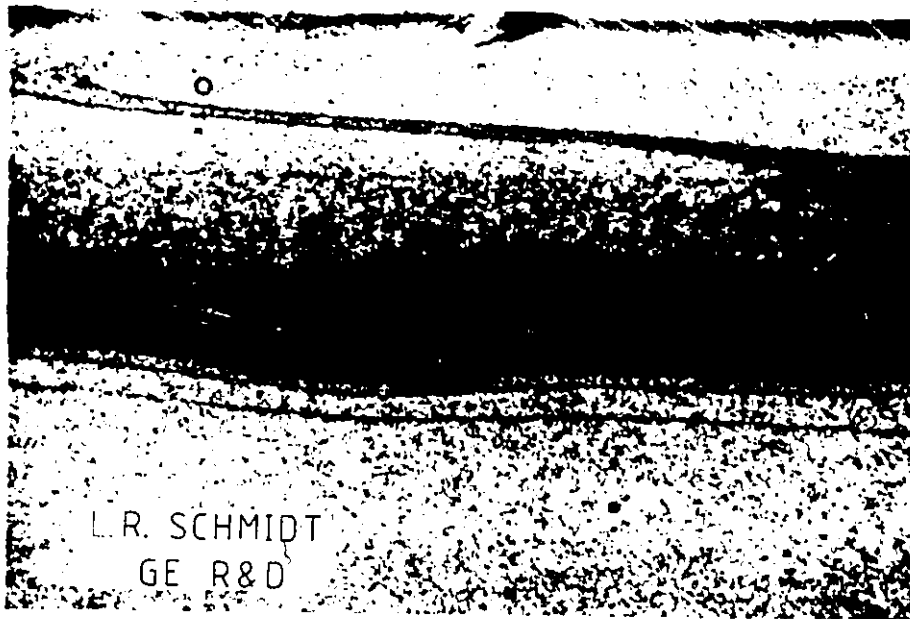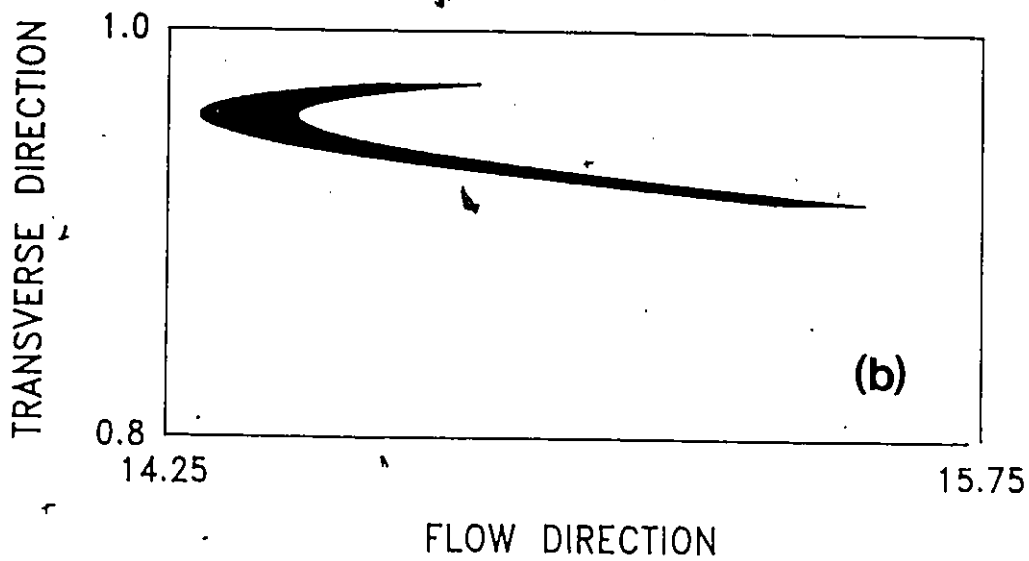
Figure 3.26   (a)   Enlargement of tracer region in the cross section of molded PBT plaque (Courtesy of L.R. Schmidt)

                (b)   Enlargement of the calculated fluid element shape at time = 29.5

flow front and then it moves towards the wall (t=8 to t≐11) where it becomes nearly stationary. At time t=12 the fluid element has completed half a turn and is mainly affected by shear flow since the flow front has moved forward. Under the effect of the shear flow the trailing edge moves forward, forming a "V" (t=14.5−t=34.5) through a rolling-type motion. The fact that such a motion can occur far behind the front is not surprising; fountain flow behind the advancing front is only responsible for the outward motion and the turning over for this particular element, while the subsequent formation of V-shapes is due to the shear flow in the fully developed region. The fluid elements eventually become nearly parallel to the wall (t=39.5). These predictions are fully in agreement with Schmidt's (1974) observations. In fact, the present results show that the formation of V-shapes occurs in isothermal flow. The formation of a frozen layer on the mold wall may also influence the appearance of the V-shapes according to Huang (1978) and Huang et al (1986).

Figure 3.26a is a photograph from Schmidt's (1977,1981) visualization experiments. The V-shaped tracer is shown on the upper part of the photograph and closely resembles the shape shown in Figure 3.26b, which is a magnification of the fluid element shape at time t=29.5 in Figure 3.25. The striking similarity suggests that fountain flow is responsible for this peculiar deformation of fluid elements. While it is possible that the non-Newtonian and non-isothermal characteristics of flow in Schmidt's experiments may influence the deformation mechanism, it appears that fountain flow is the main cause of this behavior.

Another important experimental finding of Schmidt (1974) was that the first tracer to enter the mold appears nearest to the gate when it reaches the mold wall, while the last tracer is found at the greatest distance from the gate. This is clearly illustrated in Figure 3.27 that shows the deformation of three tracer elements and how the sequence of the tracers is reversed when they reach the mold walls. As explained earlier, a material element moves
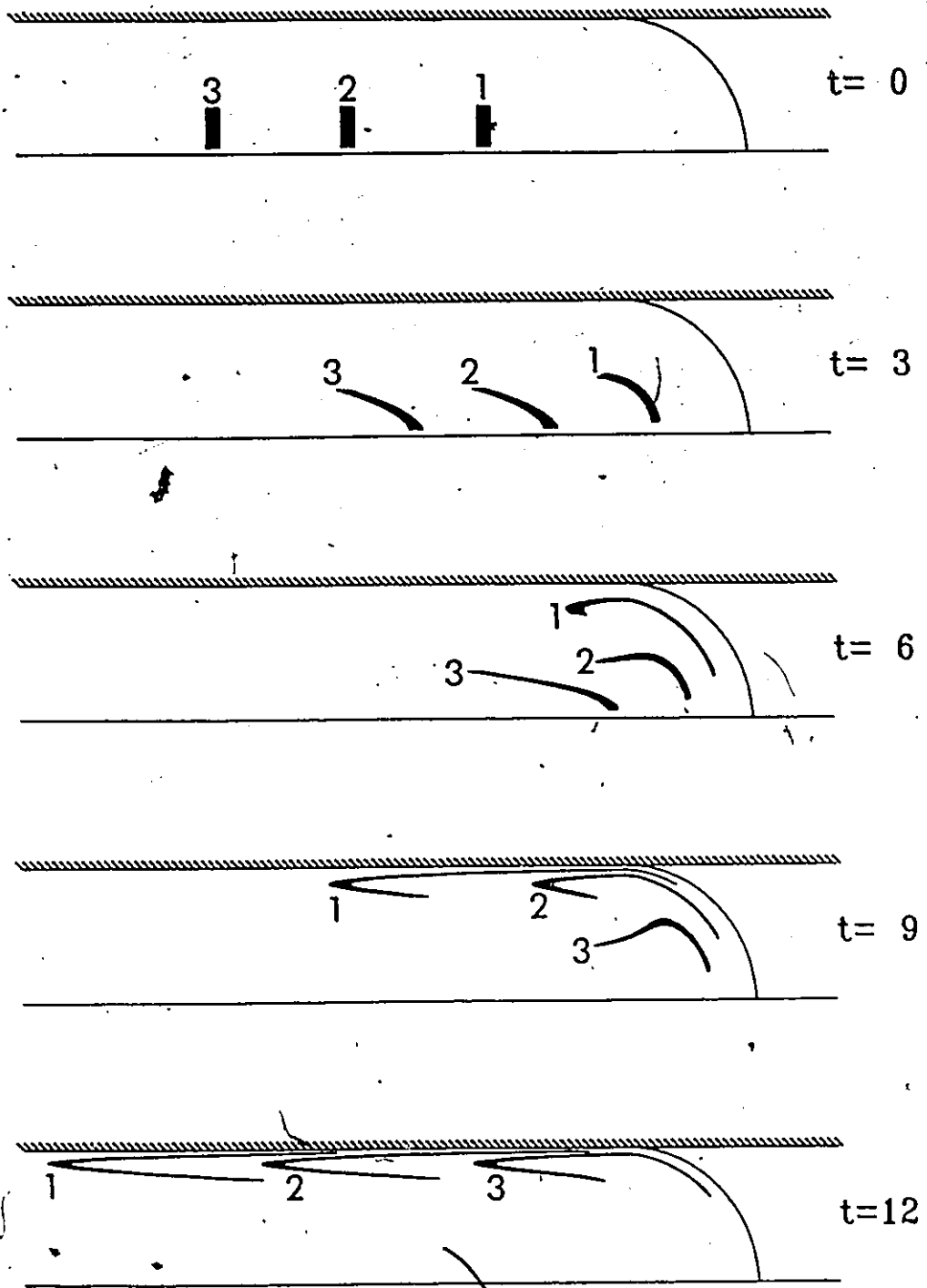
Figure 3.27   Fountain flow reverses tracer order

away from the centerline and eventually reaches the mold walls due to fountain flow behind the advancing front, the very essence of which is the existence of an outward directed transverse velocity component. Since the fountain flow region extends less than one gapwidth behind the front tip (see Section 3.2.3.1), fluid elements behind this region will be unaffected by fountain flow and continue to move parallel to the centerline. The later a tracer enters the mold the later it enters the fountain flow region and therefore the greater the distance it will have travelled when it reaches the mold wall.

Recently, Coyle et al (1987) reported fountain flow visualization experiments and finite element calculations similar to these of the present work. The tracer element in the experiments of Coyle et al (1987) was a material line spanning the entire mold gapwidth. A simulation of their experiments based on the finite element solution of the present work is shown in Figure 3.28. The tracer line develops initially into a parabolic shape. When it reaches the flow front it is deformed into a mushroom-like shape and subsequently forms the V-shapes near the wall.

The pattern of V-shape formation shown in Figure 3.28 appears different from that shown in Figure 3.25. However, this is only because the initial shape and size of the tracer element is different; in Figure 3.25 the tracer is a small material element near the centerline (corresponding to the color tracers of Schmidt,1974 which had a size of 20% of the mold gapwidth) while in Figure 3.28 the tracer is a material line spanning the entire gapwidth. It is important to note that V-shapes will always appear, for any size of tracer element. Also, the V-shape formation is independent of the nature of fluid and nonisothermal conditions, as shown by Beris (1987) whose arguments are considered below.

The velocity profile in the moving frame of reference and at some cross-section P upstream is shown in Figure 3.29a. Beris's (1987) arguments are based on the mild assumptions of steady-state, centerline symmetry and unidirectional flow conditions at the
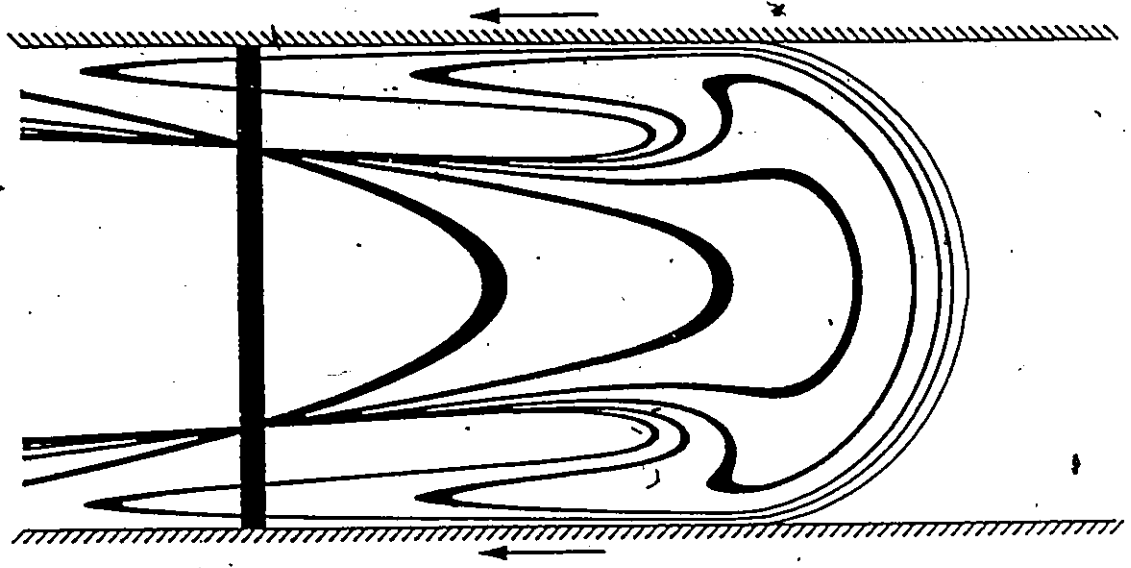
Figure 3.28   Deformation of a material line due to fountain flow. Time interval between successive shapes is 2, in units of H/U

cross-section P. The velocity profile will have the general shape shown in Figure 3.29a, decreasing monotonically from $(U_{max} - U_{avg})$ at the centerline to $-U_{avg}$ at the wall. Therefore there will be a point at the cross-section where the velocity is zero. This is indicated by point B in Figure 3.29a. A material particle that was at point B at $t = 0$ will stay at B for all $t > 0$. Let AB be a material line at time $t = 0$. Due to centerline symmetry point A is constrained to move along the centerline and approach slowly the flow front, since the front tip (flow front/centerline intersection) is a stagnation point. Therefore the endpoints of the material line AB will never move to the left of the original position in Figure 3.29a. However, because of continuity of mass at least one of the intermediate points C has to cross cross-section P to the left, at some distance $y_C > y_B$ and after some finite time $t_0 = V^0/Q^0$, where V^0 is the (constant) volume between the cross-section P and the flow front and Q^0 is the entering flowrate, $Q^0 = \int_0^{y_B} u \, dy$. Let C' be the position of the most advanced (to the left of the cross-section P) material point of line AB at time $t_1 > t_0$, which started at C at $t = 0$. Let also A' be the position at time t_1 of the material particle located at point A at $t = 0$. Then the material line moved from ACB at $t = 0$ to A'C'B at time t_1, forming the characteristic V-shape, with the tip of the V-mark pointing upstream (towards the gate).

The above arguments due to Beris (1987) prove that a material line spanning the whole gapwidth will always deform into a V-shape due to fountain flow. However, this argument can readily be extended to prove that a material element near the centerline of any finite size will also deform into a V-shape. Referring to Figure 3.29b, consider only the part AC of the material line ACB of Figure 3.29a and a material particle which at $t = 0$ is located at some intermediate position D. At time t_1 when the material line AC deforms into A'C' the material particle that was at D moves at D', and $y_{D'} > y_{C'}$, i.e. point D' is closer to the wall. Since D' is closer to the wall than point C' it moves faster in the negative x-direction and at some time $t_2 > t_1$ it is at position D" overtaking C", and forming itself the tip of the V-mark, as
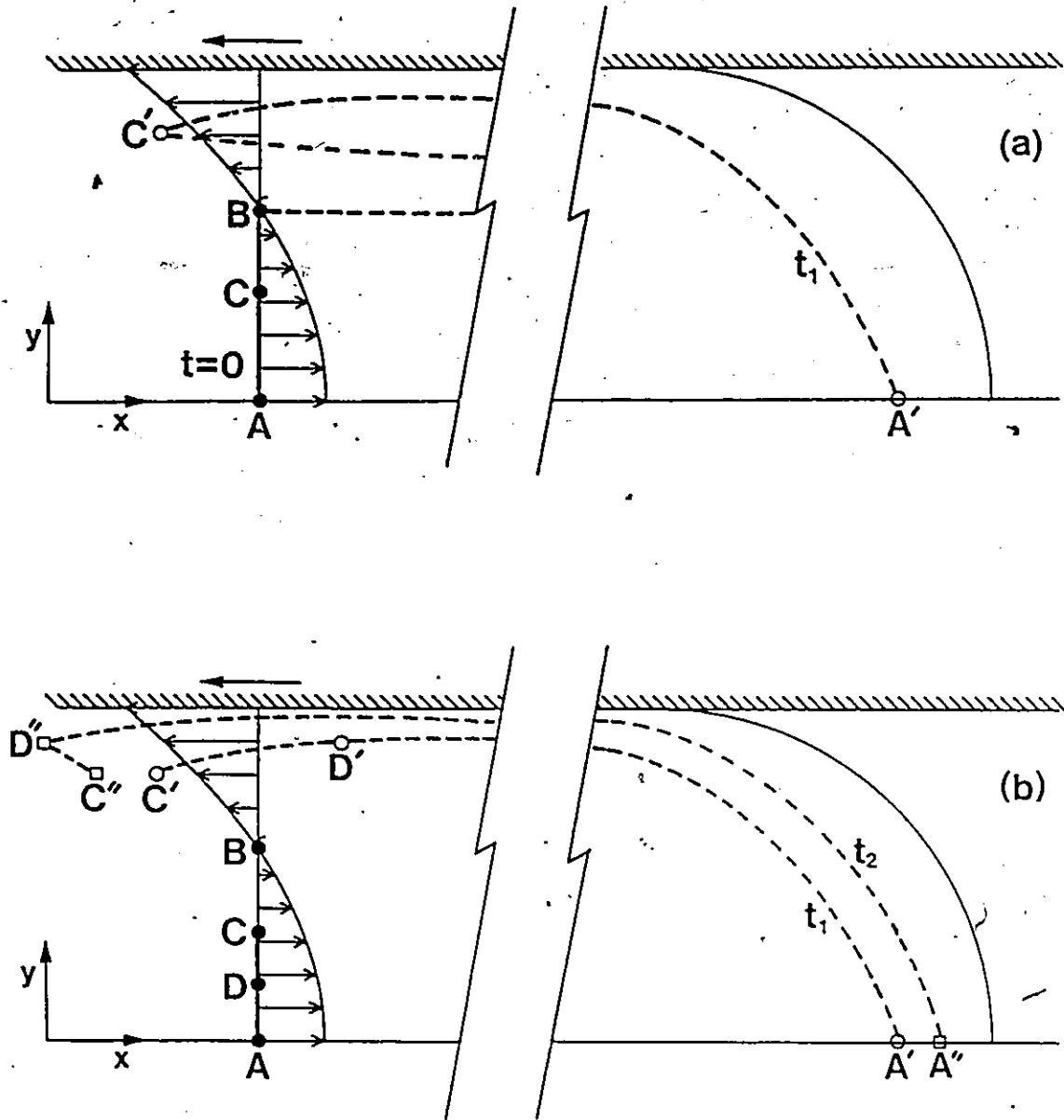
Figure 3.29   Definition sketches for explaining V-Shape formation

shown by A"D"C" in Figure 3.29b. Therefore a material line of size AC will also form a V-shape, only at a greater time. By similar arguments we can show that the material line AD will also form a V-shape, and by induction any material line with finite size close to the centerline will form a V-shape near the wall; the smaller the size of the material line the greater the time required for V-shape formation.

3.4   Fountain and Reverse Fountain Flow

3.4.1   Introduction

As was mentioned in Section 3.1, Rose (1961) in his discussion of the fountain effect was interested in the general case of two viscous fluids displacing each other inside a capillary. In mold filling the displaced fluid is a gas and fountain flow in the advancing fluid is the only phenomenon under consideration. However, in the general case of a viscous receding fluid a reverse fountain flow occurs and interesting flow phenomena take place in the vicinity of the interface. It is the purpose of this section to employ the finite element method and analyze the fountain and reverse fountain flow problem.

The immiscible displacement of two viscous liquids is a stratified multiphase flow problem. This class of problems poses additional complexities over the conventional free surface flows due to a pressure discontinuity and viscous stress jumps at the interface. The discontinuity arises due to the step change of the fluid properties at the interface and is discussed below.

Consider the flow of two immiscible fluids denoted by I and II in Figure 3.30. The two flow fields are governed by the mass and momentum conservation equations in each phase and are coupled through the boundary conditions at the interface. Referring to a local coordinate system (tangential t and normal n to the interface) the interface boundary conditions can be expressed as
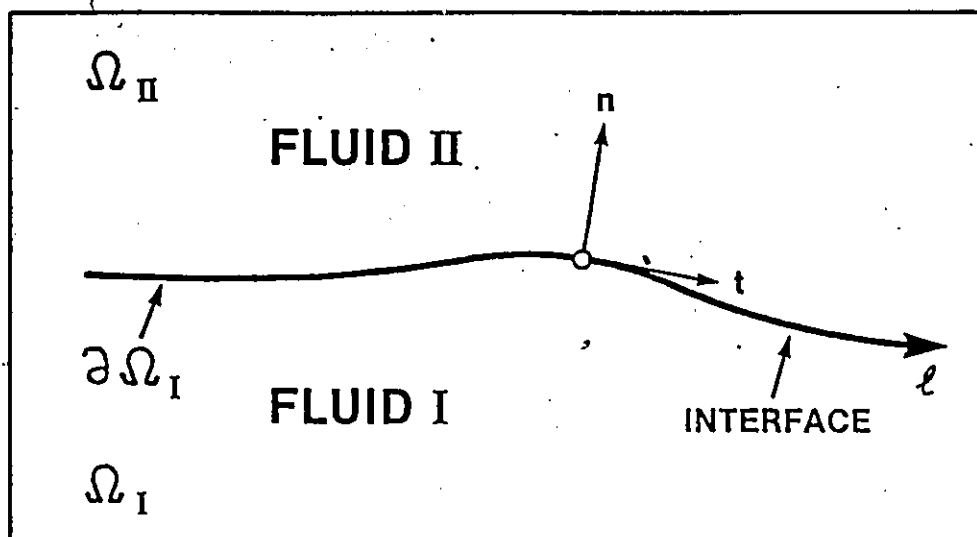
Figure 3.30   Diagram of a fluid-fluid interface

Kinematic condition:

$$V_{t,I} = V_{t,II}, \quad V_{n,I} = V_{n,II} = 0 \tag{3.47}$$

Tangential stress condition:

$$\mu_I \left(\frac{\partial V_{t,I}}{\partial n} + \frac{\partial V_{n,I}}{\partial t} \right) = \mu_{II} \left(\frac{\partial V_{t,II}}{\partial n} + \frac{\partial V_{n,II}}{\partial t} \right) \tag{3.48}$$

Normal stress condition:

$$-P_I + 2\,\mu_I \frac{\partial V_{n,I}}{\partial n} = -P_{II} + 2\,\mu_{II} \frac{\partial V_{n,II}}{\partial n} + \frac{2H}{Ca} \tag{3.49}$$

where $2H$ is the mean surface curvature and P_I, P_{II} are the pressure of fluids I and II at the interface. Eq.(3.48) implies the absence of tangential surface tension gradients, which could be caused by temperature gradients or surfactants.

A pressure discontinuity arises under certain conditions at the interface. For incompressible fluids the continuity equation may be written as:

$$\frac{\partial V_{t,I}}{\partial t} + \frac{\partial V_{n,I}}{\partial n} = 0 \tag{3.50a}$$

$$\frac{\partial V_{t,II}}{\partial t} + \frac{\partial V_{n,II}}{\partial n} = 0 \tag{3.50b}$$

The continuity of velocity at the interface, eq.(3.47) gives:

$$\frac{\partial V_{t,I}}{\partial t} = \frac{\partial V_{t,II}}{\partial t} = \frac{\partial V_t}{\partial t} \tag{3.51}$$

Combining eqs.(3.50a) and (3.50b) and using eq.(3.51)

$$\frac{\partial V_{n,I}}{\partial n} = \frac{\partial V_{n,II}}{\partial n} = \frac{\partial V_n}{\partial n} = -\frac{\partial V_t}{\partial t} \tag{3.52}$$

Then, using eq.(3.52) the normal stress condition, eq.(3.49) can be written as:

$$(P_{II} - P_I) = 2\,(\mu_I - \mu_{II})\,\frac{\partial V_t}{\partial t} + \frac{2H}{Ca} \tag{3.53}$$

By inspection of eq.(3.53) we conclude that there will be a pressure discontinuity:

1. Whenever there are non-negligible surface tension effects

$$(2H/Ca \neq 0)$$

2. In the absence of surface tension effects ($2H/Ca = 0$) but with viscosities of the two fluids being different ($\mu_I - \mu_{II} \neq 0$). In this case the pressure discontinuity will be proportional to the tangential velocity gradient ($\partial V_t/\partial t$).

The pressure discontinuity invalidates the continuous approximation of the finite element method of Section 3.2.2 and requires a special treatment. This is accomplished with the double-node finite element technique of the next section. The technique allows the finite element grid itself to be discontinuous at the interface by having two values for the primitive variables (velocities and pressure) on two different nodal points at the same spatial location. Primitive variables that are continuous are specified as such, interface conditions are applied directly and the finite jump in the discontinuous variables is determined from the solution of the global system.

This double-node finite element method has long been used as a standard technique to handle discontinuities in other areas of computational mechanics; in fracture mechanics for crack problems (Mirza & Olson, 1978; Liaw et al, 1984), and especially in aerodynamics for inviscid flow over airfoils (Baskharone & Hamed, 1981; Cox et al, 1982). It has also been applied to incompressible viscous flow, namely two-layer curtain coating, by Kistler (1984). Recently, Dheur & Crochet (1988) proposed a different method to handle the pressure discontinuity by employing a C^{-1} pressure approximation (i.e., discontinuous pressure at interelement boundaries).

3.4.2   Double-Node Finite Element Technique

In this technique the finite element grid is constructed with double nodes at the interface as shown in Figure 3.31. This figure also shows a fictitious pressure distribution (vertical axis) and how the interface double nodes are used to capture this discontinuity.

**DOUBLE NODES
AT THE INTERFACE**
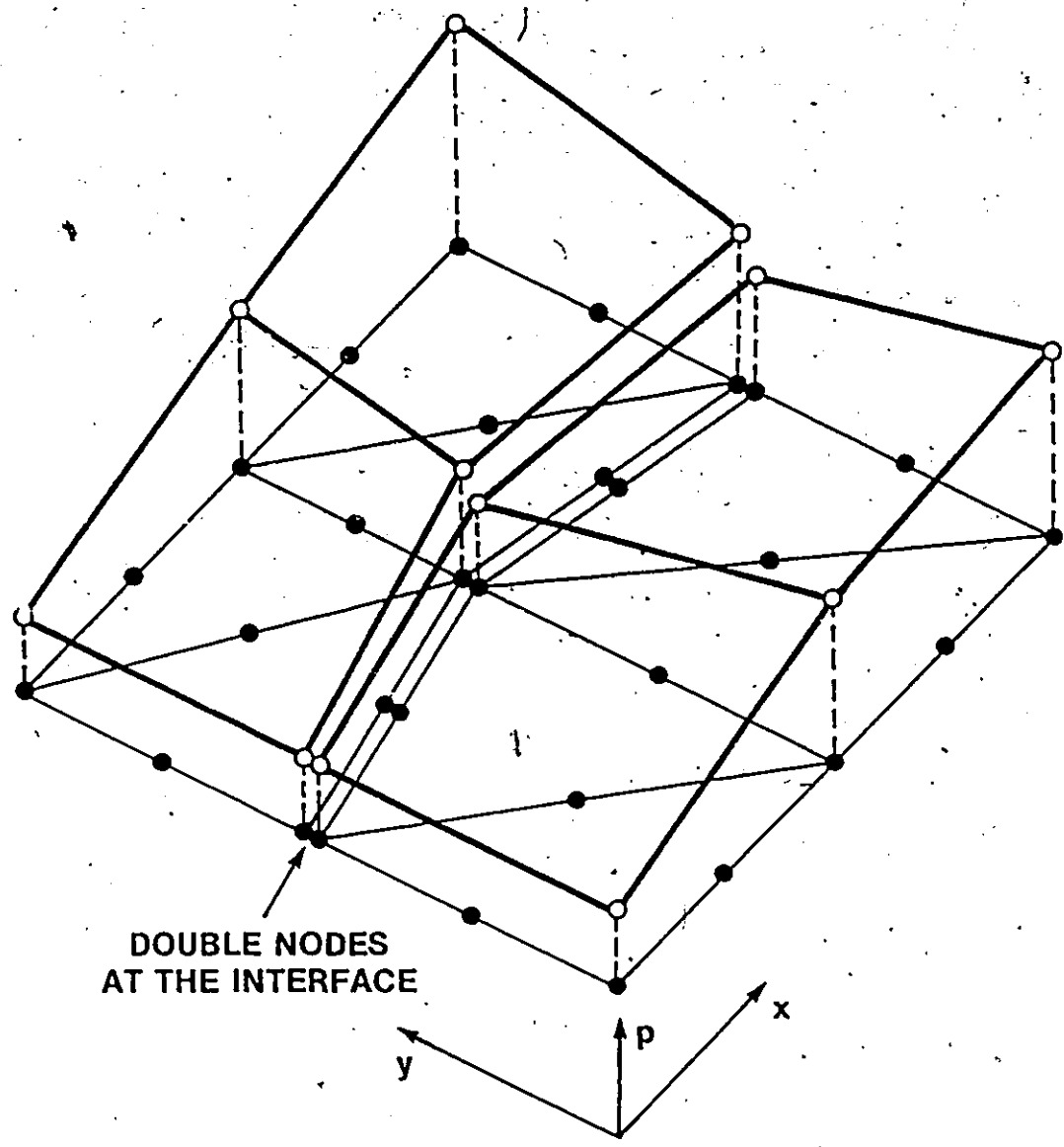
Figure 3.31   Diagram of a discontinuous grid with double nodes along the interface
illustrating the pressure discontinuity (vertical axis)

Consider again the interface of Figure 3.30 separating the two immiscible fluids I and II and a pair of double nodes at the same spatial location at the interface. The finite element equations of Section 3.2.2, eqs.(3.6-3.7), apply in the two flow domains Ω_I and Ω_{II}, while the interface boundary conditions in full vector-form are:

$$\text{Kinematic: } V_I = V_{II} = V, \quad n \cdot V = 0 \tag{3.54}$$

$$\text{Dynamic: } n_I \cdot \sigma_I + n_{II} \cdot \sigma_{II} = \frac{2H}{Ca} n_I \tag{3.55}$$

where n_I and n_{II} are the outward unit vectors normal to the interface and $n_I = -n_{II}$.

The momentum residuals at the double nodes will be:

$$R_{m,I}^i = \int_{\Omega_I} \left\{ \phi^i \, Re_I \, V_I \cdot \nabla V_I + \nabla \phi^i \cdot \sigma_I - \phi^i S_I^{-1} g \right\} d\Omega - \int_{F.S.} n_I \cdot \sigma_I \phi^i \, d\ell = 0 \tag{3.56a}$$

$$R_{m,II}^i = \int_{\Omega_{II}} \left\{ \phi^i \, Re_{II} \, V_{II} \cdot \nabla V_{II} + \nabla \phi^i \cdot \sigma_{II} - \phi^i S_{II}^{-1} g \right\} d\Omega - \int_{F.S.} n_{II} \cdot \sigma_{II} \phi^i \, d\ell = 0 \tag{3.56b}$$

Combination of the momentum residuals, eqs.(3.56), at the double nodes and use of the dynamic condition, eq.(3.55), gives:

$$R_m^i = R_{m,I}^i + R_{m,II}^i = \int_{\Omega_I} \left\{ \phi^i \, Re_I \, V_I \cdot \nabla V_I + \nabla \phi^i \cdot \sigma_I - \phi^i S_I^{-1} g \right\}$$

$$+ \int_{\Omega_{II}} \left\{ \phi^i \, Re_{II} \, V_{II} \cdot \nabla V_{II} + \nabla \phi^i \cdot \sigma_{II} - \phi^i S_{II}^{-1} g \right\} \tag{3.57}$$

$$- \int_{F.S.} \frac{2H}{Ca} n_I \phi^i \, d\ell = 0$$

The pressure involved in the total stress tensor σ is discontinuous at the interface. Since the pressure is a Lagrange multiplier introduced to satisfy the incompressibility constraint, the continuity residuals must be weighted separately with the pressure basis functions on either side of the interface, i.e.,:

$$R^i_{c,I} = \int_{\Omega_I} \nabla \cdot V_I \, n^i \, d\Omega = 0 \qquad (3.58)$$

$$R^i_{c,II} = \int_{\Omega_{II}} \nabla \cdot V_{II} \, n^i \, d\Omega = 0 \qquad (3.59)$$

The two scalar equations resulting from the vector momentum equation, eq.(3.57), and eqs.(3.58) and (3.59) provide four equations corresponding to the four variables at the interface double nodes (two velocity components and two pressure variables). Although separate nodal variables (velocities and pressure) are defined at both the double nodes, the imposition of the kinematic condition for continuity of the velocity field at the interface eliminates the second velocity degree of freedom (i.e., only the pressure is double-valued at the interface nodes). With this technique the system is closed, interface boundary conditions are used to match the two flow fields, and the pressure discontinuity is determined from the solution of the global system.

3.4.3   Immiscible Displacement in a Capillary Tube

When two immiscible fluids displace each other inside a capillary a toroidal-like flow occurs adjacent to the moving interface. The resulting flow field is schematically shown in Figure 3.32, where a viscous fluid (lower fluid) advances upward, displacing a less viscous fluid at constant speed. The frame of reference is at rest with respect to the moving interface so that the walls appear to move downward with the velocity of the advancing interface. The advancing fluid undergoes fountain flow, the receding fluid undergoes reverse fountain flow, and a bolus forms inside the less viscous fluid so as to meet the requirements of mass continuity and compatibility between the two flow fields. The existence of the bolus was first observed and documented experimentally by Dussan (1977), who injected dye on the interface
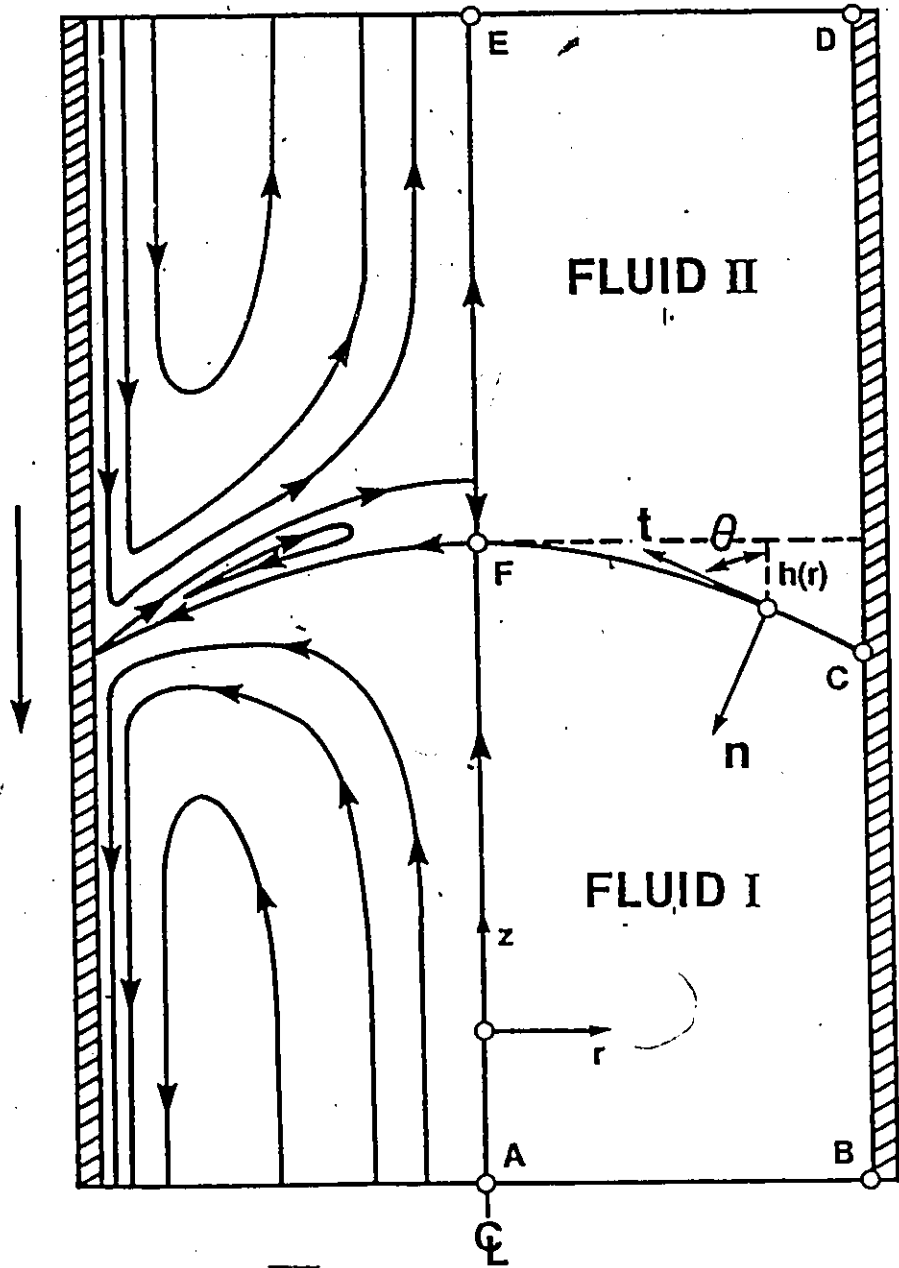
Figure 3.32   Definition sketch for immiscible liquid displacement in a tube

and noticed that a portion of it was trapped and recirculating next to the interface inside the less viscous fluid.

This phenomenon is of interest for oil recovery by immiscible displacement through porous media. It is common practice to introduce surfactants in order to reduce the surface tension and enhance oil recovery. Therefore, it is important whether the surfactants remain on the interface or are pushed off and forced away from it (Dussan, 1977).

A review of the relevant literature can be found in Kafka & Dussan (1979), with an analytical solution for the limiting case of a flat interface, and a detailed discussion of the phenomena near the contact line. Also, Huh & Scriven (1971) solved the problem of a flat interface moving over a solid plane and obtained analytically the characteristic streamline pattern in the vicinity of the contact line.

The immiscible liquid displacement problem was simulated numerically with the double-node finite element method of the previous section. The wetting fluid was the less viscous fluid (fluid II) and the viscosity ratio μ_{II}/μ_I was 0.1. The capillary number Ca was varied in the range 0.001-0.1. For Ca $>$ 0 the contact angle θ_c needs to be specified. This angle was fixed to 80°.

Consider a typical case, for Ca=0.01. The finite element grid used is shown in Figure 3.33. The computed flow field is shown in Figure 3.34, where the more viscous fluid is on the lower part and advances upward. The velocity vectors are plotted on the right half and the streamlines on the symmetric left half. This figure clearly shows the fountain flow in the advancing fluid, reverse fountain flow in the receding fluid, and the characteristic vortex next to the interface inside the less viscous fluid, fully in agreement with the work of Dussan (1977) and Kafka & Dussan (1979).
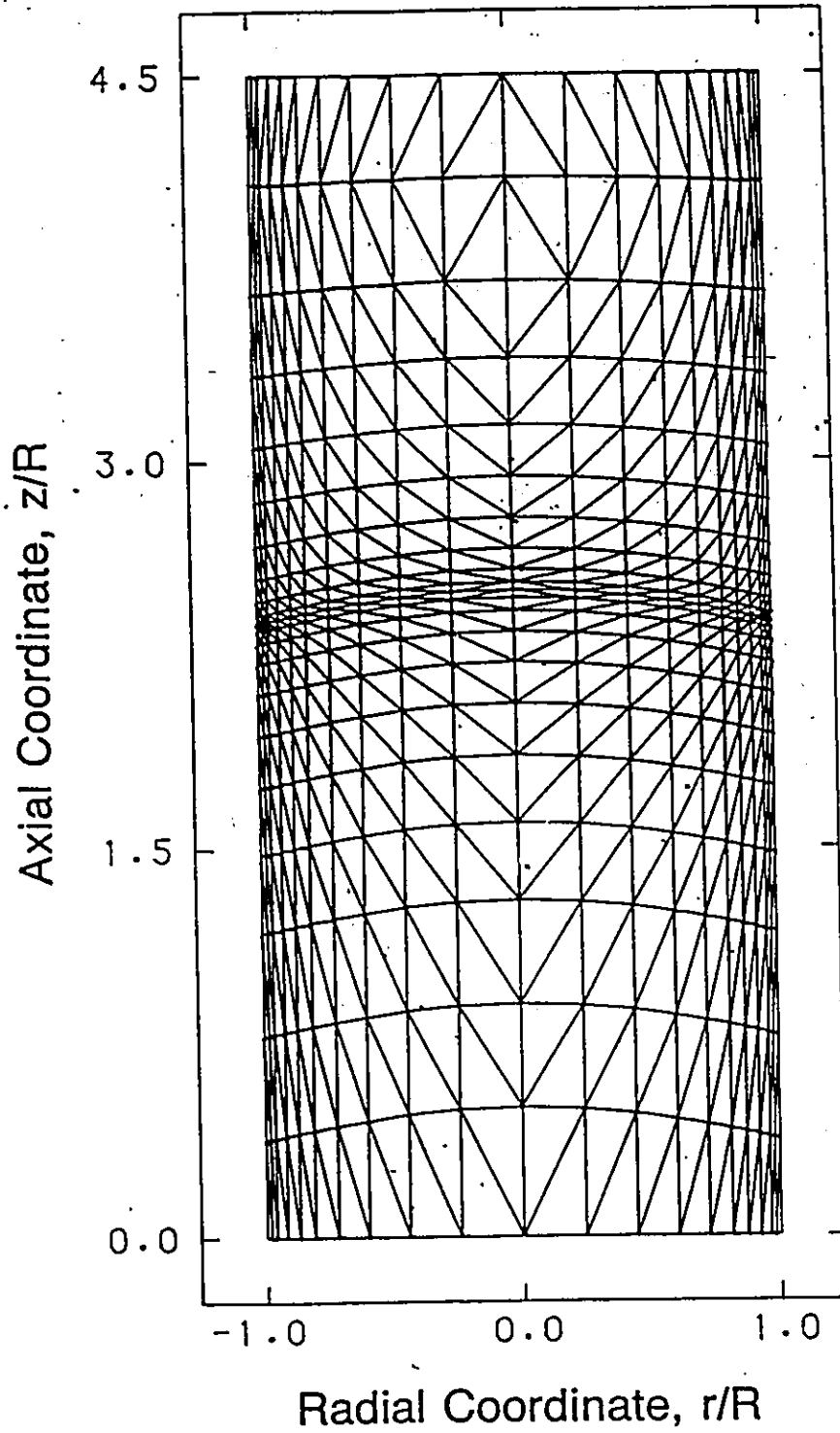
Figure 3.33   Finite element grid
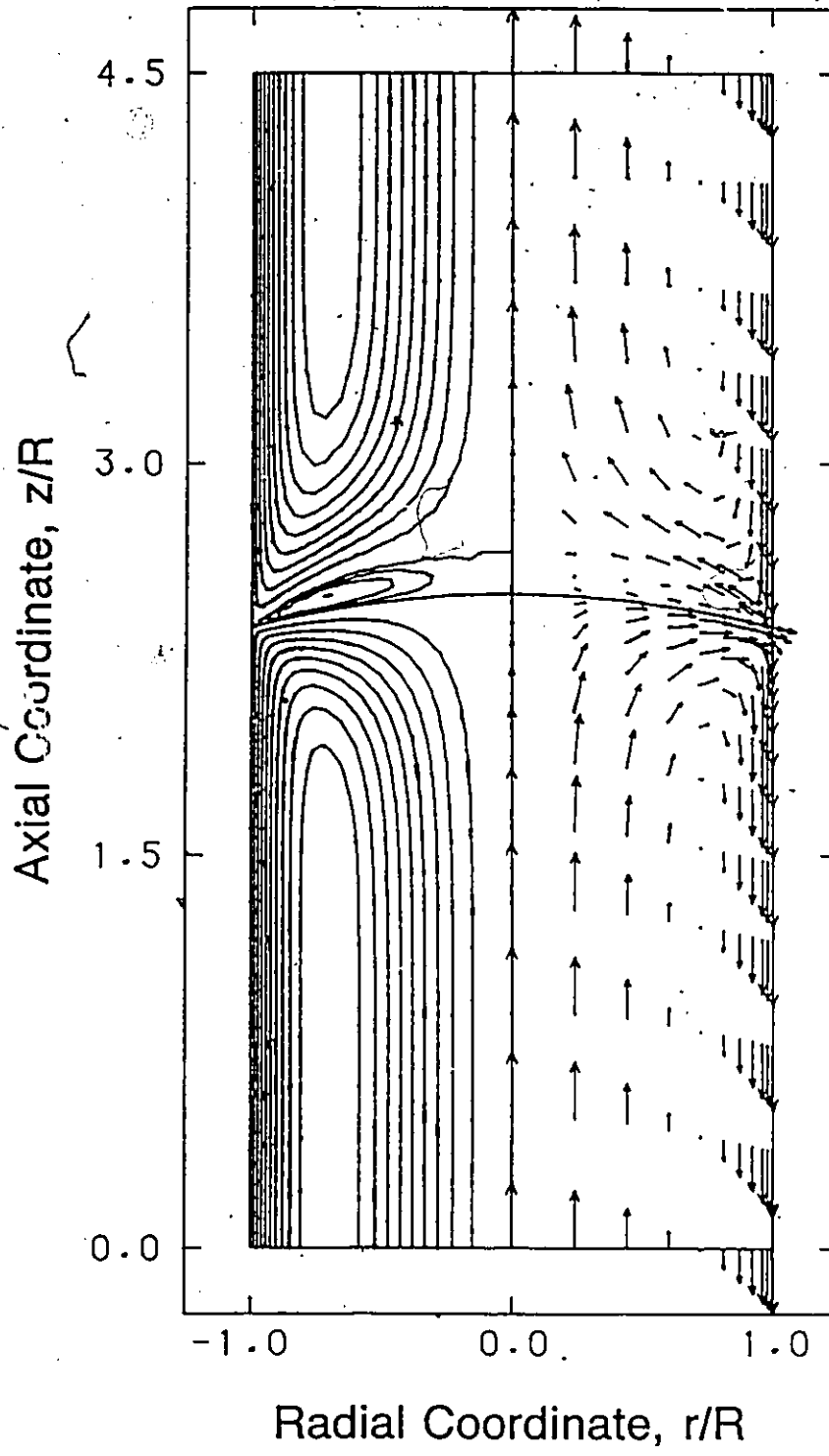
Figure 3.34   Velocity vectors and streamlines for the immiscible liquid displacement problem
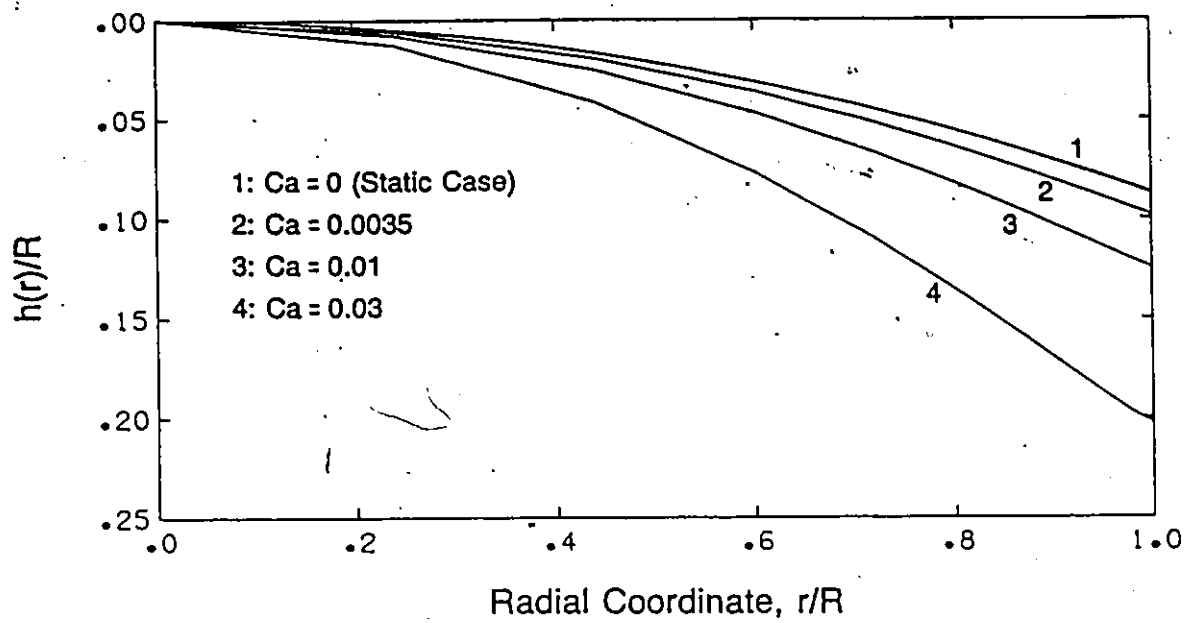
Figure 3.35   Interface dependence on the Capillary number
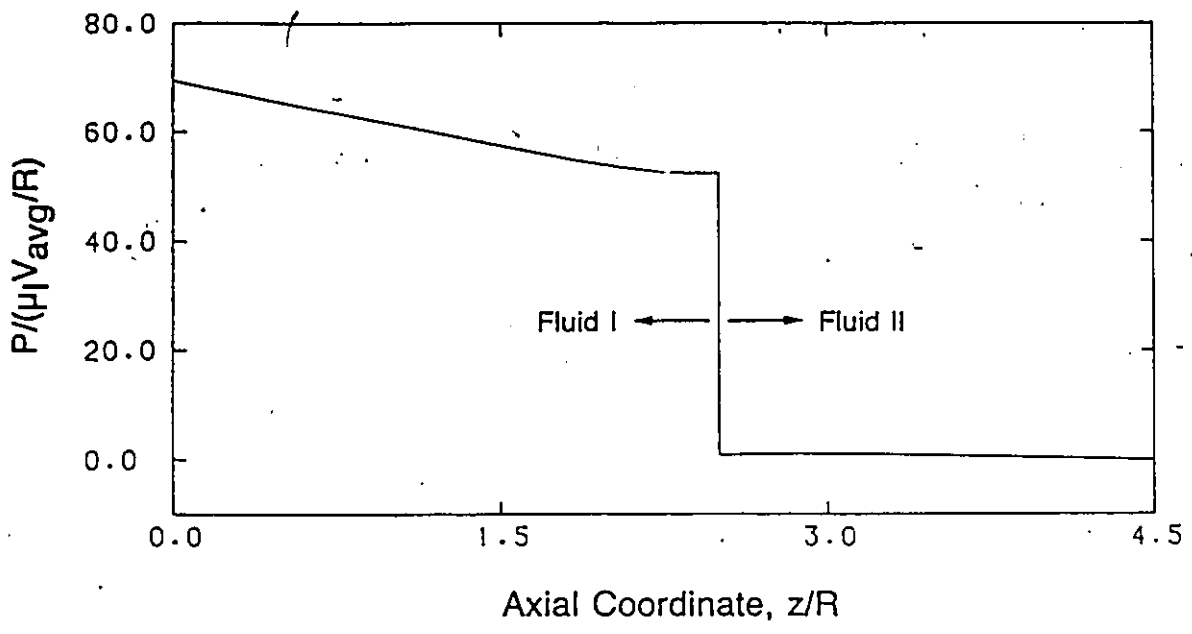
Figure 3.36   Pressure variation along the centerline

The effect of the capillary number Ca on the interface shape is shown in Figure 3.35. As Ca is increased, that is, as the effect of the viscous terms is increased, the interface deviates more from the limiting static case, becoming more convex.

A stagnation point appears at the intersection of the interface with the centerline. As a result of the vortex formation a second stagnation point appears on the centerline, inside the less viscous fluid. The normalized distance Z_{st} between the two stagnation points is a measure of the size of the vortex, while the relative rate of fluid recirculating in the vortex ψ_v is a measure of its intensity. The dependence of Z_{st} and ψ_v on Ca is given in Table 3.4. It is shown that the vortex becomes smaller in size and weaker in intensity as Ca is increased.

The discontinuity of the pressure at the interface that necessitated the use of a special finite element technique is shown in Figure 3.36, which is a plot of the pressure along the centerline. The pressure undergoes a large step change at the interface due to surface tension effects. Having two pressure variables at the interface double nodes enabled the finite element technique to resolve this discontinuity.

Table 3.4 Results for the immiscible liquid displacement problem

Ca	h(r/R = 1)/R	z_{st}/R	ψ_v
0.001	0.0884	0.1767	0.0614
0.0035	0.0987	0.1711	0.0596
0.01	0.1250	0.1573	0.0546
0.03	0.2028	0.1162	0.0436
0.06	0.3177	0.0697	0.0296
0.1	0.5040	0.0169	0.0129

The double-node finite element method of this section made possible the simulation of the general fountain and reverse fountain flow problem. The method can be readily applied

to study other stratified multiphase flows. Some applications to coextrusion were reported in Mavridis et al (1987).

3.5   Concluding Remarks

The fluid mechanics behind an advancing flow front was examined in the steady-state. A comprehensive finite element algorithm was described (Section 3.2.2) that allows simulation of free surface flows. The technique determines simultaneously the flow field and the free surface shape and employs a Newton-Raphson iterative scheme, whose superior convergence properties reduce the computational cost considerably.

Detailed fountain flow calculations with a Newtonian fluid in planar and axisymmetric geometries were described in Section 3.2.3. The effect of a slip boundary condition was also investigated (Section 3.2.3.2). Simulations with shear-thinning fluids showed the same qualitative features of fountain flow as for Newtonian fluids (Section 3.2.4).

The effect of fountain flow kinematics on the deformation experienced by the fluid was examined in Section 3.3. It was shown that fluid elements from the centerline are found at the walls, extended in the flow direction and forming characteristic V-shapes, fully in agreement with the experimental photographs of Schmidt (1974).

Finally, the general fountain and reverse fountain flow problem was addressed in Section 3.4. A double-node finite element technique suitable for stratified multiphase flows was described and it was applied to simulate the immiscible displacement in a capillary tube. The computational results clearly show the existence of a recirculating vortex adjacent to the interface and inside the less viscous fluid, in full agreement with Dussan's (1977) experimental observations.

CHAPTER 4

TRANSIENT FREE-SURFACE FLOWS

IN INJECTION MOLD FILLING

This chapter contains the numerical studies on the transient free surface flows involved in the injection mold filling process. A numerical technique for the simulation of this class of problems is presented. The technique combines a Galerkin/Finite Element discretization of the governing equations with a predictor-corrector scheme for integration in time, and is capable of handling deforming flow domains with moving contact lines. The method is applied on the start-up flow of a fluid with a free front (transient fountain flow) and the collision of two fronts to form a weldline.

4.1   Introduction

The finite element approach adopted in Chapter 3 enabled the detailed investigation of the fountain effect in the steady state. A question that remained unanswered is how the associated flow phenomena change under truly transient conditions. In order to study the time dependent motion of the advancing front.the finite element methodology of the previous chapter must be extended appropriately for transient free surface flows.

Transient free surface flows encountered in injection mold filling include advancing and colliding flow fronts and involve the complicating feature of the moving contact line (fluid/gas/wall intersection); depending on local conditions (to be discussed in Section 4.2.1) the contact line may remain pinned to the wall or it may roll over the solid surface. In the present work conditions for the contact line motion are derived and

implemented in a very efficient finite element algorithm that can handle transient flows with deforming flow domains. The numerical technique is employed to simulate the start-up flow of a fluid with a free front and the collision of two flow fronts to form a weldline.

4.2 Numerical Simulation of Transient Free-Surface Flows

4.2.1 Mathematical Modeling

We consider the time-dependent, isothermal flow of a incompressible fluid. The governing equations include the mass and momentum conservation equations:

$$\nabla \cdot V = 0 \tag{4.1}$$

$$Re \frac{DV}{Dt} = \nabla \cdot \sigma + S^{-1}g \tag{4.2}$$

where all symbols have their usual meaning (Section 3.2.1) and D/Dt denotes the material (or substantial) time derivative.

Appropriate boundary conditions require the specification of two scalar boundary conditions on every portion of the flow boundary. A velocity field satisfying eq.(4.1) and the initial shape of the free surface must also be specified as initial conditions.

In fully developed flow regions, symmetry lines and the wall, the boundary conditions are: fully developed velocity profile, symmetry conditions and no-slip respectively. At the free surface a force balance provides the following boundary condition:

$$n \cdot \sigma = -P_a n + \frac{1}{Ca}\left(\frac{1}{R_1} + \frac{1}{R_2}\right)n \tag{4.3a}$$

where n is the outward unit vector normal to the free surface, R_1 and R_2 are the principal radii of curvature and P_a is the ambient pressure (set to zero as the pressure datum). Ca is the Capillary number defined as the ratio of viscous to surface tension forces, $Ca = \mu U/\gamma$. In injection molding of molten polymers the Capillary number is large and eq.(4.3a) reduces to the no-traction condition:

$$n \cdot \sigma = 0. \tag{4.3b}$$

Another condition arises at the free surface from mass conservation considerations: a free surface is a material surface and no fluid particle crosses it. For a point x at the free surface this condition is expressed as:

$$n \cdot V = n \cdot \left(\frac{\partial x}{\partial t}\right)_{F.S.} \tag{4.4}$$

The contact line, where the free surface intersects a solid wall, poses a special problem and is discussed below.

Contact Line Motion   Complications arise at the contact line: when the no-slip condition is applied at the wall up to the contact line, a stress singularity results (stresses increase without bound as the contact line is approached). Singular stresses, although aphysical, can be tolerated as they long as they are integrable, i.e., the total drag exerted on the wall remains finite. When the contact line does not move (static contact line) the singularity is integrable (Michael, 1958). For a moving contact line the singularity is not-integrable when the contact angle is less than 180° (Huh & Scriven, 1971 ; Dussan, 1979). Pismen & Nir (1982) who obtained a perturbation solution in the vicinity of the contact line, for the case of a liquid advancing into a inviscid medium, reported an integrable singularity for a 180° contact angle. In this work only viscous effects are taken into account and the contact angle is required to be 180° ; therefore the singularity is integrable and there is no need to remedy the situation, for example with a slip-boundary condition.

There remains a difficulty in treating the apparent motion of the contact line. Consider the start-up flow problem, where the initial free surface is perpendicular to the wall (ABCD at time t_0 in Figure 4.1). As the flow begins the free surface deforms and the contact angle increases (time t_1). In the numerical algorithm (to be described in the next section) the position of the contact line is fixed up to the time that the contact angle becomes 180°. At this
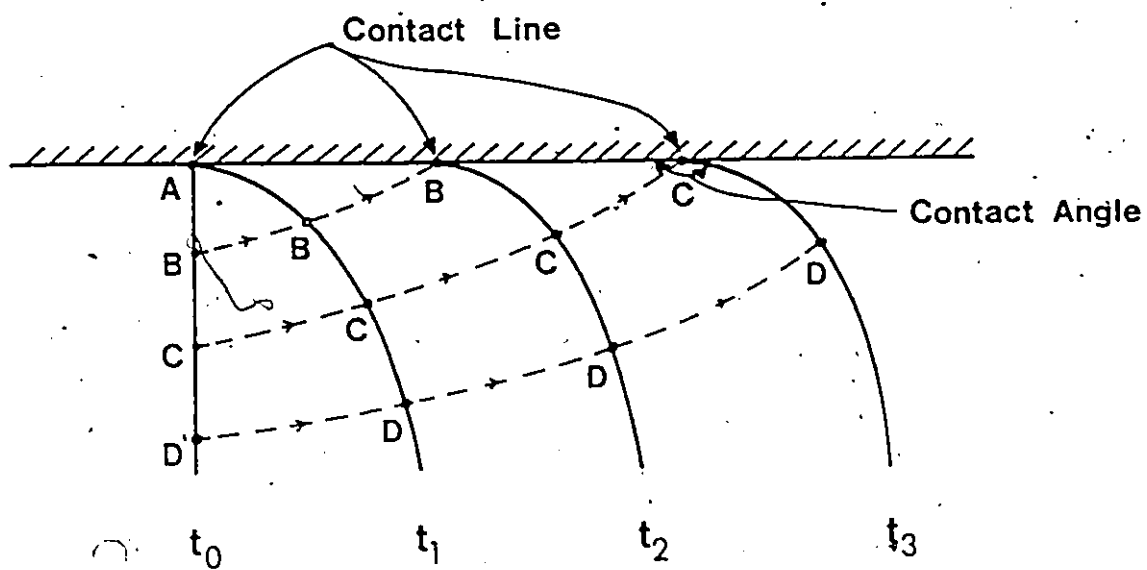
Figure 4.1   Contact line motion over a solid surface

time the condition of a fixed contact line position is replaced by a 180° contact angle condition and the contact line is allowed to move. The mechanism implied by these conditions is that of a rolling-type motion of the fluid over the solid surface. It should be noted that the contact line motion is apparent, i.e., there is no slip. A different material particle occupies the contact line position at every instant, and the contact line appears to move as new material reaches the wall from the free surface as indicated in Figure 4.1.

The above requirements for the contact-line motion provide the necessary condition for the determination of the contact line position. Other workers (Behrens, 1983 and Behrens et al, 1987 for transient flows and Viriyayuthakorn & Deboo, 1983 for steady flows) do not impose explicitly a condition at the contact line but determine its position implicitly ; the kinematic condition, eq.(4.4), is imposed at the free surface and the contact line position is determined as the intersection of the extrapolated free surface with the wall. This implicit scheme is equivalent to that used in the present work, i.e., combination of the kinematic condition with no-slip at the contact line directly yields the present scheme, as it will be shown below.

Consider for example, a fluid displacing a gas over a flat solid surface, parallel to the x-direction as shown in Figure 4.2. If we parametrize the free surface as $y = h(x)$, the outward unit vector normal to the surface is:

$$n = \left[1 + \left(\frac{\partial h}{\partial x}\right)^2\right]^{-1/2}\left[-e_x\left(\frac{\partial h}{\partial x}\right) + e_y\right] \tag{4.5}$$

and the kinematic condition, eq.(4.4), can be written as:

$$-\left(\frac{\partial h}{\partial x}\right)u + v = -\left(\frac{\partial h}{\partial x}\right)\frac{\partial x}{\partial t} + \frac{\partial h}{\partial t} \tag{4.6a}$$

At the contact line $u = v = 0$ (no slip) and $\partial h/\partial t = 0$ (straight wall). Then eq.(4.6a) becomes:

$$\left(\frac{\partial h_{CL}}{\partial x}\right)\left(\frac{\partial x_{CL}}{\partial t}\right) = 0 \tag{4.6b}$$

From eq.(4.6b) we notice that:
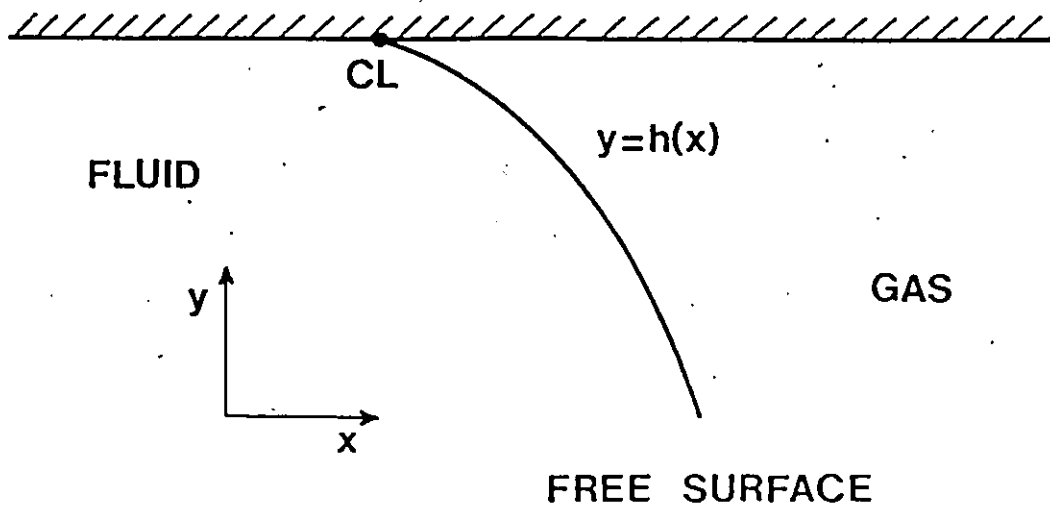
Figure 4.2   Schematic of a solid/fluid/gas contact line

(i)   when the contact angle is less than $180°$ ($\partial h_{CL}/\partial x \neq 0$) then the contact line does not

move ($\partial x_{CL}/\partial t = 0$).

(ii)   for the contact line to move ($\partial x_{CL}/\partial t \neq 0$) the contact angle must be $180°$

($\partial h_{CL}/\partial x = 0$).

The above conditions result from purely kinematic considerations at the contact

line combined with the no-slip hypothesis. They are appropriate when surface tension effects

are insignificant, which is the case for the problems examined in this work.

4.2.2 Finite Element Formulation

The Galerkin/Finite Element formulation of the time-dependent equations

proceeds in exactly the same way as for steady flows in Section 3.2.2 (u-v-p-h-δ formulation).

The weighted residual equations are:

$$R_m^i = \int_\Omega \left\{ \phi^i \, Re \frac{DV}{Dt} + \nabla\phi^i \cdot \sigma - \phi^i S^{-1} g \right\} d\Omega - \int_{\partial\Omega} n \cdot \sigma \, \phi^i d\ell = 0 \qquad (4.7)$$

$$R_c^i = \int_\Omega \nabla \cdot V \, n^i d\Omega = 0 \qquad (4.8)$$

$$R_k^i = \int_{F.S.} \left\{ n \cdot V - n \cdot \frac{\partial x}{\partial t} \right\} \phi^i(\xi,\eta=1) d\ell = 0 \qquad (4.9)$$

$$R_\delta^i = \int_{-1}^{0} \left(x_\xi^2 + y_\xi^2 \right)^{1/2} \Big|_{\eta=1} d\xi - \int_0^1 \left(x_\xi^2 + y_\xi^2 \right)^{1/2} \Big|_{\eta=1} d\xi = 0 \qquad (4.10)$$

The material derivative D/Dt in eq.(3.7) is written as:

$$\frac{DV}{Dt} = \frac{\partial V}{\partial t} + \left(V - \frac{\partial x}{\partial t} \right) \cdot \nabla V \qquad (4.11)$$

to account for the nodal motion ($\partial x/\partial t$) in the deforming finite element grid (Lynch, 1982 ;

Khesghi & Scriven, 1984 ; Keunings, 1986a).

The time derivative of the nodal position vector ($\partial x/\partial t$) is expressed in terms of time derivatives of free surface parameters:

$$\frac{\partial x}{\partial t} = \frac{\partial x}{\partial h}\frac{\partial h}{\partial t} + \frac{\partial x}{\partial \delta}\frac{\partial \delta}{\partial t} \tag{4.12}$$

Eqs. (4.7-4.10) lead to a coupled system of algebraic and first-order ordinary differential equations of the form:

$$R(V, P, h, \delta, \dot{V}, \dot{h}, \dot{\delta}) = 0 \tag{4.13}$$

where the dot denotes differentiation with respect to time. The time derivatives are approximated with finite differences as explained in the next section.

The conditions for the contact line motion are implemented as follows. The contact angle θ is computed from:

$$\theta = \cos^{-1}(n_{CL} \cdot n_w) \tag{4.14}$$

where n_W is the unit vector normal to the wall ($n_w = -e_y$ in the present case) and n_{CL} is unit vector normal to the free surface at the corner of the element adjacent to the contact line:

$$n_{CL} = \frac{-y_\xi e_x + x_\xi e_y}{\left(x_\xi^2 + y_\xi^2\right)^{1/2}}\bigg|_{\xi=-1, \eta=1} \tag{4.15}$$

When $\theta < 180°$ the h^i variable corresponding to the contact line position is fixed with an essential boundary condition. When θ becomes $180°$ the contact line is allowed to move and the corresponding h^i is determined on the requirement of a $180°$ contact angle condition, which is imposed by adding the equation

$$n_{CL} \cdot n_w = \cos(180°) \tag{4.16}$$

in the algebraic system to be solved.

4.2.3 Predictor-Corrector Scheme for integration in time

The Galerkin/Finite Element formulation reduced the original set of partial differential equations into a coupled set of algebraic equations and first-order ordinary

differential equations with respect to time (i.e., only the spatial derivatives were discretized).
To integrate the equations in time we employ a predictor-corrector scheme, originally
introduced by Gresho et al (1979) and further developed by Khesghi & Scriven (1984). The
integration technique is second-order-accurate and consists of an explicit Adams-Bashforth
formula (predictor) and the implicit trapezoid rule (corrector), combined to yield a stable
integration scheme in which the time step-size is varied automatically, based solely on
temporal accuracy requirements, by obtaining a good estimate of the local (single step) time
truncation error.

To illustrate the method consider the system:

$$f(t, y, \dot{y}) = 0 \qquad (4.17)$$

$$y (t = 0) = y_o \qquad (4.18)$$

and let y^{j-1} be the solution at time t^{j-1}. The solution at time $t^j = t^{j-1} + \Delta t^{j-1}$ is obtained through
the following procedure:

(i)   **Predictor**

The variable-step, second-order Adams-Bashforth (AB) formula gives:

$$y_p^j = y^{j-1} + \frac{\Delta t^{j-1}}{2}\left[\left(2 + \frac{\Delta t^{j-1}}{\Delta t^{j-2}}\right)\dot{y}^{j-1} - \frac{\Delta t^{j-1}}{\Delta t^{j-2}}\dot{y}^{j-2}\right] \qquad (4.19)$$

Note that two history vectors of time derivatives are required ($\dot{y}^{j-1}$ and $\dot{y}^{j-2}$ at time t^{j-1} and t^{j-2}
respectively). These are obtained simply and recursively from the corrector step described
below. Also, note that the AB formula can only be applied from the third step onward.

(ii)   **Corrector**   —

The trapezoid rule (TR) formula is:

$$y_c^j = y^{j-1} + \frac{\Delta t^{j-1}}{2}\left(\dot{y}^{j-1} + \dot{y}^j\right) \qquad (4.20a)$$

Solving for $\dot{y}^j$:

$$\dot{y}^j = 2\frac{y_c^j - y^{j-1}}{\Delta t^{j-1}} - \dot{y}^{j-1}$$ (4.20b)

Eq.(4.20b) is substituted in eq.(4.17) to yield:

$$f\left(t^j, y_c^j, 2\frac{y_c^j - y^{j-1}}{\Delta t^{j-1}} - \dot{y}^{j-1}\right) = 0$$ (4.21)

Eq.(4.21) is a system of algebraic equations for y_c^j. This system is solved with Newton-Raphson iteration, with the initial guess provided by the predictor y_p^j.

(iii)   Local truncation error control and time step-size selection

An estimate of the local time truncation error can be obtained with a Taylor series expansion of both the Adams-Bashforth and trapezoid rule formulas, eqs.(4.19) and (4.20a). The result is (Gresho et al, 1979):

$$\Delta(y^i) \equiv y_{exact}^j - y_c^j = \frac{y_c^j - y_p^j}{3\left(1 + \dfrac{\Delta t^{j-2}}{\Delta t^{j-1}}\right)} + 0\left[\left(\Delta t^{j-1}\right)^4\right]$$ (4.22)

An appropriate tactic (Khesghi & Scriven, 1984) is to keep approximately constant the ratio of the norm of the error, eq.(4.22), to the like norm of the time derivatives, i.e.,:

$$\| \Delta(y^j)\| \leq \chi \varepsilon \| \dot{y}^j\|$$ (4.23)

where ε is the tolerance (usually set to 10^{-3} or less) and χ is the ratio of the maximum allowed relative time discretization error to the preferred value ε, usually set to 1.5 (Khesghi & Scriven, 1984).

At the completion of the j-th step with step-size Δt^{j-1}, the truncation error is estimated from eq.(4.22). If it violates the error criterion, eq.(4.23), then the step-size is deemed unacceptably large. The step-size Δt^{j-1} is reduced (usually by a factor 0.8) and the cycle is repeated (from the predictor, step (i)).
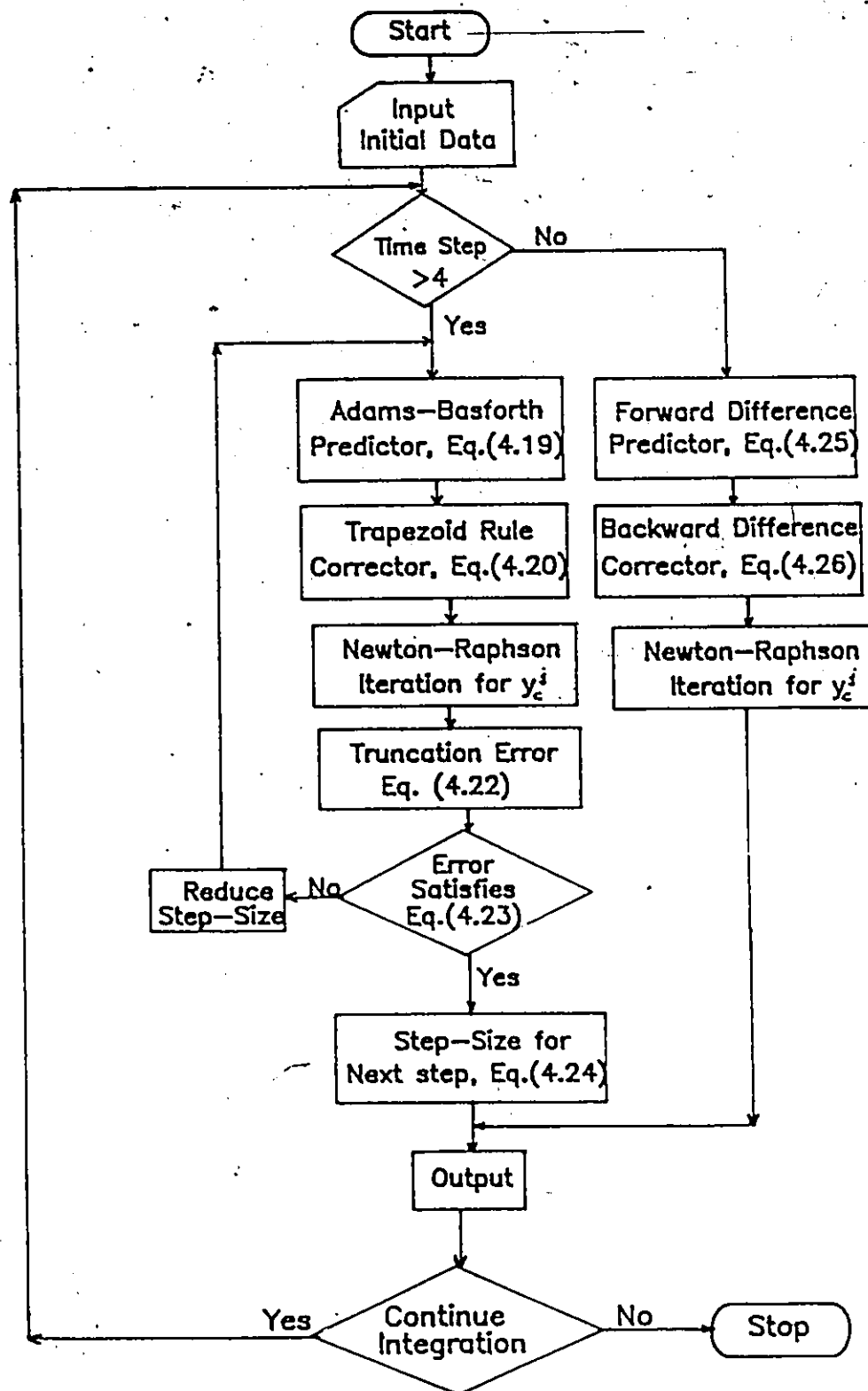
Figure 4.3   Flowchart of predictor-corrector scheme

If the criterion of eq.(4.23) is satisfied the solution at t^j with Δt^{j-1} is accepted $(y^j = y_c^j)$ and a new step-size Δt^j for the next step $(j+1)$ is computed from (Gresho et al, 1979 ; Khesghi & Scriven, 1984):

$$\Delta t^j = \min\left\{2\Delta t^{j-1}, \Delta t^{j-1}\left[\varepsilon\frac{\|\ddot{y}^j\|}{\|\Delta(y^j)\|}\right]^{1/3}\right\} \qquad (4.24)$$

The above scheme can only be applied from the third step onward, since it requires two history vectors. The first steps at the outset of the integration are performed with a first-order-accurate forward difference predictor-backward difference corrector:

Forward difference predictor:

$$y_p^i = y^{j-1} + \Delta t^{j-1}\ \dot{y}^{j-1} \qquad (4.25)$$

Backward difference corrector:

$$y_c^j = y^{j-1} + \Delta t^{j-1}\ \dot{y}^j \qquad (4.26)$$

Khesghi & Scriven (1984) suggested performing four steps at the outset with the forward difference predictor-backward difference corrector in order to suppress any unwanted transient induced by initial data. These steps are performed with a constant step size. From the fifth step onward, the integration scheme switches to Adams-Basforth predictor - trapezoid rule corrector, and the step-size is controlled automatically thereafter. Figure 4.3 shows the flowchart of the complete integration scheme as applied in the present work.

The above predictor-corrector scheme was employed in the present work to integrate in time the coupled system of algebraic and ordinary differential equations, eq.(4.13). The integration scheme essentially offers a discrete approximation of the time derivatives in eq.(4.13), thereby reducing the problem to the solution of a nonlinear algebraic set of equations at every time step. The Newton-Raphson iterative method was again employed to solve the nonlinear algebraic set. Typically, the Newton-Raphson iteration approached quadratic convergence as shown in Figure 4.4. This figure shows that after one iteration the Euclidean norm of the residuals has been reduced below 10^{-4}. Gresho et al
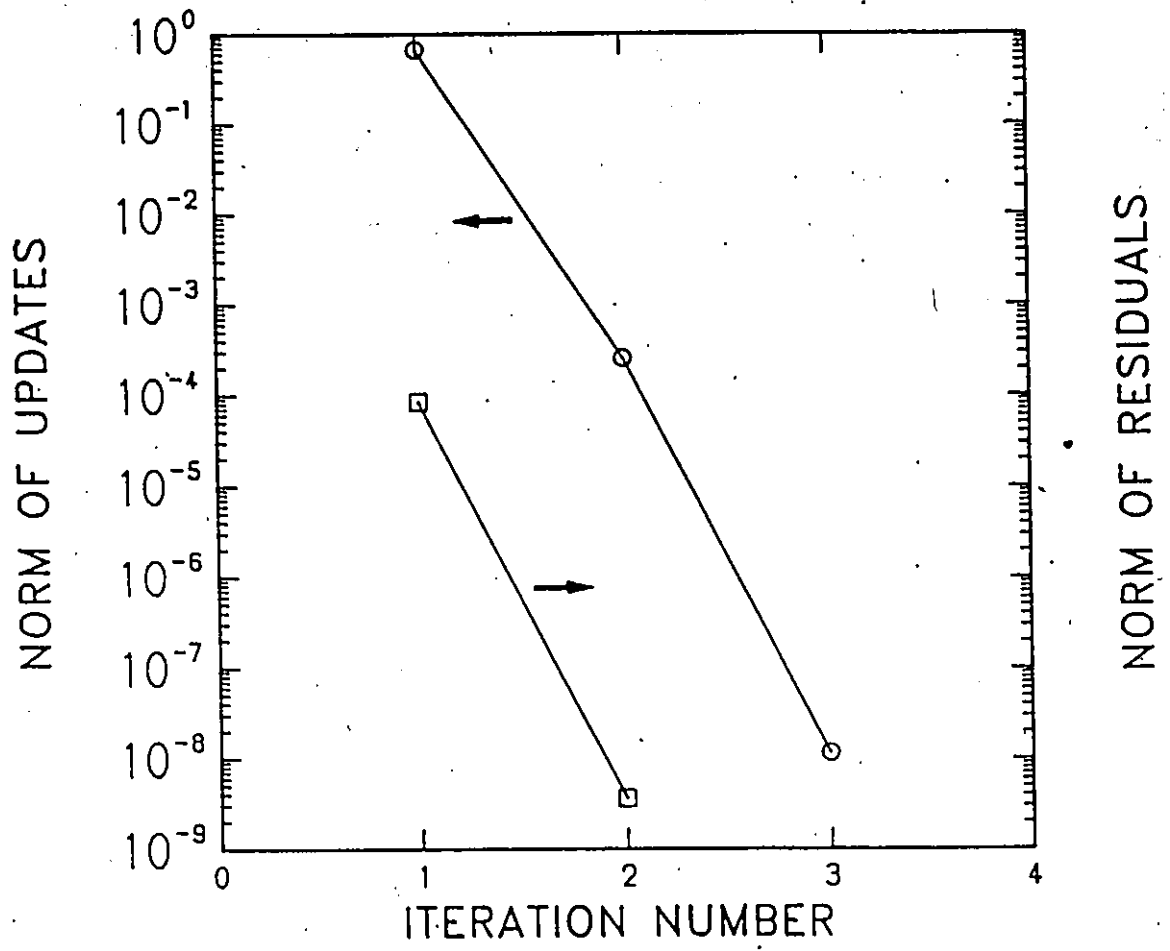
Figure 4.4   Behavior of Newton-Raphson iteration

(1979) and Khesghi & Scriven (1984) have taken advantage of this behavior of Newton-Raphson and allowed only one iteration per step. In this work 2-3 iterations were required to reduce the maximum relative update below 10^{-4}. This conservative convergence criterion was imposed in order to ensure a high accuracy in the determination of the free surface shape, which is of main interest for the problems studied.

4.3 Start-up Flow of a Fluid with a Free-Front

We study the start-up flow of a fluid with a free-front initially at rest, in both planar and axisymmetric geometries. A schematic diagram of the problem is given in Figure 4.5. Gravity and surface tension effects are neglected, so that the fluid-gas interface is initially flat and perpendicular to the walls (90° contact angle). These conditions correspond to the experiments of Behrens (1983).

For a typical simulation the finite element grid consists of 45 elements and 199 nodes. The total number of unknowns (u-v-p-h-δ) is 412 and each time step requires 30 CPU seconds on a VAX 8600. The usefulness of having a variable midside spine direction (δ-variables) is shown in Figure 4.6, which is a plot of the evolution of the free surface segment near the wall. It is shown that the corner node moves along the constant-direction spine (straight trajectory) while the midside spine direction changes (curved trajectory) so that the midside node remains always at the mid-point of the free surface arc and the element is well-shaped.

Figure 4.7 shows the evolution of the contact angle, front tip and contact line positions for transient flow in a tube. Up to the time that the contact angle becomes 180° the contact line does not move (its position is specified as an essential boundary condition). This time is predicted to be 0.2272 (in R/U units) and the front tip position $Z_{FT} = 0.3736$ (0.26 and 0.3508 respectively for the planar case). Behrens et al (1987) report an experimental $Z_{FT} = 0.4$

when the contact line begins to move. This is 7% higher than the present result, but this difference is not significant in view of the very slow initial motion of the contact line (Z_{CL} is predicted to be 0.0085 when Z_{FT} becomes 0.4). When the contact angle becomes 180°, the contact line is allowed to move, and the boundary condition at the contact line is changed to that of a 180° contact angle. Therefore the contact angle remains at 180° for all subsequent times. The contact line starts moving slowly and its velocity approaches asymptotically the average velocity of the fluid. At t=2.055 R/U (Z_{FT}=2.34) the ($Z_{FT}-Z_{CL}$) difference reaches 99% of the steady-state value, and after this time the flow can be considered steady for a moving frame of reference.

Similar results were found for flow in a planar geometry. Figure 4.8 shows the evolution of the free surface shape. A steady-state is reached at t=2.72 H/U (i.e., at this time the ($x_{FT}-x_{CL}$) difference reaches 99% of the steady-state value. At this time x_{FT}=2.92). After this time the flow field remains invariant with respect to a frame of reference moving with the average velocity of the fluid and the problem can be analyzed in the steady-state (Chapter 3).

Behrens (1983) performed experiments with Newtonian fluids in tubes. Data were reported (see also Behrens et al, 1987) in the form of the ($Z_{FT}-Z_{CL}$) difference versus front travel (Z_{FT}). Comparison of the present simulations with Behrens' experimental data is given in Figure 4.9. The data symbols correspond to different experiments with polybutene, and the scatter does not correlate with process variables but merely reflects experimental error. The agreement of simulation with experiment is remarkably good. Behrens (1983) and Behrens et al (1987) also presented simulations with a finite element method, where the free surface and the flow field were decoupled. Good agreement with the experiments was found. The predicted motion of the contact line showed slight oscillations which do not appear with the present algorithm. The major advantage of the present approach is the free surface

parametrization strategy and the coupled technique for determining simultaneously the free surface and the flow field. Coupling allows the use if the Newton-Raphson iterative scheme for the solution of the global nonlinear system of algebraic equations. The quadratic convergence of the Newton-Raphson scheme reduces considerably the computational cost.

The evolution of the finite element grid, for the axisymmetric case, is shown in the upper part of the plots in Figure 4.10. This figure illustrates how the grid deforms and expands, adjusting automatically to the changing free surface shape. The area of the flow domain increases with time since there is no outflow region. This increase was accommodated by expanding the size of the upstream elements only. The grid density in the front region, where the flow rearrangement occurs, remained nearly independent of time, thus avoiding a degradation of accuracy at large times.

The mechanism of flow front advancement can be better understood by tracking material elements, i.e. in the Lagrangian frame. We begin with rectangular material elements at zero time, as shown in figure 4.10. The deformation history was followed by tracking numerically a large number of material points along the perimeter of the fluid element, as described in Section 3.3. Consider first the fluid element adjacent to the flow front ; the evolution of its shape, shown in the lower part of the plots in Figure 4.10, illustrates clearly the rolling motion of the fluid over the solid surface, and how material from the flow front is deposited on the wall giving rise to the apparent motion of the contact line.

The evolution of the shape of the second element in Figure 4.10 is characteristic of the deformation experienced by the fluid due to fountain flow. The faster moving material near the centerline enters the flow front region where it decelerates spilling outward toward the walls. The fluid element is stretched and deformed into a mushroom-like shape ($t = 2.27$), forming characteristic V-shapes near the wall ($t = 4.15$).

t=0

QUIESCENT
    FLUID \

GAS

t=0$^+$
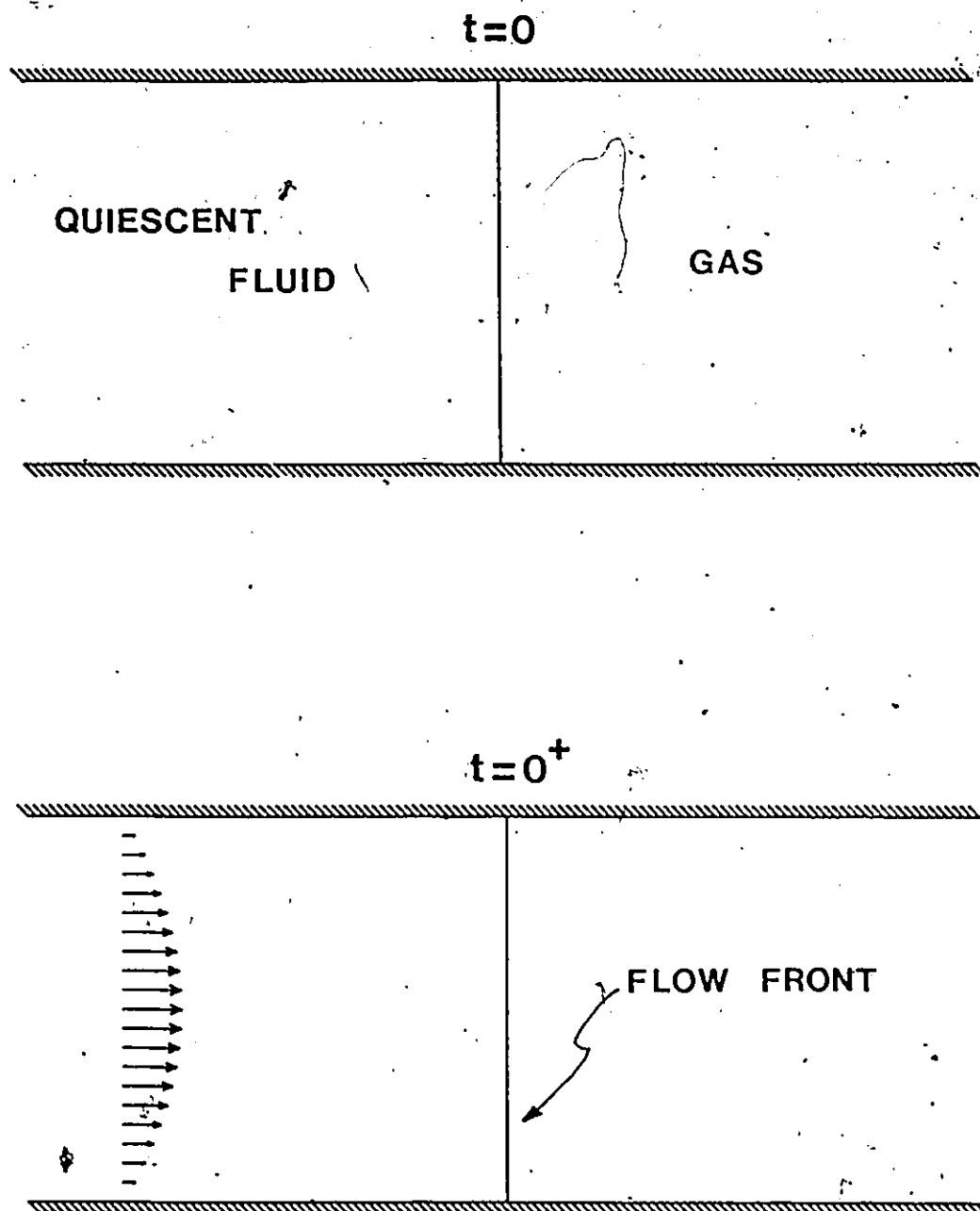
FLOW FRONT

Figure 4.5   Schematic of the start-up flow problem
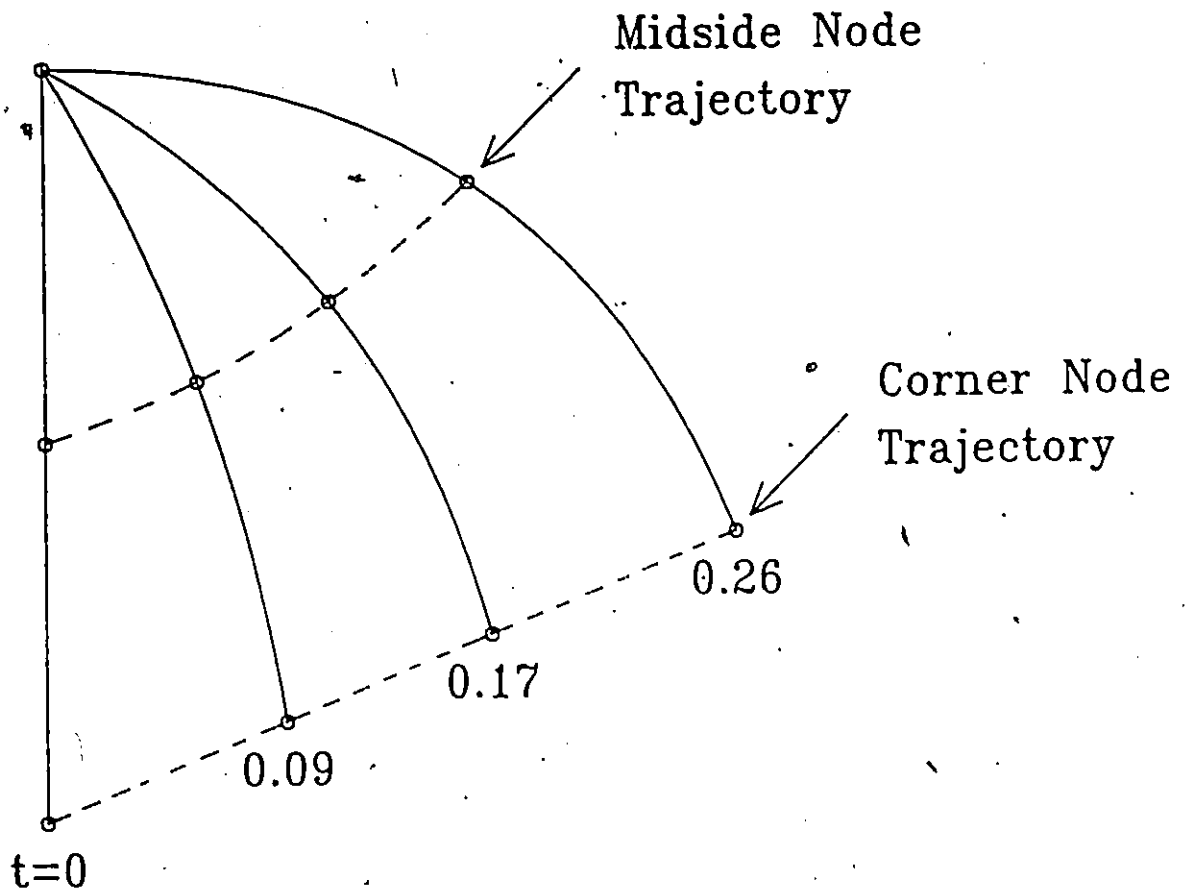
Figure 4.6   Evolution of corner free surface segment
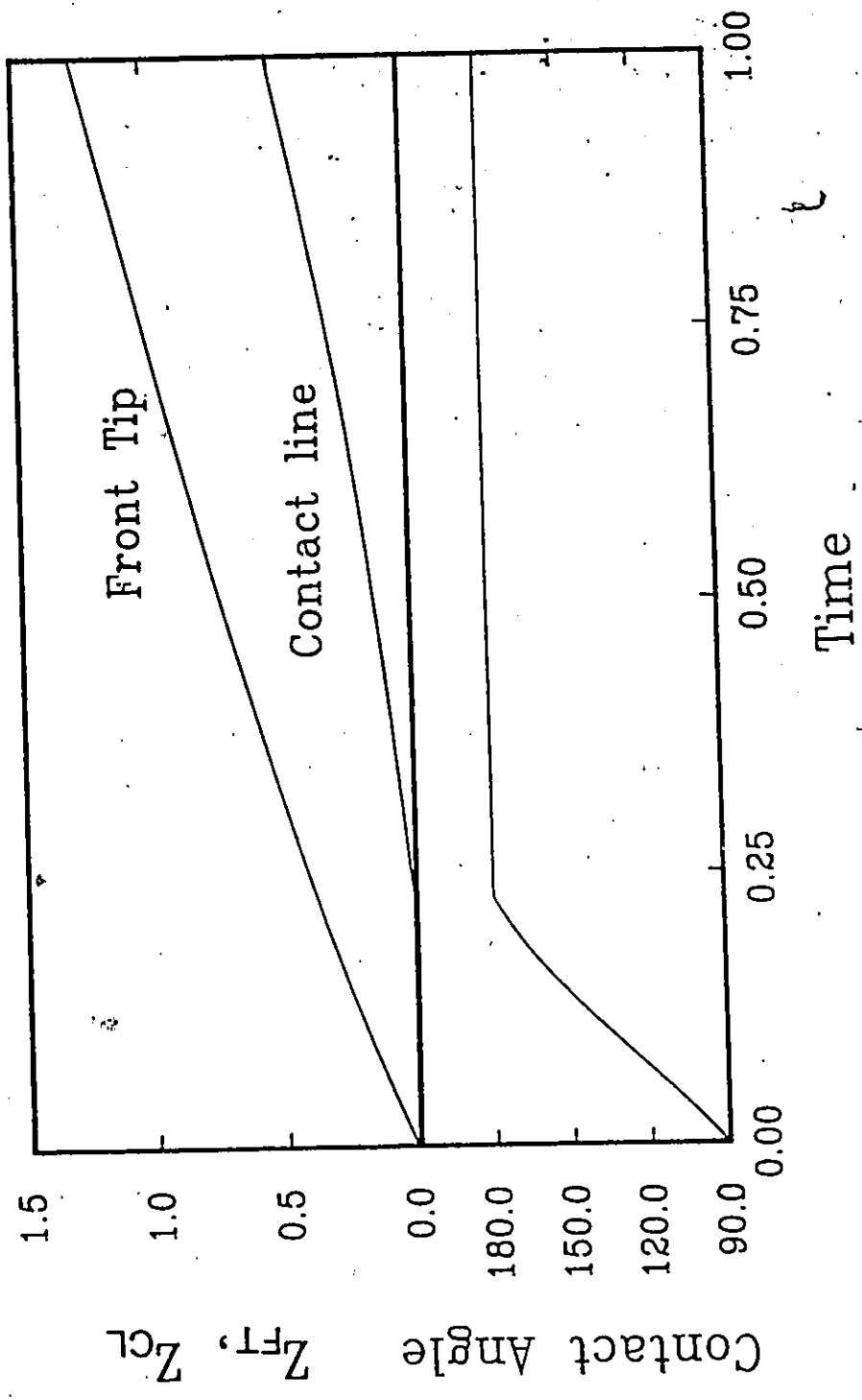
Figure 4.7   Evolution of contact angle, front tip and contact line position (axisymmetric)
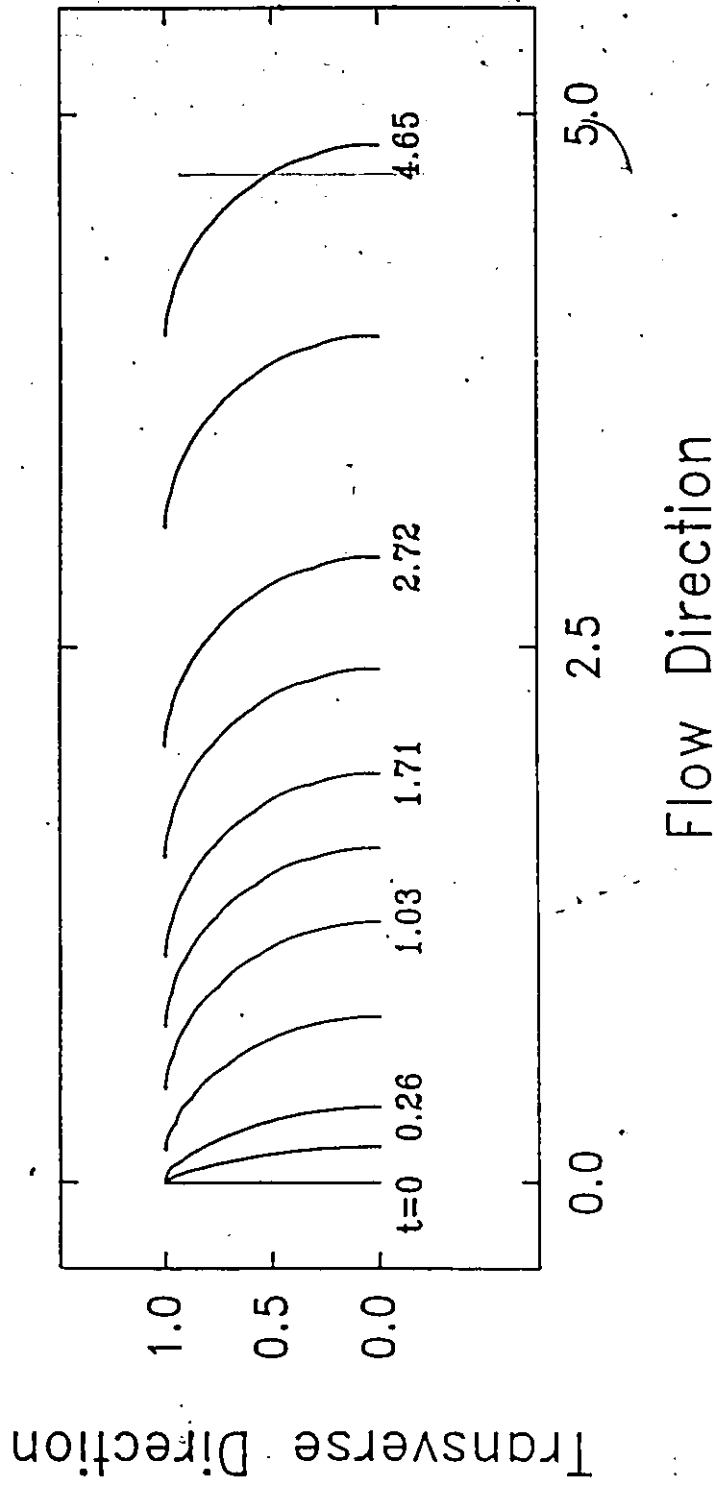
Figure 4.8   Evolution of flow front shape (planar)
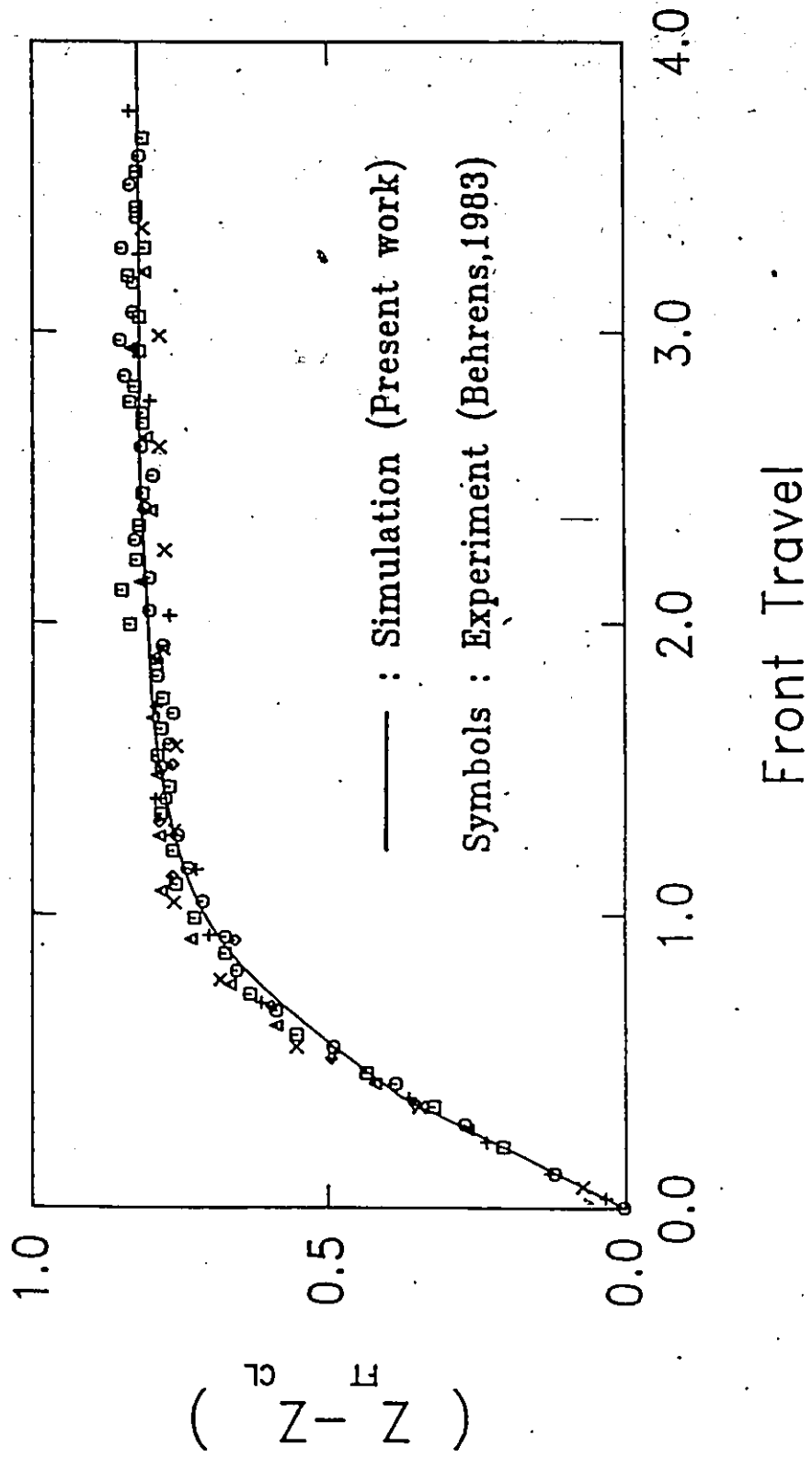
Figure 4.9 $(Z_{FT}-Z_{CL})$ versus front tip position (Z_{FT})-(axisymmetric)
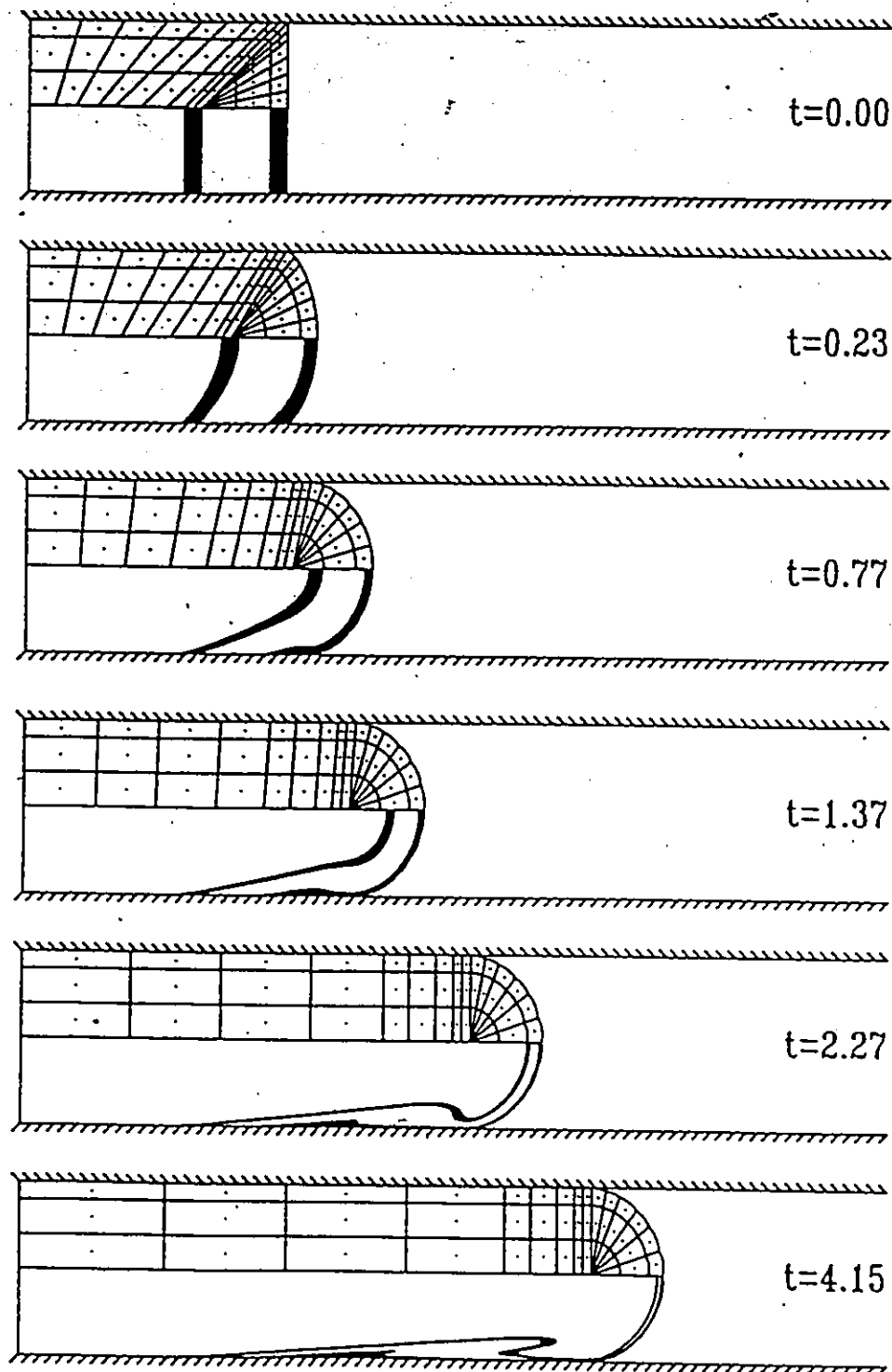
Figure 4.10   Evolution of finite element grid and fluid element shapes (axisymmetric)

4.4   Colliding Flow Fronts

We study the fluid mechanics of two colliding flow fronts to form a weldline. This situation arises frequently in commercial molds due to injection through multiple gates or recombination of two flow fronts divided after passage around an insert. During the impingement phase, polymer molecules are stretched and oriented parallel to the polymer-polymer interface. Depending on the local thermal conditions, this orientation may be frozen-in resulting in incomplete bonding and reduction in the strength of the weldline. Sang-Gook & Suh (1986) offer a recent review and analysis of the problem.

Consider the symmetrical impingement of two flow fronts in a parallel plate geometry, as shown in Figure 4.11. Creeping Newtonian flow and constant flowrate conditions are assumed in the simulations. The problem is solved in a quarter of the flow domain taking into account symmetry considerations.

At t=0 the flow fronts meet at the centerline. The shape of the free surface, required as an initial condition, is taken from the steady-state solution of the fountain flow problem (Section 3.2). The present transient algorithm is then applied to obtain the solution in time. The time required to fill the vacant space can be estimated a priori by dividing the area of the vacant space with the constant flowrate per unit width. This time is estimated to be 0.212 in H/U units (where H is the half-gapwidth and U is the average velocity). At this time no more flow can occur (incompressible fluid) and the algebraic system of equations is singular. The numerical algorithm stopped at t=0.21, leaving a small vacant area at the surface (Figure 4.12). This area is the last to be filled, and in practice the air trapped in it may cause an optically visible defect in the shape of a notch at the surface (Hagerman, 1973 ; Sang-Gook & Suh, 1986).

The evolution of the flow field is shown as the series of instantaneous streamlines in the upper part of the plots in Figure 4.12. At zero time the curvature of the streamlines

reflects the outward motion of the fluid due to fountain flow. As the weldline forms at the centerline and develops towards the wall, the elongational component of the deformation increases and the streamlines bend parallel to the weldline. At the end the flow resembles planar stagnation flow. In fact, the planar stagnation flow model of Tadmor (1974) has frequently been used to explain the flow induced orientation parallel to the weldline.

The impact of weldline formation on the deformation of the material was investigated by tracking numerically a gridded band of material behind the flow front. This material is already stretched due to fountain flow but we examine here the stretching induced during the impingement phase. The evolution of the fluid element shapes is shown in the lower part of the plots in Figure 4.12. The material elements become stretched and oriented parallel to the weldline, and stretching is more pronounced near the centerline, while near the wall shearing orients the material parallel to the wall. This is better illustrated in Figure 4.13, which is a magnification of the band of material immediately adjacent to the flow front. This material has already experienced the fountain flow induced deformation before the collision of the two fronts. Comparison of the fluid element shapes in Figures 4.13 and 4.10 shows that stretching due to fountain flow is much larger (see also Section 3.3). While some orientation of the material is introduced during the collision phase, it appears from the present results that fountain flow is mostly responsible for the anisotropy at weldlines of injection molded parts.

It is interesting to note the actual length and time scales involved in weldline formation. For a typical case, with an average velocity $U = 0.1$ m/s and a half-gapwidth $H = 0.001$ m the weldline forms in 0.21 H/U = 2.1 milliseconds. Experiments are difficult to perform and their analysis is a laborious off-line procedure. Numerical simulations can be of invaluable assistance providing insight into the process at time and length scales that are difficult to capture or reproduce experimentally.

t<0

t=0
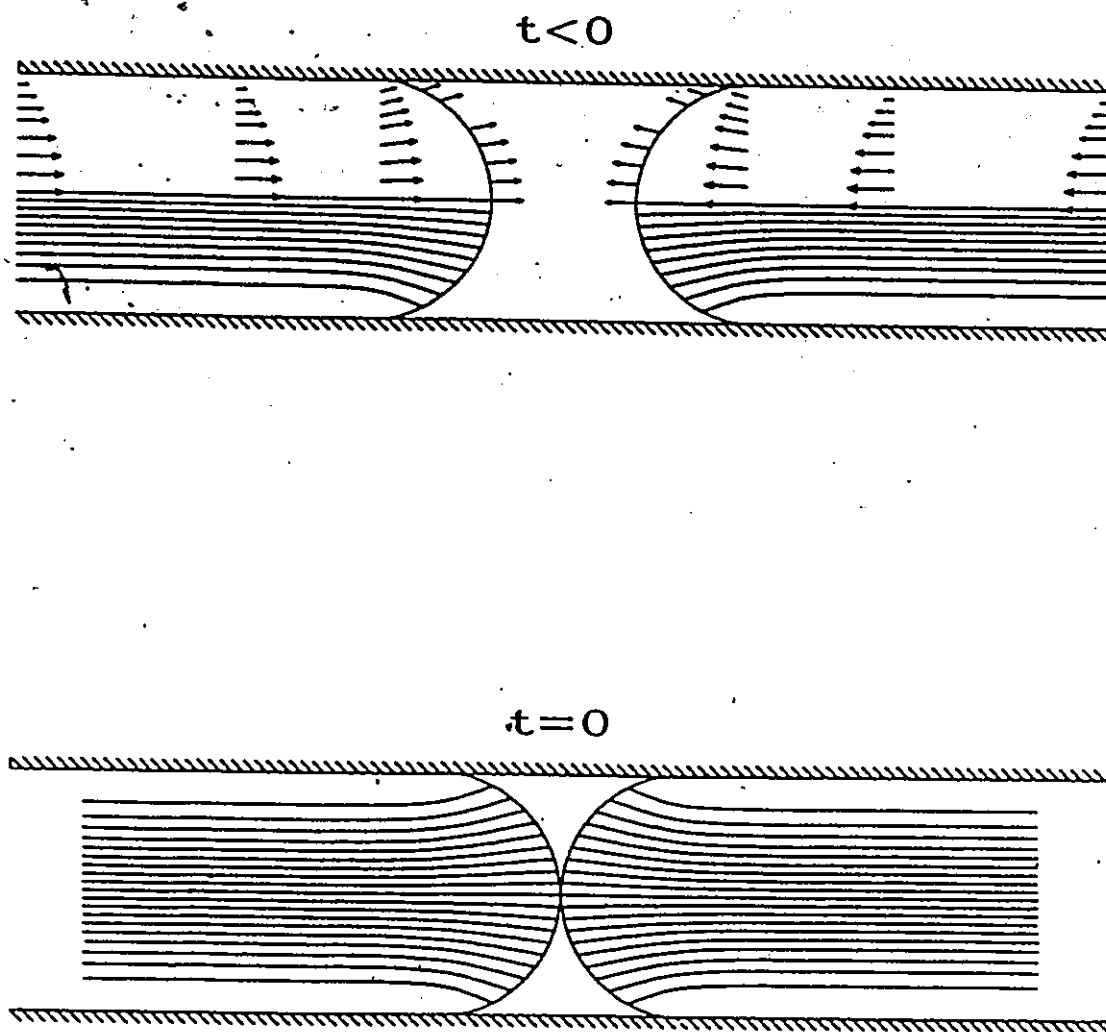
Figure 4.11   Colliding flow fronts

t=0.000

t=0.054

t=0.108

t=0.168

t=0.198

t=0.210
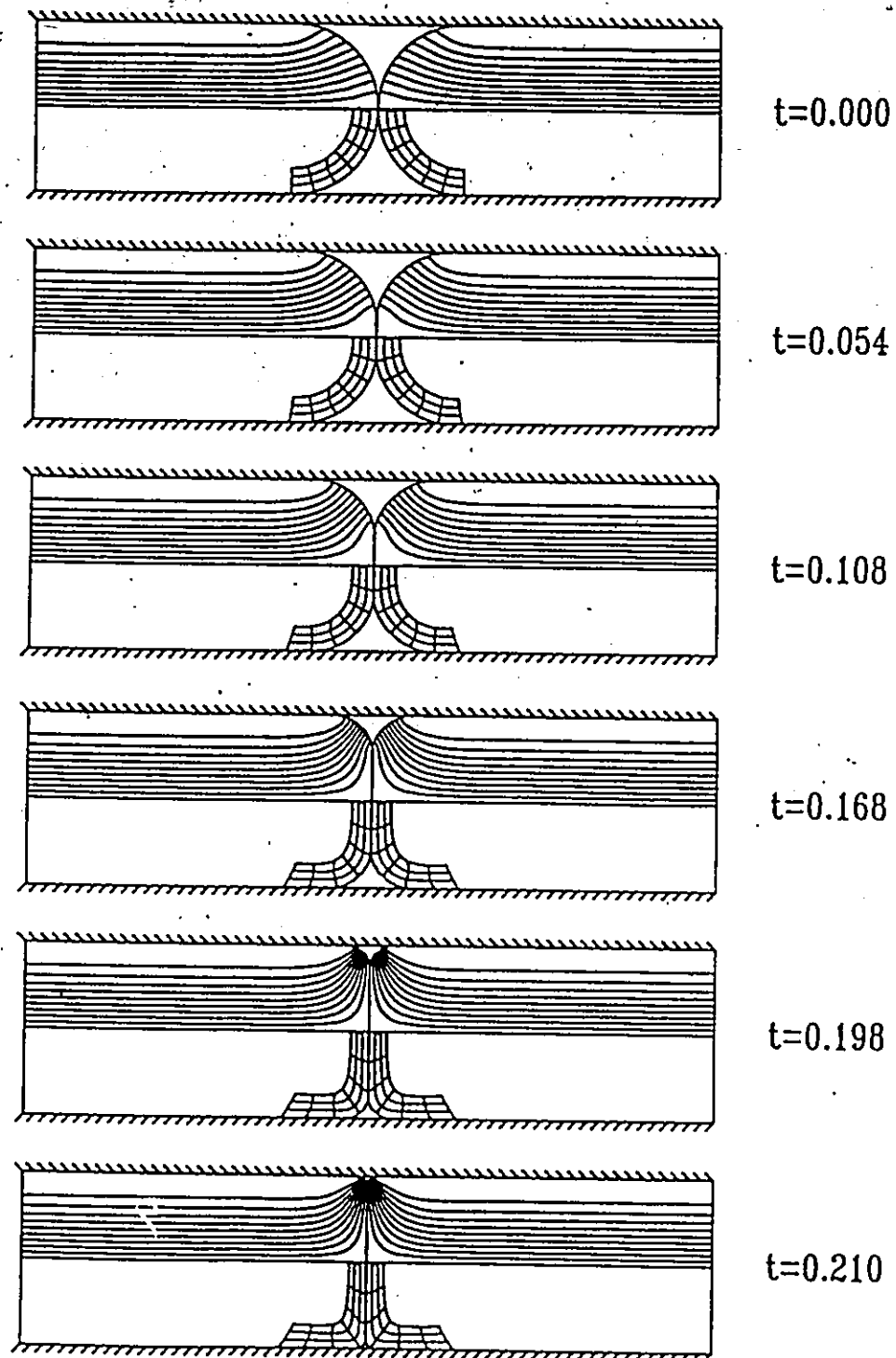
Figure 4.12   Evolution of instantaneous streamlines and fluid element shapes

t=0.21

t=0.108

t=0
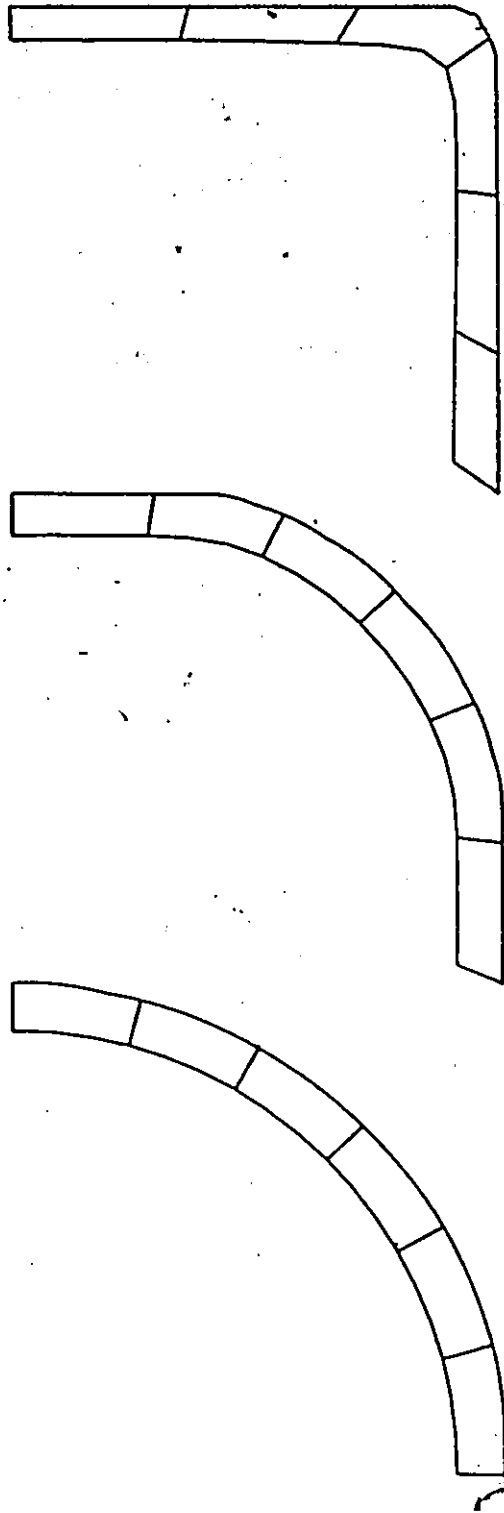
Figure 4.13   Magnification of fluid element shapes adjacent to the flow front

4.5   Concluding Remarks

A comprehensive algorithm has been described for the numerical simulation of transient free surface flows encountered in injection mold filling. The algorithm combines the Galerkin/Finite Element discretization of the governing equations with a predictor-corrector scheme for temporal integration. It determines simultaneously the flow-field and the free surface shape at every time step and can handle deforming flow domains with moving contact lines.

The numerical technique was employed to study the start-up flow of a fluid with a free front, in planar and axisymmetric geometries. It is found that the flow development is completed in a short distance (2.92 half-gapwidths for the planar and 2.34 tube radii for the axisymmetric case). Numerical tracking of material elements illustrate the rolling-type advancement of the fluid over the solid surface, and the V-shape formation, and show the same features of flow as those observed in the steady-state analysis. Computational results are compared to, and agree favorably with available experimental measurements.

The problem of two symmetrically colliding flow fronts was also examined (weldline formation in the gapwise direction). Tracking of material elements was employed to investigate the deformation experienced by the fluid. It was found that the material is stretched and oriented parallel to the weldline. However, the deformation induced during the collision phase is small when compared to that due to fountain flow. It appears that fountain flow is mostly responsible for the anisotropy near weldlines of injection molded parts.

CHAPTER 5

THE EFFECT OF FOUNTAIN FLOW ON THE MOLECULAR

ORIENTATION OF INJECTION MOLDED PARTS

In this chapter we investigate the impact of the fluid mechanics of mold filling on the molecular orientation of the final part, as reflected in available birefringence measurements. A quantitative evaluation of the flow-induced molecular orientation requires adequate description of the dynamics of the flow. The viscoelasticity of the polymer melt is of primary importance for this purpose and is accounted for with the multi-mode Leonov model. A finite element algorithm for the numerical simulation of viscoelastic free surface flows is presented and is applied on the fountain flow problem. Converged solutions are obtained for processing conditions corresponding to available experiments. The finite element results are combined with a simplified theory to predict frozen-in birefringence distributions. Computational results are compared to, and agree favorably with, available birefringence measurements. The effect of fountain flow on the molecular orientation of injection molded parts is clearly demonstrated.

5.1   Introduction

Injection molded articles of amorphous polymers exhibit an anisotropy in the optical and mechanical properties due to frozen-in orientation of the polymer chains. To a large extent this orientation is created during the nonisothermal mold filling stage; polymer molecules tend to orient while flowing under the action of the prevailing stress field. If the molten polymer is cooled rapidly to a temperature below its glass transition temperature (T_g) the polymer molecules will not have sufficient time to relax their orientation and return to a

random configuration. This is particularly the case in commercial molds which are held at temperatures below T_g and a solidified layer in the order of 10% of the mold thickness is already built-up at the outer surfaces of the part by the end of the filling stage. Since polymer molecules at different locations of the final molded part have generally experienced different deformation histories prior to their solidification, they will be oriented in varying degrees and therefore complex <u>distributions</u> of molecular orientation are to be expected.

A second source of orientation is due to the continued cooling of the molded part after the completion of the filling process. During this cooling non-equilibrium density or shrinkage changes occur that result in thermal stresses. In fact, high back pressures are maintained after mold filling (packing stage) and additional melt flows into the mold to compensate for density changes and ensure accurate reproduction of the mold shape.

The final anisotropy of the molded part is a composite effect due to both flow- and thermally-induced orientation. However, from experimental investigations with birefringence measurements on molded and quenched strips (Isayev, 1983), it appears that thermally induced orientation is an order of magnitude smaller than flow-induced orientation. It is believed (Janeschitz-Kriegl, 1983) that flow-induced orientation accounts for most of the composite birefringence pattern of injection molded parts.

Two experimental techniques for investigating orientation in injection molding are: birefringence measurements and shrinkage at elevated temperatures of microtomed samples cut from the product. Experimental and theoretical considerations for the birefringence and shrinkage techniques are provided in Isayev, 1983; Janeschitz-Kriegl, 1983; Wales, 1972, 1976; Fleissner, 1973; Bakerdjian & Kamal, 1977; Kamal et al., 1977; Dietz et al., 1978; Dietz & White, 1978; White & Dietz, 1979; Kamal & Tan, 1979; Isayev & Hieber, 1980 and Bakerdjian & Kamal, 1977; Kamal et al., 1977; Menges & Wübken, 1973; Menges & Thienel, 1975; Menges et al., 1976 respectively. Birefringence is the most widely

used technique. In addition to being an important property in itself (e.g. for optical lenses, compact disks) what makes birefringence particularly attractive, from a rheological point of view, is the stress optical rule. This rule states that the refractive index and stress ellipsoids are coaxial and the birefringence (difference in magnitude of the principal values of the refractive index tensor) is proportional to the corresponding difference in principal stresses (Wales, 1976), i.e.

$$n - \frac{1}{3} \, \mathrm{tr}(n) \, I = C \left(\sigma - \frac{1}{3} \mathrm{tr}(\sigma) \, I \right) \qquad (5.1)$$

where n, σ, I are the refractive index, stress and unit tensors respectively and C is the stress-optical coefficient, which for most polymer melts is a constant (Wales, 1976). Knowledge of the stress field and the stress-optical coefficient allows, with the aid of eq. (5.1), direct evaluation of the birefringence and comparison with experimental measurements.

Experimental investigations on birefringence of injection molded parts are usually performed on molded strips. The configuration and the notation to be followed are shown in Figure 5.1: x- is the flow direction, y- is the thickness direction (direction of the velocity gradient) and z- is the width (neutral) direction. Birefringence measurements are performed on slices cut from the part, and results are usually reported in the form of variations of Δn with y, for various positions X from the gate. From eq. (5.1), Δn is related to the stresses with:

$$\Delta n = C[(\tau_{xx} - \tau_{yy})^2 + 4\tau_{xy}^2]^{1/2} \qquad (5.2)$$

A typical distribution of Δn in the thickness direction is shown in Figure 5.2. The data points represent experimental measurements of Kamal & Tan (1979). The solid line is the birefringence that would be measured in an isothermal shear flow of the material at the same shear rate and at the injection temperature. It is plotted only for comparison and for the sake of the discussion to follow.
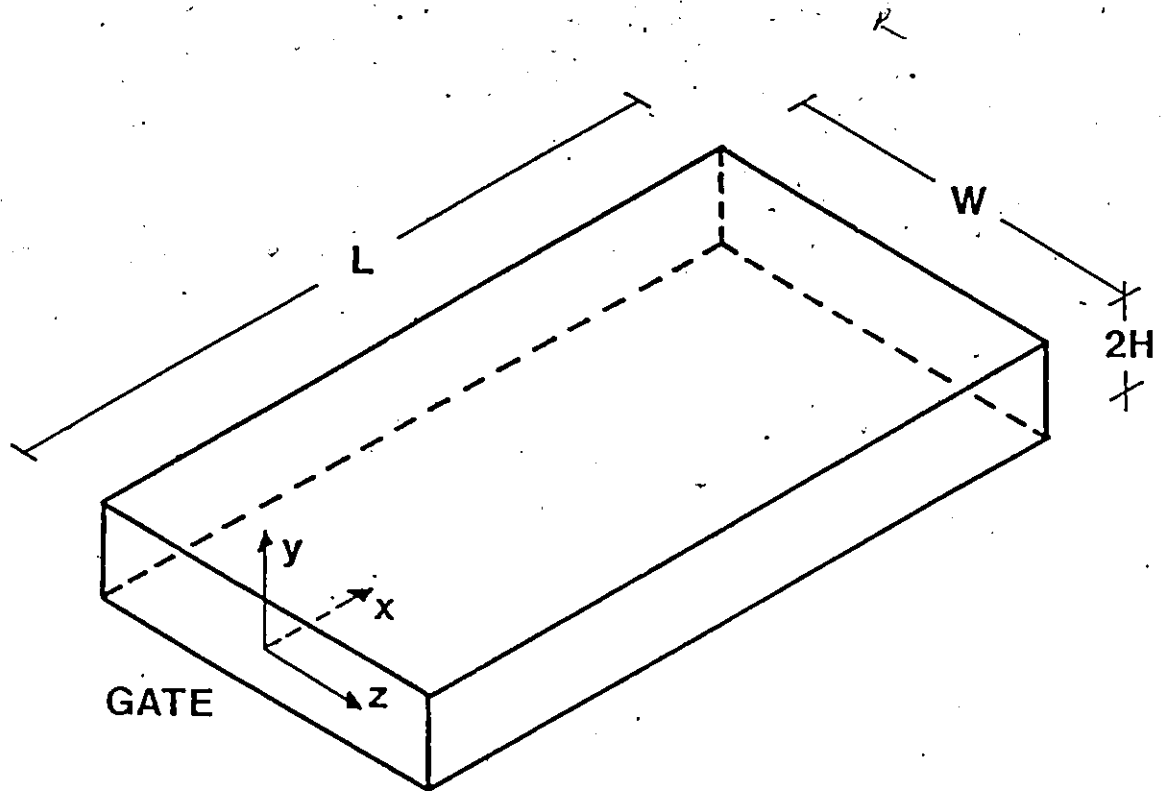
Figure 5.1   Schematic diagram of rectangular mold geometry
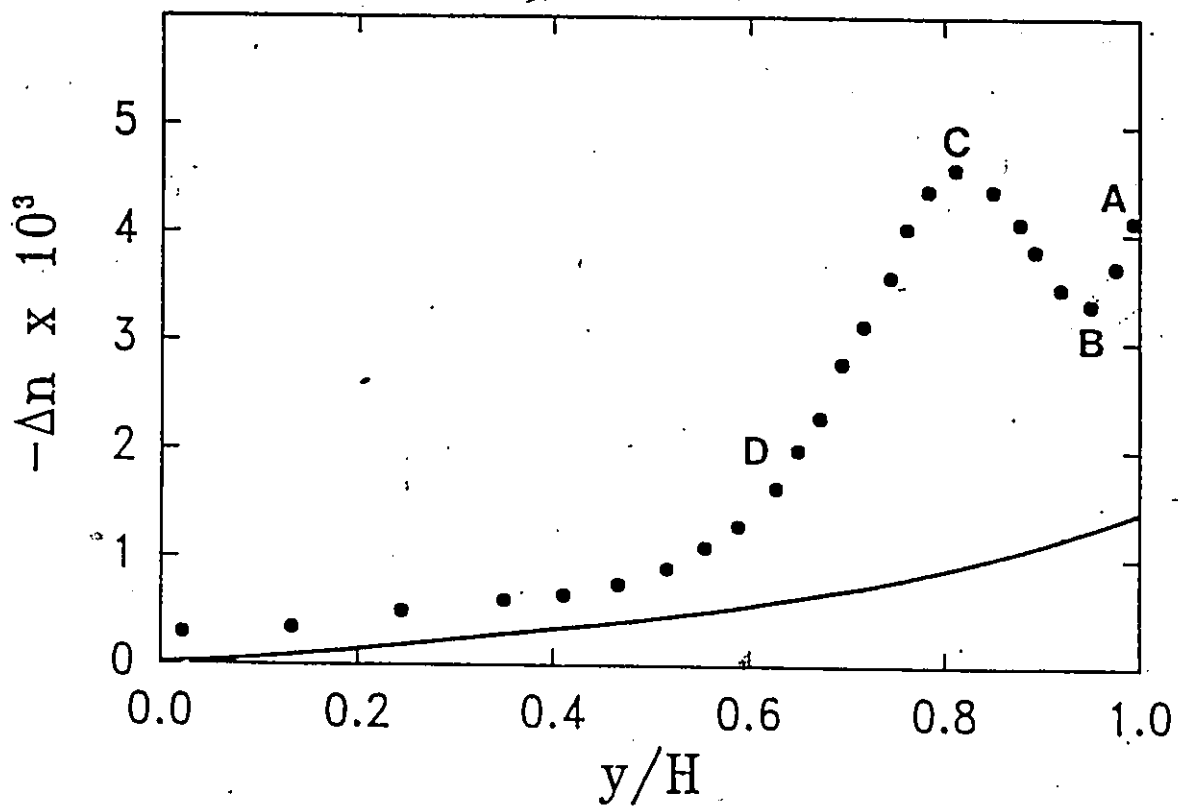
Figure 5.2   Gapwise distribution of birefringence: experimental measurements of Kamal & Tan (1979) (symbols) and theoretical prediction in isothermal flow (solid line)

Assume, in a hypothetical experiment, a constant flow rate, isothermal flow in a slit. The birefringence Δn will be the solid line in Figure 5.2. Now let us assume that the walls are brought instantaneously to a temperature T_w below the glass transition temperature of the polymer. Then a solid layer will begin to grow from the walls towards the center. Consequently, the stress levels will begin to rise with a maximum near the melt-solid interface (stresses developed in the surface layer after solidification do not contribute to the frozen-in birefringence, Janeschitz-Kriegl (1983)). The polymer nearest the wall is frozen at earlier times than the inner layers and therefore at lower stress levels. Thus we expect a birefringence profile similar to the BCD part of the experimental curve in Figure 5.2. However, the AB part of the curve is not explained by considering only shear flow and solidification at the walls. In fact, in the above hypothetical experiment the CB part of the curve should continue decreasing monotonically up to the wall, with point A having the minimum birefringence. The experimentally shown trend with the birefringence increasing near the wall (part BA) indicates the presence of a highly oriented skin layer. The skin-core structure is typical of injection molded parts and its origin must be sought in the fluid mechanical details of the injection mold filling process.

The salient feature of mold filling is the fountain flow behind the advancing flow front. Tadmor (1974) was the first to postulate fountain flow as responsible for the highly oriented surface layer; the front advances in a kind of a rolling-type motion whereby fluid elements from the centerline reach the wall passing through a complex shear and elonga- tional flow in the front region. Tadmor neglected the shear contribution and assumed that the elongational deformation at the front causes the high orientation of the surface layer. He employed the bead-and-spring macromolecular theory and developed a semiquantitative model that was able to explain the molecular orientation distribution of molded parts as determined by the shrinkage measurements of Menges and Wübken (1973).

The visualization experiments of Schmidt (1974) shed further light into the kinematics of injection mold filling. As discussed in detail in Chapter 3, in Schmidt's experiments color tracers introduced at the centerline were found at the surface of the final part deformed into V-shapes. The color tracers were highly stretched and oriented in the flow direction. Both the migration of the color tracers towards the wall and their orientation support the hypothesis that fountain flow plays a dominant role on the molecular orientation development of the surface layers of injection molded parts.

Various attempts to approach theoretically the development of molecular orientation in injection molding have so far involved major simplifications and focused on a subset of the general problem. This is not surprising in view of the enormous complexity of the original problem in its full generality (transient, three dimensional, nonisothermal, free surface flow of a viscoelastic fluid, followed by nonisothermal stress relaxation after cessation of flow). White and co-workers (Dietz et al., 1978; Dietz & White, 1978; White & Dietz, 1979) have considered unidirectional nonisothermal shear flow and employed Tadmor's (1974) model to account for the effect of fountain flow. Isayev and Hieber (1980) developed a theory along similar lines, using the Leonov viscoelastic model but neglecting the fountain effect. Kim and Suh (1987) studied the nonisothermal stress relaxation in low thermal inertia molding using the Wagner viscoelastic model. Janeschitz-Kriegl (1977,1979) and Van Wijngaarden et al (1982) have examined the heat transfer problem and the formation of a solidified layer during mold filling.

A quantitative evaluation of the effect of fountain flow on the molecular orientation of injection molded parts requires a detailed description of the flow field in the front region. The viscoelasticity of the polymer melt is of primary importance for this purpose and must be accounted for with an appropriate constitutive equation. For a frame of reference moving with the average velocity of the fluid and assuming isothermal conditions the

problem can be solved in the steady-state (Chapter 3). Even though the isothermality condition is a simplification, it appears a reasonable approximation in the flow front region where the fluid has the minimum contact time with the cold wall and temperature variations are not expected to be large enough to disturb the flow appreciably. The Leonov viscoelastic model (Leonov, 1976) as applied by Upadhyay & Isayev (1986) was used in this work. A recent discussion of this model and further references are given by Leonov (1987).

A finite element algorithm is presented for the numerical simulation of the fountain flow problem with the Leonov viscoelastic model. Converged solutions are obtained at high levels of elasticity and are checked with mesh refinement. Frozen-in stresses and birefringence distributions are calculated with a modification of the theory developed by Isayev & Hieber (1980). Computational results are compared to, and agree favorably with, various sets of experiments available in the literature.

5.2   Fountain Flow of a Viscoelastic Fluid

5.2.1   The Leonov Viscoelastic Model

The constitutive equation relating stress to the rate-of-strain according to the multi-mode Leonov model is (Upadhyay & Isayev, 1986):

$$\sigma = -P\,I + s\,\eta_0(\nabla V + \nabla V^T) + \sum_{k=1}^{N} \frac{\eta_k}{\theta_k}\, C_k \tag{5.3}$$

where σ is the total stress tensor, P is the pressure, V is the velocity vector, η_k and θ_k are the shear viscosity and relaxation time in the k-th mode of the Leonov model, s is a rheological parameter lying between zero and one, and η_0 is the zero shear viscosity:

$$\eta_0 = \sum_{k=1}^{N} \eta_k / (1-s) \tag{5.4}$$

where N is the number of modes in the Leonov model. C_k is the elastic strain tensor of the k-th mode in the Leonov model and is given by:

$$\overset{\triangledown}{C}_k + \frac{1}{2\theta_k}(C_k \cdot C_k - I) = 0 \tag{5.5}$$

where ($\triangledown$) signifies the upper-convected derivative:

$$\overset{\triangledown}{C}_k = \frac{\partial}{\partial t} C_k + V \cdot \nabla C_k - \nabla V^T \cdot C_k - C_k \cdot \nabla V \tag{5.6}$$

The predictive capabilities of the Leonov model have been tested in various flow situations: one-dimensional steady (Upadhyay et al., 1981) and oscillatory (Isayev & Hieber, 1982) flow, multistep shear deformation (Upadhyay et al., 1983), uniaxial elongational flow (Upadhyay & Isayev, 1983) and non-isothermal elongational flow (Upadhyay & Isayev, 1984), two-dimensional channel flow in converging and diverging geometries (Isayev & Upadhyay, 1985), injection molding (Isayev & Hieber, 1980) and bubble growth in foam injection molding (Upadhyay, 1986).

It is instructive to note the Leonov model predictions in two-dimensional shear flow between parallel plates (Poiseuille-type flow):

Viscosity:

$$\mu = s\eta_o + \sum_{k=1}^{N} \frac{2\eta_k}{1+Q_k} \tag{5.7}$$

First-normal stress difference:

$$N_1 = \tau_{xx} - \tau_{yy} = \sqrt{2} \sum_{k=1}^{N} \frac{\eta_k}{\theta_k} \frac{Q_k-1}{(1+Q_k)^{1/2}} \tag{5.8}$$

Second-normal stress difference:

$$N_2 = \tau_{yy} - \tau_{zz} = \sum_{k=1}^{N} \frac{\eta_k}{\theta_k} \left[\frac{\sqrt{2}}{(1+Q_k)^{1/2}} - 1 \right] \tag{5.9}$$

where

$$Q_k = [1 + 4\theta_k^2 \dot{\gamma}^2]^{1/2} \tag{5.10}$$

and $\dot{\gamma}$ is the shear rate.

The Leonov model parameters for a typical polymer melt (polystyrene STYRON 678U, Dow Chemical) are given in Table 5.1, along with other properties of this material. The Leonov model parameters were fitted by Isayev & Hieber (1980) using the data of Wales (1976). Two modes were sufficient to fit the data up to a shear rate of 10^3 s^{-1} at a temperature of 190°C.

For this material, the variation of viscosity and normal stress differences with shear rate are shown in Figures 5.3a and 5.3b respectively. It can be observed that the model predicts a shear-thinning viscosity, a positive first normal stress difference and a negative second normal stress difference N_2 in the range 5%-20% of N_1. It is remarkable that this model can model real polymeric behavior while retaining a simple form (observe in eqs. (5.3) to (5.6) that the only nonlinearity of the model is the bilinear convective terms in eq. (5.6)) which makes it very attractive computationally.

Table 5.1 Properties of polystyrene STYRON 678U (Isayev & Hieber, 1980)

— Leonov model parameters at $T_0 = 190$°C

$N = 2$, $\quad s = 0,009$, $\quad \eta_1 = 5.44 \times 10^3$ Pa s, $\quad \theta_1 = 0.8$

$\eta_2 = 1.50 \times 10^3$ Pa s, $\quad \theta_2 = 0.027$ s

— Parameters in WLF equation

$C_1 = 2.3 \times 8.86$, $C_2 = 101.6$°C, $T_{ref} = 134$°C

— Glass transition temperature $T_g = 100$°C

— Stress-optical coefficient, $C = -4.8 \times 10^{-9}$ Pa^{-1}

— Thermal diffusivity, $a = 6.2 \times 10^{-8}$ m^2/s
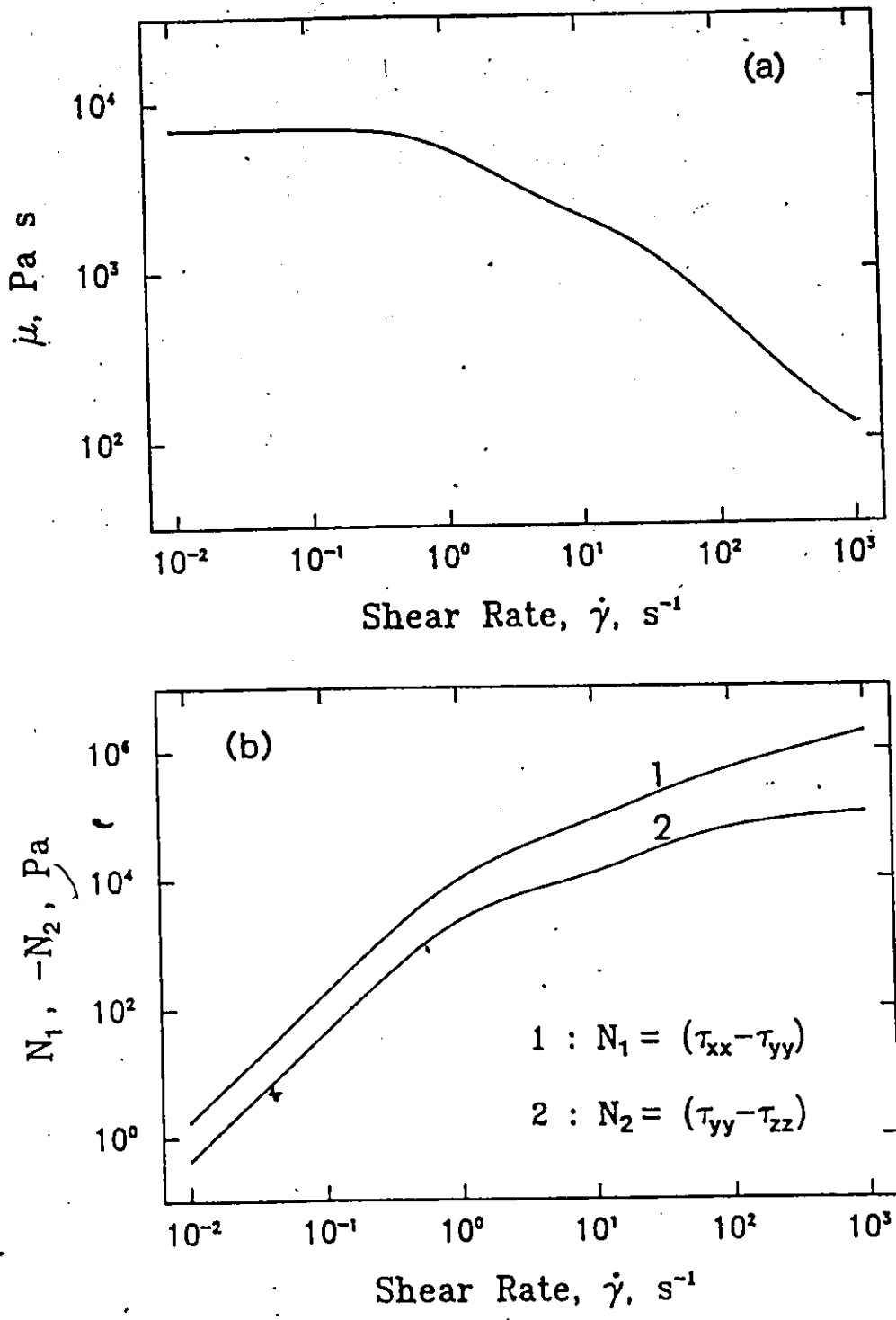
Figure 5.3 Leonov model predictions for (a) viscosity, and (b) normal stress differences (parameters of Table 5.1, T = 190°C)

5.2.2   Determination of fully-developed profiles in shear flow

The fully-developed velocity and elastic strain tensor profiles in pressure-driven

shear flow between parallel plates cannot be obtained analytically from the Leonov model.

However, these profiles are necessary to be imposed as boundary conditions in the finite

element algorithm of the next section. Therefore, they are obtained numerically as described

below.

Consider the pressure-driven shear flow of a fluid with average velocity U between

parallel plates with half-gapwidth H. The governing equations are:

Continuity:
$$\int_0^H u\,dy = U\,H \tag{5.11}$$

x-momentum:
$$0 = -\frac{dP}{dx} + \frac{d}{dy}(\mu\,u_y) \tag{5.12}$$

where μ is given in eq. (5.7). The boundary conditions are:

at $y = 0$: $\qquad\qquad u_y = 0$ (5.13a)

at $y = H$: $\qquad\qquad u = -\beta\,\mu\,u_y$ (5.13b)

where $u_y = du/dy = \dot{\gamma}$ and β is the slip coefficient ($\beta = 0$ for no-slip at the wall). Equations (5.11)

and (5.12) can be modified to yield:

$$\int_0^H \dot{\gamma}\,y\,dy + U\,H + \beta\,\mu\,u_y\Big|_{y=H} = 0 \tag{5.14}$$

$$\mu\,u_y - y\,\frac{dP}{dx} = 0 \tag{5.15}$$

The boundary conditions, eqs. (5.13), have been absorbed in eqs. (5.14) and (5.15).

Equation (5.15) is a differential equation for the shear rate profile $\dot{\gamma}(y)$ and eq. (5.14) is an

algebraic constraint associated with the pressure gradient. These equations are solved as

follows:

(i)   The half-gapwidth $0 \leq y \leq H$ is discretized into M one-dimensional 3-node line elements. This gives $(2M+1)$ nodal points. A shear rate degree of freedom is assigned to each nodal point.

(ii)   There are $(2M+1)$ shear rate degrees of freedom and the pressure gradient $(2M+2$ unknowns). $2M+1$ equations are provided by applying eq. (5.15) to every nodal point, while eq. (5.14) provides the $(2M+2)$-th equation. This is a nonlinear system of algebraic equations which is solved iteratively (Newton-Raphson) to obtain the shear rate at the nodal points and the pressure gradient.

Once the shear rate profile is known the velocities and elastic strain tensor components at the nodal points are computed as follows:

(i)   Velocity: the velocity at the wall $(y = H)$ is computed from:

$$u(y=H) = -\beta \mu \dot{\gamma}(y=H) \tag{5.16}$$

and the velocity at the interior points is computed from:

$$u(y_2) = u(y_1) + \int_{y_1}^{y_2} \dot{\gamma} \, dy \tag{5.17}$$

The integration in eq. (5.17) is performed with Simpson's rule which is exact in the present case, since the shear rate is approximated as piecewise quadratic.

(ii)   Elastic strain tensor components: the elastic strain tensor components for the k- mode in the Leonov model are computed from (Isayev & Hieber, 1980):

$$C_{xx,k} = \frac{\sqrt{2}\,Q_k}{(1+Q_k)^{1/2}}, \quad C_{yy,k} = \frac{\sqrt{2}}{(1+Q_k)^{1/2}}, \quad C_{xy,k} = \frac{2\theta_k u_y}{1+Q_k} \tag{5.18}$$

where Q_k is given in eq. (5.10).

For the rheological parameters of Table 5.1, typical velocity and shear rate profiles as predicted by the Leonov model are given in Figures 5.4a and 5.4b respectively.
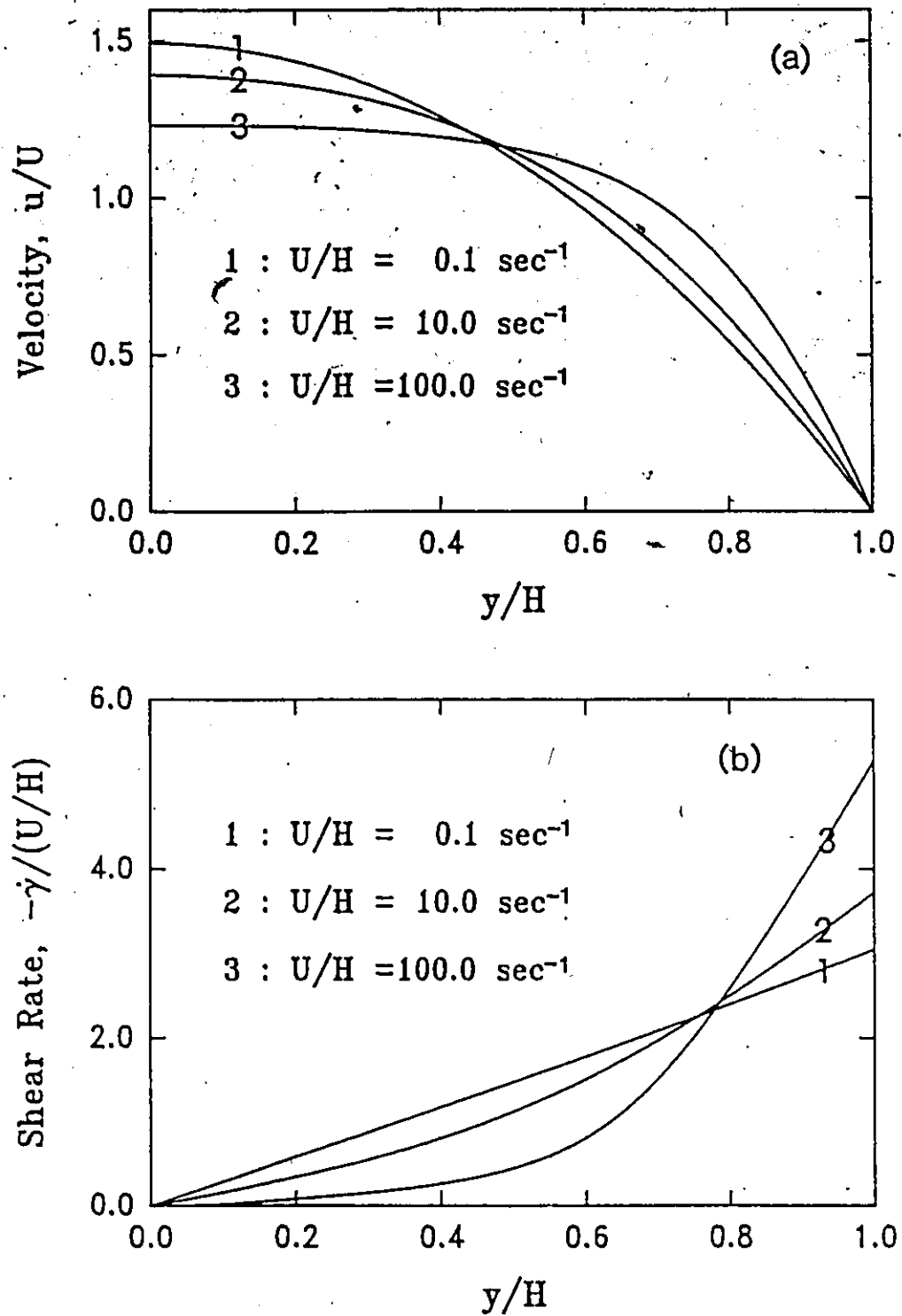
Figure 5.4   Predictions of the Leonov model for (a) velocity, and (b) shear rate, in shear flow (parameters as in Fig. 5.3)

5.2.3   Finite Element Formulation

We consider steady and isothermal flow of an incompressible fluid whose rheological behavior is described by the Leonov model. The governing equations are (neglecting inertia and gravitational effects):

$$\nabla \cdot V = 0 \tag{5.19}$$

$$\nabla \cdot \sigma = 0 \tag{5.20}$$

$$\sigma = -P I + s\eta_0(\nabla V + \nabla V^T) + \sum_{k=1}^{N} \frac{\eta_k}{\theta_k} C_k \tag{5.21}$$

$$\overset{\nabla}{C}_k + \frac{1}{2\theta_k}(C_k \cdot C_k - I) = 0 \tag{5.22}$$

The explicit form of the above equations for two-dimensional planar flow is:

$$\frac{\partial u}{\partial x} + \frac{\partial v}{\partial y} = 0 \tag{5.23}$$

$$-\frac{\partial P}{\partial x} + \frac{\partial \tau_{xx}}{\partial x} + \frac{\partial \tau_{xy}}{\partial y} = 0 \tag{5.24a}$$

$$-\frac{\partial P}{\partial y} + \frac{\partial \tau_{yy}}{\partial y} + \frac{\partial \tau_{xy}}{\partial x} = 0 \tag{5.24b}$$

where

$$\tau_{xx} = \eta_0 s 2 \frac{\partial u}{\partial x} + \sum_{k=1}^{N} \frac{\eta_k}{\theta_k} C_{xx,k} \tag{5.25a}$$

$$\tau_{yy} = \eta_0 s 2 \frac{\partial v}{\partial y} + \sum_{k=1}^{N} \frac{\eta_k}{\theta_k} C_{yy,k} \tag{5.25b}$$

$$\tau_{xy} = \eta_0 s\left(\frac{\partial u}{\partial y} + \frac{\partial v}{\partial x}\right) + \sum_{k=1}^{N} \frac{\eta_k}{\theta_k} C_{xy,k} \tag{5.25c}$$

$$\tau_{zz} = \sum_{k=1}^{N} \frac{\eta_k}{\theta_k} \tag{5.25d}$$

and

$$u\frac{\partial C_{xx,k}}{\partial x} + v\frac{\partial C_{xx,k}}{\partial y} - 2\left(\frac{\partial u}{\partial x}C_{xx,k} + \frac{\partial u}{\partial y}C_{xy,k}\right) + \frac{1}{2\theta_k}(C^2_{xx,k} + C^2_{xy,k} - 1) = 0 \qquad (5.26a)$$

$$u\frac{\partial C_{yy,k}}{\partial x} + v\frac{\partial C_{yy,k}}{\partial y} - 2\left(\frac{\partial v}{\partial y}C_{yy,k} + \frac{\partial v}{\partial x}C_{xy,k}\right) + \frac{1}{2\theta_k}(C^2_{yy,k} + C^2_{xy,k} - 1) = 0, \qquad (5.26b)$$

$$u\frac{\partial C_{xy,k}}{\partial x} + v\frac{\partial C_{xy,k}}{\partial y} - \left(\frac{\partial v}{\partial x}C_{xx,k} + \frac{\partial u}{\partial y}C_{yy,k}\right) + \frac{1}{2\theta_k}C_{xy,k}(C_{xx,k} + C_{yy,k}) = 0 \qquad (5.26c)$$

The boundary conditions associated with the above equations for the fountain flow problem were described in Section 3.2.1 for viscous flows. In the present viscoelastic case the components of the elastic strain tensor C_k must also be specified at a portion of the flow boundary crossed by the streamlines (AD in Figure 3.3).

The above system of equations is solved numerically with a mixed Finite Element formulation to obtain the velocity and stress fields and the free surface shape. Recent reviews for the numerical simulation of viscoelastic flows can be found in Crochet et al (1984) and Keunings (1987).

The finite element approximation to the velocity, pressure and elastic strain tensor is:

$$V = \sum_i V^i \phi^i(\xi, \eta), \qquad P = \sum_i P^i \pi^i(\xi, \eta), \qquad C_{k,} = \sum_i C^i_k \phi^i(\xi, \eta) \qquad (5.27)$$

where V^i, P^i and C^i_k are nodal variables and $\phi^i(\xi,\eta)$, $\pi^i(\xi,\eta)$ are the associated basis functions. Elements used in this work are the 9-node quadrilateral and 6-node triangular isoparametric elements (see appendix A) with C^0-P^2 approximation for velocity and elastic strain tensor and C^0-P^1 for pressure.

The Galerkin principle is invoked to obtain the weak form of the governing equations. Following standard procedures within the Galerkin Finite Element framework we arrive at the following form of momentum, continuity, constitutive equation and free surface residuals associated with velocity, pressure, elastic strain and free surface unknowns

respectively:

$$R^i_m = \int_\Omega \nabla \phi^i \cdot \sigma \, d\Omega - \int_{\partial\Omega} n \cdot \sigma \, \phi^{i'} d\ell = 0 \qquad (5.28a)$$

$$R^i_c = \int_\Omega \nabla \cdot V n^i \, d\Omega = 0 \qquad (5.28b)$$

$$R^i_{CE} = \int_\Omega \left[\overset{\nabla}{C}_k + \frac{1}{2\theta_k}(C_k \cdot C_k - I) \right] \phi^i \, d\Omega = 0 \qquad (5.28c)$$

$$R^i_k = \int_{F.S.} n \cdot V \bar{\phi}^i(\xi, \eta = 1) d\ell = 0 \qquad (5.28d)$$

$$R^i_\delta = \int_{-1}^0 (x_\xi^2 + y_\xi^2)^{1/2} \bigg|_{\eta=1} d\xi - \int_0^1 (x_\xi^2 + y_\xi^2)^{1/2} \bigg|_{\eta=1} d\xi = 0 \qquad (5.28e)$$

The above formulation, eqs. (5.28a-e) is similar to the u-v-p-h-δ formulation of Section 3.2.2 (also appendix A), except for the presence of the elastic strain unknowns associated with the viscoelasticity of the fluid. The momentum, continuity and free surface equations are treated in exactly the same way. The explicit form of the weighted residual equations and Jacobian entries for the viscoelastic case can easily be derived by following the procedure outlined in appendix A for the viscous case. Note the increased number of unknowns in the viscoelastic case. For every mode in the Leonov model there are three elastic strain components ($C_{xx,k}$, $C_{yy,k}$, $C_{xy,k}$) and typically two modes are required (N=2) to describe rheologically a given polymer melt. For the 9-node quadrilateral element and for a 2-mode Leonov model the degrees of freedom at the element level are:

9   x-velocity components

9   y-velocity components

4   pressure variables (at nodes 1,3,5,7)

3   h-variables (at nodes 5,6,7)

1	δ-variable (at node 6)
$9 \times 2 = 18$	$C_{xx,k}$ variables
$9 \times 2 = 18$	$C_{yy,k}$ variables
$9 \times 2 = 18$	$C_{xy,k}$ variables

Total = 80 variables per 9-node element

Hence, at the element level we have 80 variables and an 80x80 element Jacobian matrix, as compared to 26 variables and an 26×26 element Jacobian for the viscous case. It is obvious that the computational cost increases by an order of magnitude in the viscoelastic case. Note also that the increased nonlinearity and intricacy of the viscoelastic problem requires special iteration and continuation procedures. These are discussed below.

When the residuals, eqs. (5.28), are applied at the nodes of the discretized flow domain along with the appropriate boundary conditions they provide as many algebraic equations as there are nodal unknowns. Let X be the vector of unknowns and R be the vector of residuals. For given rheological properties and for the present problem, there is only one independent parameter. A convenient choice is the shear rate at the wall or equivalently the U/H ratio (1/3 of the apparent shear rate). Let p denote the U/H ratio:

$$p = U/H \tag{5.29}$$

For a given value of p the algebraic system to be solved is:

$$R(X ; p) = 0 \tag{5.30}$$

We distinguish the following cases:

Case 1: there is no available solution in the neighborhood of p. Typically, this represents the first attempt to obtain a solution on a given mesh. In this case a preliminary iteration is performed to obtain the Newtonian velocity and pressure fields (the elastic strain and free surface unknowns are held fixed). On the basis of the Newtonian velocity field an initial approximation to the elastic strain tensor is given by (Upadhyay & Isayev, 1986):

$$C_k = I + \theta_k(\nabla V + \nabla V^T) \tag{5.31}$$

A few additional start-up iterations (usually 2 or 3) are performed to improve the initial solution estimate (free surface variables are still fixed). With an adequate initial solution estimate flow available, a full Newton-Raphson iteration with line searches (Engelman et al, 1981; Karagiannis et al, 1988) is performed on eq. (5.30):

$$J^{(m)}d^{(m)} = -R^{(m)} \tag{5.32a}$$

$$X^{(m+1)} = X^{(m)} + \alpha d^{(m)} \tag{5.32b}$$

where $J = \partial R/\partial X$, is the Jacobian of the global system. The parameter α is used to modify the step length in eq. (5.32b) with a line search, to minimize the sum of residuals along the search direction $d^{(m)}$, if necessary (Karagiannis et al.,1988). For $\alpha=1$ we recover the ordinary Newton-Raphson algorithm. The line search increases considerably the radius of convergence of the original Newton-Raphson scheme.

Case 2: there are N_p available solutions X_j at parameter values (p_j, $j=1,N_p$) in the neighborhood of p (usually 2 or 3). Then an initial estimate $X^{(0)}$ at p is obtained by continuation using Lagrangian polynomials, i.e.:

$$X^{(0)} = \sum_{j=1}^{N_p} \ell_j(p)X_j \tag{5.33}$$

where

$$\ell_j(p) = \prod_{\substack{i=1 \\ i \neq j}}^{N_p} \frac{p-p_i}{p_j-p_i} \tag{5.34}$$

With $X^{(0)}$ providing the initial estimate, the Newton-Raphson iteration, eqs. (5.32), is then employed to obtain the solution. Equations (5.33) and (5.34) offer a computationally cheap method of continuation in the parameter p. For $N_p=2$ we have the discrete analog of first

order continuation (Brown et al,1980), while for $N_p>2$ we obtain higher order (and more efficient) continuation. It is possible to employ an adaptive continuation scheme in which the increments in the parameter p are determined by means similar to the time step-size control of Section 4.2.3 (Khesghi et al,1983). However, such an approach was not necessary for the problems studied.

In both Cases 1 & 2 the solution at the given parameter value is determined with the Newton-Raphson iteration. In addition to the fast convergence that characterizes this iterative technique, availability of the Jacobian brings other benefits in identifying irregular points that are sometimes encountered in the simulation of viscoelastic flows; at an irregular point of the parameter space (here the one-dimensional space of the parameter p=U/H) where the solution family either varies infinitely rapidly, terminates abruptly, bifurcates, or turns on itself, the linearization, eq. (5.32a), of eq. (5.30) fails and the Jacobian matrix is singular. This gives us the means to detect irregular points unambiguously by monitoring changes of sign of the determinant of the Jacobian matrix as we compute the solution family (the determinant is simply the product of pivots computed during the Gaussian elimination).

5.2.4   Fountain Flow Simulations

The previously described algorithm was employed to investigate the steady, isothermal fountain flow of a commercial polystyrene STYRON 678 U (Dow Chemical). The Leonov model parameters for this material are given in Table 5.1.

The WLF temperature-shift factor (Ferry, 1970) was used to evaluate η_k, θ_k at other temperatures, i.e.

$$\eta_k(T) = \eta_k(T_0) a_T/a_{T_0} \, , \quad \theta_k(T) = \theta_k(T_0) a_T/a_{T_0} \qquad (5.35)$$

$$a_T = \begin{cases} a_{T_g} \, , & \text{if } T \leq T_g \\[2mm] \exp\left[-\dfrac{C_1(T - T_{ref})}{C_2 + T - T_{ref}} \right] , & \text{if } T > T_g \end{cases} \qquad (5.36)$$

Two representative sets of processing conditions were selected from the literature and are given in Table 5.2. The material parameters were evaluated at the injection temperature for each set and the corresponding Leonov model predictions for unidirectional shear flow are listed in Table 5.3. Two commonly used measures of elasticity are the stress ratio evaluated at the wall:

$$S_R = \left. \frac{\tau_{xx} - \tau_{yy}}{2|\tau_{xy}|} \right|_{wall} \qquad (5.37)$$

and the Weissenberg number:

$$Ws = \theta_{avg} \dot{\gamma}_w \qquad (5.38)$$

where

$$\theta_{avg} = \sum_{k=1}^{N} \frac{\eta_k}{\eta_0} \theta_k \, , \qquad \dot{\gamma}_w = \left. \left| \frac{du}{dy} \right| \right|_{wall} \qquad (5.39)$$

The values of S_R and Ws given in Table 5.3 indicate a highly elastic fluid. Table 5.3 shows the effect of a slip boundary condition on the flow characteristics at the dimensionless slip number of $B = 10^{-2}$ ($B = \eta_0\beta/H$, see Section 3.2.3.2). At this level of slip the gapwise velocity and stress profiles, as predicted by the Leonov model, are affected by less than 1%. However, application of the slip boundary condition is crucial for the success of the finite element algorithm.

Three successively refined meshes were used in the fountain flow studies. The three meshes are plotted in Figure 5.5 and their characteristics are listed in Table 5.4. For clarity only part of each mesh is plotted (up to $x/H = -5$). The actual mesh extends up to

Table 5.2 Processing Conditions and Mold Dimensions

Set No.	U (m/s)	T_i (°C)	T_w (°C)	H (mm)	L (m)	W (m)	Reference
1	0.36	224	40	1.905	0.456	0.0762	Isayev (1983)
2	0.141	218	35	0.9	0.127	0.0635	Kamal&Tan (1979)

Table 5.3 Flow Characteristics of cases studied

Set No.	T_i (°C)	$\dot{\gamma}_w$ (s⁻¹)	τ_w (kPa)	S_R	Ws	
1	224	927.70	57.74	2.095	56.55	No Slip, B = 0
2	218	810.85	60.91	2.284	70.09	
1	224	922.13	57.65	2.090	56.20	With Slip, B = 0.01
2	218	806.62	60.83	2.279	69.72	

Table 5.4 Characteristics of finite element meshes

	Elements	Nodes	Unknowns	CPU sec / iteration	
				VAX 8600	CRAY X-MP/22
Mesh 1	60	261	2126	155	—
Mesh 2	120	519	4229	325	25
Mesh 3	296	1242	10162	—	90
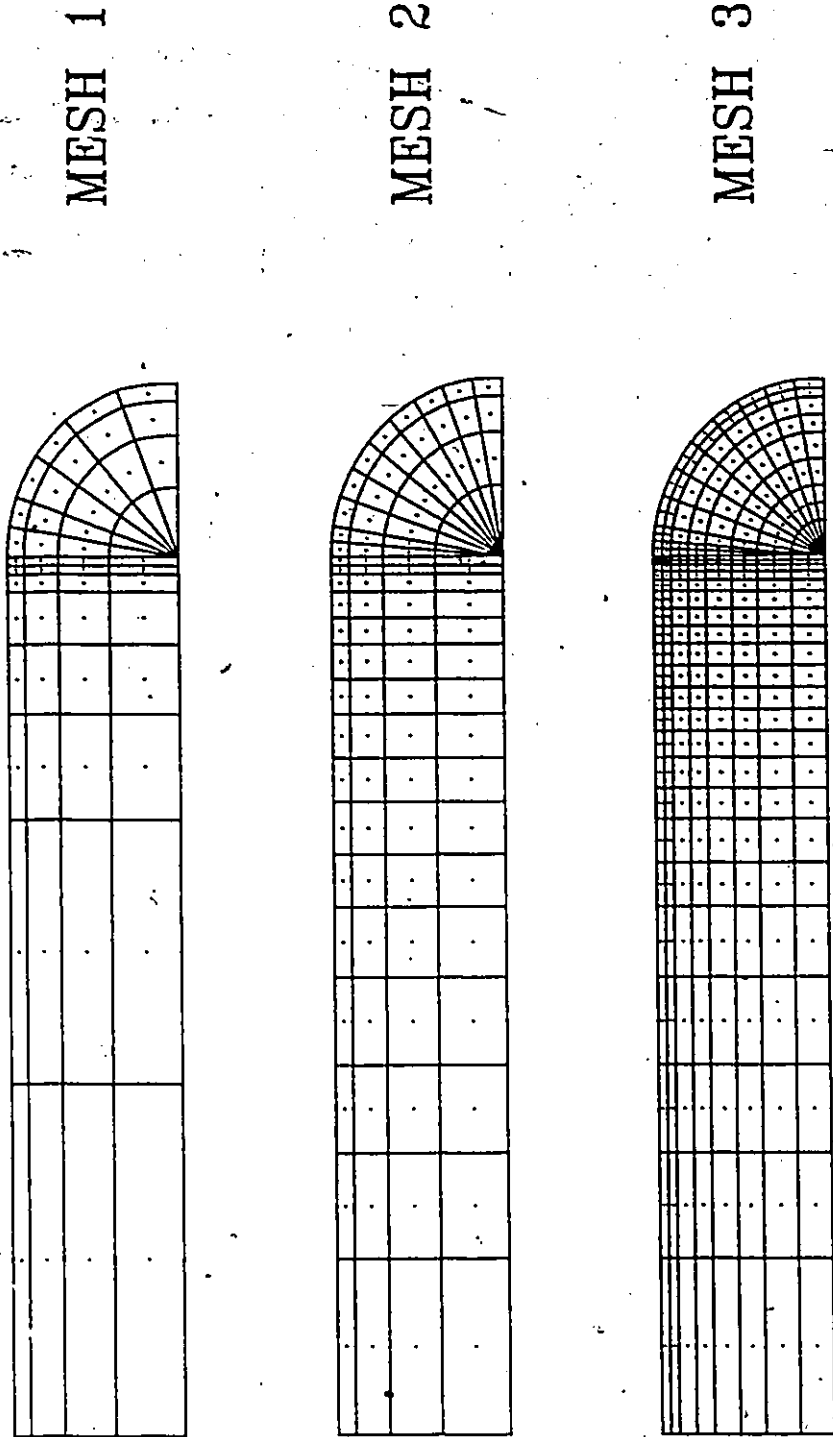
MESH 1

MESH 2

MESH 3

Figure 5.5   Finite element meshes for viscoelastic fountain flow

$x/H = -10$ for Mesh 1 and $x/H = -20$ for Mesh 2 and Mesh 3, where $x/H = 0$ is the contact line position, i.e. the flow front/wall intersection.

For every mesh the Newtonian solution was obtained first. Then the viscoelastic solution at the desired shear rate was obtained by successively incrementing the shear rate. The Newton-Raphson iterative scheme was employed to solve the finite element set of equations at every intermediate shear rate, as described in the previous section. Three to four shear rate increments were sufficient for the conditions of Table 5.3. Convergence was reached in 4-5 Newton-Raphson iterations (convergence criterion: maximum residual and maximum relative update below 10^{-8}). The strict termination criterion for Newton-Raphson iteration was imposed in order to achieve quadratic convergence which occurs asymptotically near regular points of the solution.

The mesh refinement study, with and without the slip boundary condition, was undertaken in anticipation of the "High Weissenberg Number Problem" (HWNP, Keunings, 1986b). This problem arises in the numerical simulation of viscoelastic flows in complex geometries and manifests itself as an inability to obtain a solution beyond some critical level of elasticity. When there is a stress singularity for the corresponding Newtonian flow problem (in the fountain flow problem stresses are singular at the contact line), viscoelastic computations always exhibit a limit point (limiting level of elasticity) beyond which convergence is lost, and this limit point decreases with mesh refinement. As a possible remedy to the HWNP, within the context of continuum theory, Lipscomb et al (1987) suggested relaxing the no-slip condition to alleviate the stress singularities. The results of the present work lend further support to this suggestion.

Computations with Mesh 1 and the no-slip condition $(B=0)$ allowed the high elasticity levels of Table 5.3 to be reached with no difficulty. When using the denser Mesh 2, problems arose at a stress ratio value of about 2.2. Despite all efforts (small shear rate

increments, higher order continuation) the Newton-Raphson iterative scheme was unable to converge: the sign of the determinant of the Jacobian matrix oscillated during the unsuccessful iterations indicating the presence of an irregular point.

The slip boundary condition was then used and calculations were repeated with $B = 10^{-2}$. For this level of slip the Newton-Raphson iterative scheme converged quadratically for the conditions of Table 5.3 and for all three meshes. Comparison of the converged solutions for Mesh 1 with and without slip ($B = 0$ and $B = 10^{-2}$) showed that the results were practically unchanged. This indicates that the main effect of slip is localized in the contact line region, where it removes the singular stresses that become more pronounced with mesh refinement and cause loss of convergence of the algorithm.

A representative plot for the behavior of the computed velocity, stress and free surface degrees of freedom with mesh refinement is given in Figure 5.6, which shows the axial velocity along the centerline (Figure 5.6a), the gapwise profile of the first normal stress difference at $x/H = 0$ (Figure 5.6b) and the flow front shape (Figure 5.6c). The close agreement of the results with the three meshes shows that a sufficient accuracy has been reached at this level of mesh refinement. Due to the high cost involved in the computations, and in view of the present results no further numerical tests were undertaken with denser meshes or higher levels of elasticity.

The streamlines for the conditions of set 2 in Table 5.3 are shown in the lower half of Figure 5.7. The effect of fountain flow on the deformation experienced by the fluid is shown as the series of fluid element shapes in the upper half of Figure 5.7. These shapes were obtained by tracking a large number of material points along the surface of an initially rect-angular element, as described in Chapter 3. It is shown that as the fluid element decelerates near the flow front it is stretched initially in the transverse direction. The element continues to deform as it moves away from the centerline towards the wall following the flow front
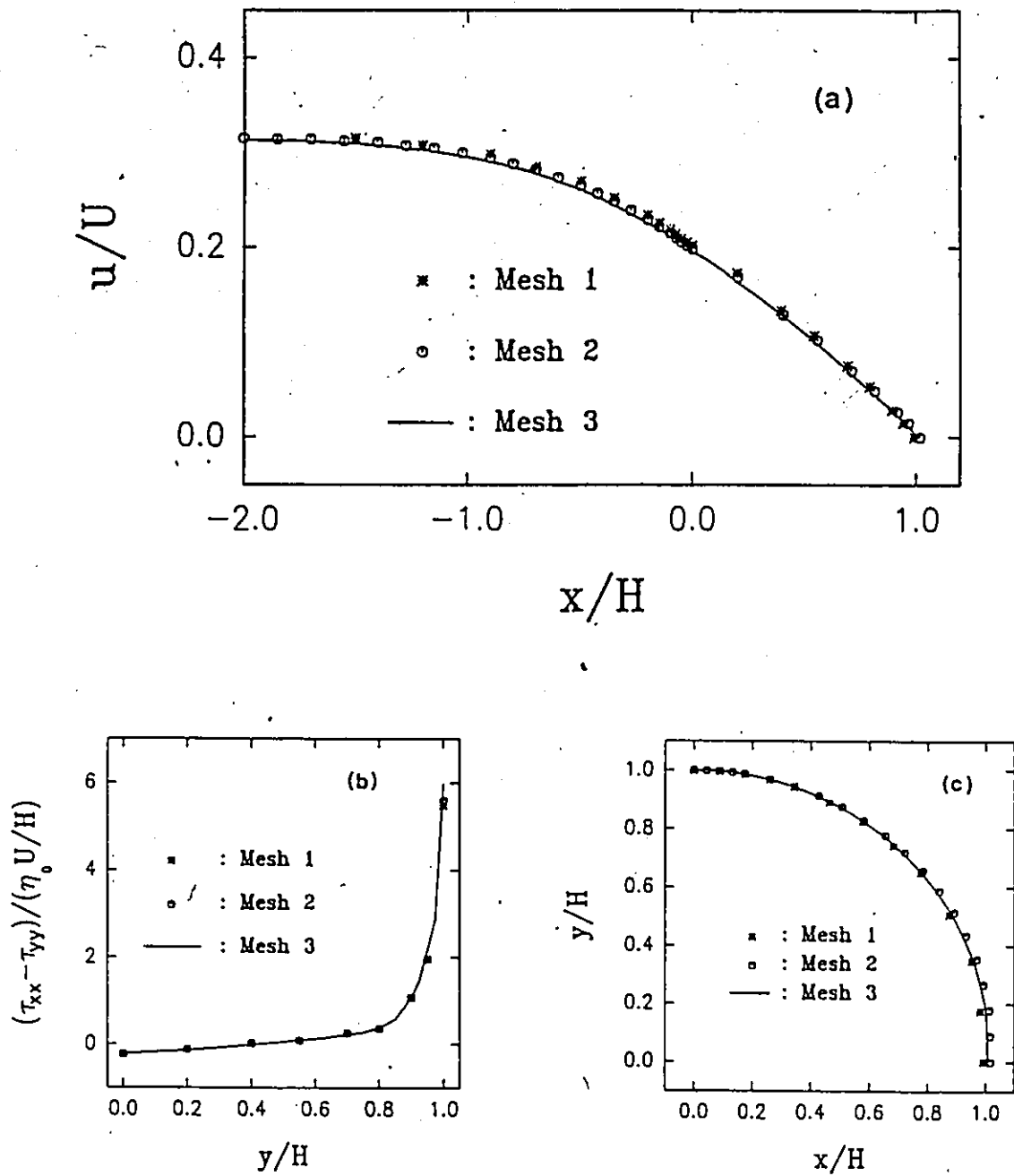
Figure 5.6   Results obtained with the three meshes (parameters of set 2 in Table 5.3,
              B = 0.01):
              (a) velocity variation along the centerline
              (b) profile of first normal stress difference behind the flow front (x/H = 0)
              (c) flow front shape
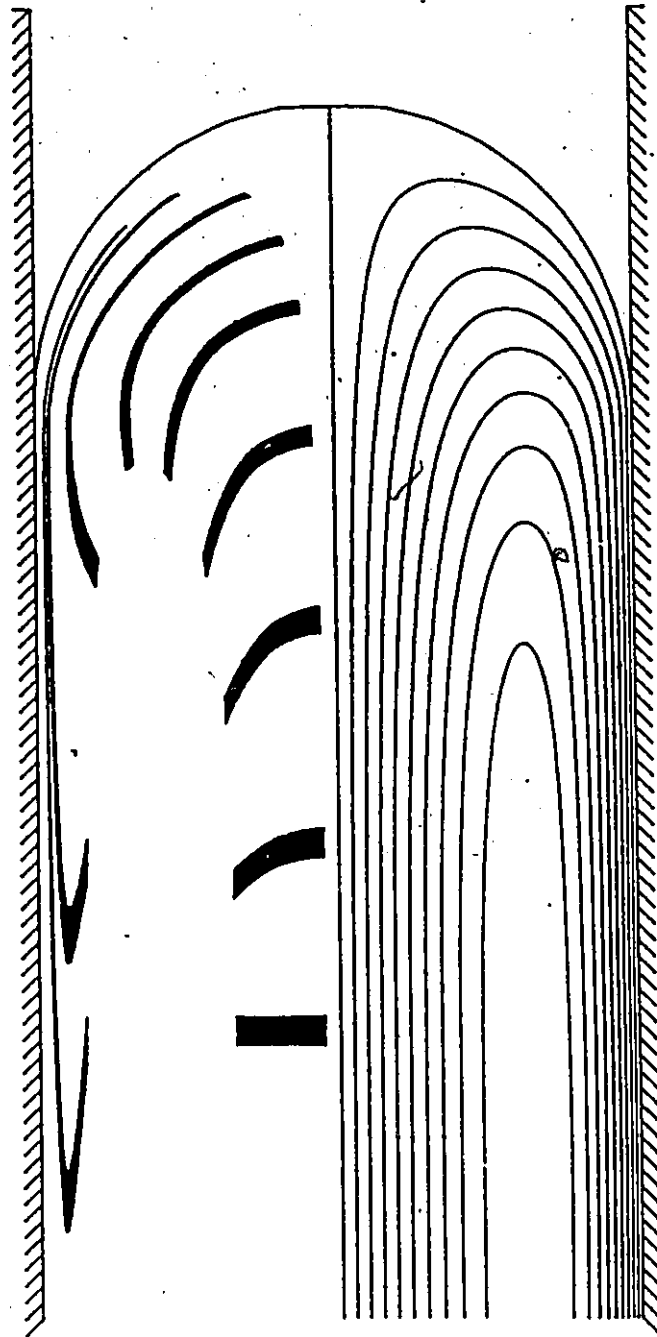
Figure 5.7   Streamlines and deformation of a fluid element (parameters of set 2 in Table 5.3, B = 0.01)
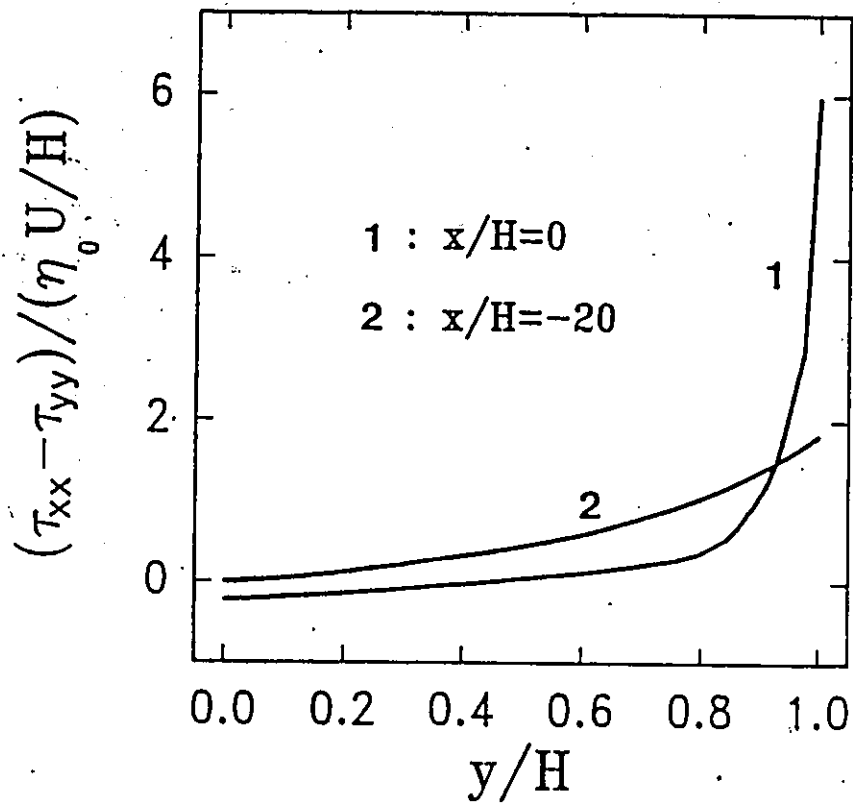
Figure 5.8   Comparison of first normal stress difference profiles behind the flow front
              (x/H=0, curve 1) and in-the fully developed flow region (x/H = −20, curve 2).
              Parameters as in Figure 5.7

shape in a curved path. When the fluid element reaches the wall it is extremely stretched and oriented in the flow direction, while its trailing edge forms a V-shape. The deformation pattern is the same as that obtained in Section 3.3 with a Newtonian constitutive equation. There were no essential differences between the fluid element shapes determined with the Newtonian and the viscoelastic velocity field. This is because the kinematics of fountain flow is not affected qualitatively by the viscoelastic character of the fluid. However, it would be expected that the dynamics of the flow is different in the viscoelastic case. Shown in Figure 5.8 is a comparison of the gapwise profiles of the first normal stress difference behind the flow front ($x/H = 0$, curve 1) and in the fully developed flow region ($x/H = -20$, curve 2). For curve 1, it is noted that the first normal stress difference is negative near the centerline corresponding to the initial compression of the fluid element in Figure 5.7, and very large and positive near the wall corresponding to the extreme extension of the fluid elements in this region as illustrated in Figure 5.7. These extended fluid elements form the solidified surface layer in injection molding. The deformation of the elements in Figure 5.7 or equivalently the high stress levels of curve 1 in Figure 5.8 can explain the increasing birefringence of the surface layer in injection molded articles (part BA in Figure 5.2). A quantitative description of this phenomenon is considered below.

5.3   Prediction of flow-induced frozen-in stresses

5.3.1   A simplified theory

Rigorous prediction of frozen-in stresses in injection molded parts requires the solution of the fully two-dimensional, transient and non-isothermal mold filling and the subsequent stress relaxation. Although this problem does not involve new principles and can be solved with currently available numerical techniques, it would require enormous computer resources. It appears, however, that reasonable approximations can be made that simplify

the numerical problem considerably. The first approximation is related to the fluid mechanics of mold filling. Clearly, it is not practical to consider the full two-dimensional problem in both the flow and thickness directions. Since the aspect ratio of the molds is usually very high ($H/L << 1$) and the fountain flow region extends only a small distance behind the advancing front (see Chapter 3), the flow can be modelled as a locally unidirectional shear flow for the majority of the mold (lubrication-like approximation).

The second approximation is related to the heat transfer of the process. The heat transfer problem has been discussed extensively by Janeschitz-Kriegl (1977,1979,1983). The dominant heat transfer mechanisms are convection in the flow direction and conduction in the thickness direction. Heat convection prevails near the gate while heat conduction is dominant behind the flow front (Janeschitz-Kriegl, 1983). Since we are mainly interested in the development of the solidified layer behind the advancing flow front, we neglect heat convection in the flow direction. Then the problem reduces to transient heat conduction in the thickness direction.

Isayev & Hieber (1980) developed a theory with the above assumptions for the prediction of frozen-in stresses in injection molding. The mathematical model involves the equations describing transient nonisothermal shear flow, i.e.

Momentum:
$$-\frac{dP}{dx} + \frac{d}{dy}(\tau_{xy}) = 0 \quad \text{or} \quad \tau_{xy} = y\,\frac{dP}{dx} \tag{5.40}$$

Continuity:
$$\int_0^H u\,dy = UH \quad \text{or} \quad \int_0^H y\dot{\gamma}\,dy + UH = 0 \tag{5.41}$$

Energy:
$$\frac{\partial T}{\partial t} = a\,\frac{\partial^2 T}{\partial y^2} \tag{5.42}$$

Constitutive model:

$$
\begin{bmatrix} \tau_{xx} & \tau_{xy} & 0 \\ & \tau_{yy} & 0 \\ \text{symm.} & & \tau_{zz} \end{bmatrix} = s\eta_0 \begin{bmatrix} 0 & \dot{\gamma} & 0 \\ & 0 & 0 \\ \text{symm.} & & 0 \end{bmatrix} + \sum_{k=1}^{N} \frac{\eta_k}{\theta_k} \begin{bmatrix} C_{xx,k} & C_{xy,k} & 0 \\ & C_{yy,k} & 0 \\ \text{symm.} & & 1 \end{bmatrix} \qquad (5.43)
$$

$$
C_{xx,k} C_{yy,k} - C_{xy,k}^2 = 1 \qquad (5.44a)
$$

$$
\frac{d\,C_{xx,k}}{dt} - 2\dot{\gamma}\,C_{xy,k} + \frac{1}{2\theta_k}(C_{xx,y}^2 + C_{xy,k}^2 - 1) = 0 \qquad (5.44b)
$$

$$
\frac{d\,C_{xy,k}}{dt} - \dot{\gamma}\,C_{yy,k} + \frac{1}{2\theta_k}C_{xy,k}(C_{xy,k} + C_{yy,k}) = 0 \qquad (5.44c)
$$

where $\dot{\gamma} = du/dy$ is the shear rate, a is the thermal diffusivity and η_0, η_k, θ_k are temperature dependent (eq. (5.35)). The above system of algebraic and parabolic differential equations describes the pressure gradient (dP/dx) and the gapwise profiles of temperature (T), shear rate ($\dot{\gamma}$) and the components of the elastic strain tensor ($C_{xx,k}, C_{yy,k}, C_{xy,k}$). The initial and boundary conditions for the temperature are:

$$
t=0: \quad T=T_i, \qquad 0 \le y \le H \qquad (5.45a)
$$

$$
t>0: \quad \partial T/\partial y = 0 \text{ at } y=0 \quad \text{and} \quad T=T_w \text{ at } y=H \qquad (5.45b)
$$

Initial conditions must also be specified for the components of the elastic strain tensor. Isayev & Hieber (1980) used the steady-state solution of eq. (5.44) (given in eq. (5.18)), therefore neglecting any effect of fountain flow.

The above equations were solved as follows:

(i)   The half-gapwidth $0 \le y \le H$ is discretized into M one-dimensional 3-node line elements. There are 2M + 1 nodal points y_i, $y_1 = 0$, $y_{2M+1} = H$.

(ii)   The degrees of freedom at the nodal points are: temperature (T), shear rate ($\dot{\gamma}$), and the components of the elastic strain tensor (6 components in the present case of a 2-

mode Leonov fluid). Finally, there is a pressure gradient (dP/dx) degree of freedom. Thus, the total number of unknowns is $8(2M+1)+1$.

(iii)   A Galerkin/Finite Element formulation reduces the energy partial differential equation, eq. (5.42), into a first order ordinary differential equation (ODE) with respect to time. Applying this to every nodal point gives $(2M+1)$ ODE's for the temperature. Applying eq. (5.40) and eqs. (5.44) at the nodal points provides as many algebraic and ordinary differential equations as there are nodal shear rate and elastic strain unknowns. Finally, the continuity equation, eq. (5.41), provides an additional algebraic equation associated with the pressure gradient.

(iv)   We have now a coupled system of algebraic and first order ordinary differential equations. This is integrated in time using the predictor-corrector scheme of Section 4.2.3.

For a given set of processing conditions, the algorithm to predict the flow-induced frozen-in stresses and birefringence at a location X from the gate of a mold with length L, is as follows:

(i)   <u>mold filling phase</u>: the system of eqs. (5.40-5.44) is integrated up to time $t_{fill}=(L-X)/U$.

(ii)   <u>stress relaxation phase</u>: at $t=t_{fill}$ the flow is assumed to stop abruptly. The shear rate is set to zero and integration is continued until the maximum temperature (at the centerline) drops below the glass transition temperature T_g.

At every instant the stresses are calculated from eq. (5.43) and the birefringence Δn from eq. (5.2).

5.3.2   Results and Discussion

Typical predictions of the theory of Isayev & Hieber (1980) are shown in Figures 5.9 and 5.10, for the conditions of set 1 in Table 5.2, and at a distance $X=0.057$ m from the gate. Figure 5.9 corresponds to the predictions of eqs. (5.40-5.44) during the mold filling phase. The initial temperature is $T_i=224°C$, while the wall is at $T_w=40°C$ and the solidification (glass transition) temperature is $T_g=100°C$. Consequently, a solidified layer begins growing from the wall towards the center, as can be observed in Figure 5.9a by noting the y/H position at which $T=100°C$ for the various temperature curves. Associated with these developments are the changes in the velocity and shear rate profiles shown in Figures 5.9b and 5.9c respectively. The velocity decreases with time in the vicinity of the cold wall. Accordingly, the flow rate increases in the hot region in order to maintain a constant flow rate. The velocity profile is a bell-shaped curve characteristic of this type of non-isothermal flow (with a temperature dependent viscosity) and the shear rate profile exhibits a maximum (corresponding to the inflection point of the velocity curve) which shifts inward as time increases.

The shear stress profiles are plotted in Figure 5.9d and show a linear variation, which follows from a well-known balance of forces. The shear stress continues to increase into the solidified layer and up to the wall. However, it must be pointed out the stress that develops into the solidified layer (i.e. after the temperature has dropped below $T_g=100°C$) does not contribute to the final flow birefringence, i.e. it is not frozen-in.

The profiles of the first normal stress difference are shown in Figure 5.9e. The normal stress is frozen near the wall and displays an intermediate maximum which increases and shifts inward with time, due to the growth of the solidified layer. Comparison of the normal stress and shear stress levels in Figures 5.9d and 5.9e shows that the normal stress is larger and therefore forms the dominant term to the flow birefringence (see eq. (5.2)).

Figure 5.9   Evolution of the profiles of (a) temperature, (b) velocity, (c) shear rate, (d) shear stress, (e) first normal stress difference, and (f) birefringence, during the mold filling phase. Parameters of set 1 in Table 5.2, X = 0.057 m from gate
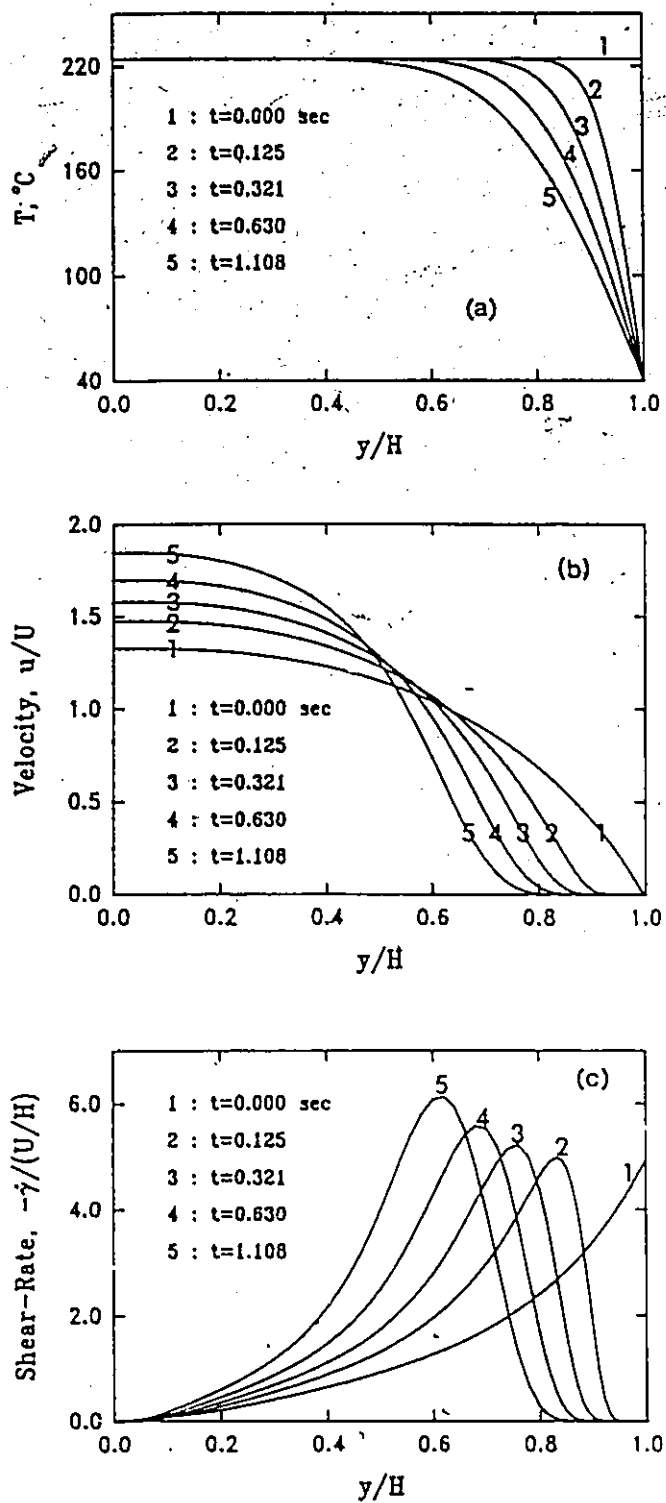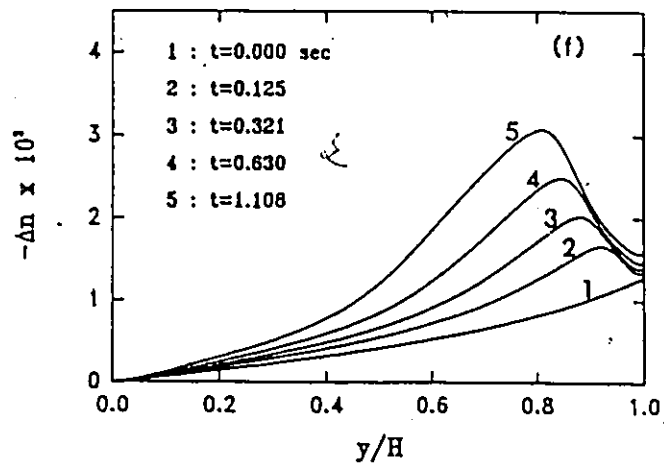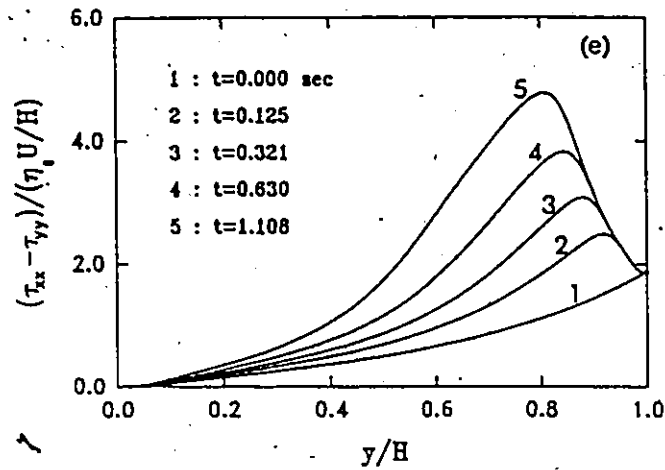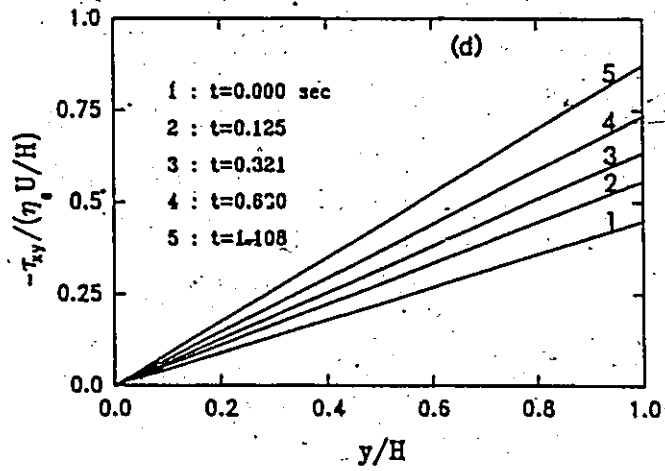
Figure 5.9   (continued)
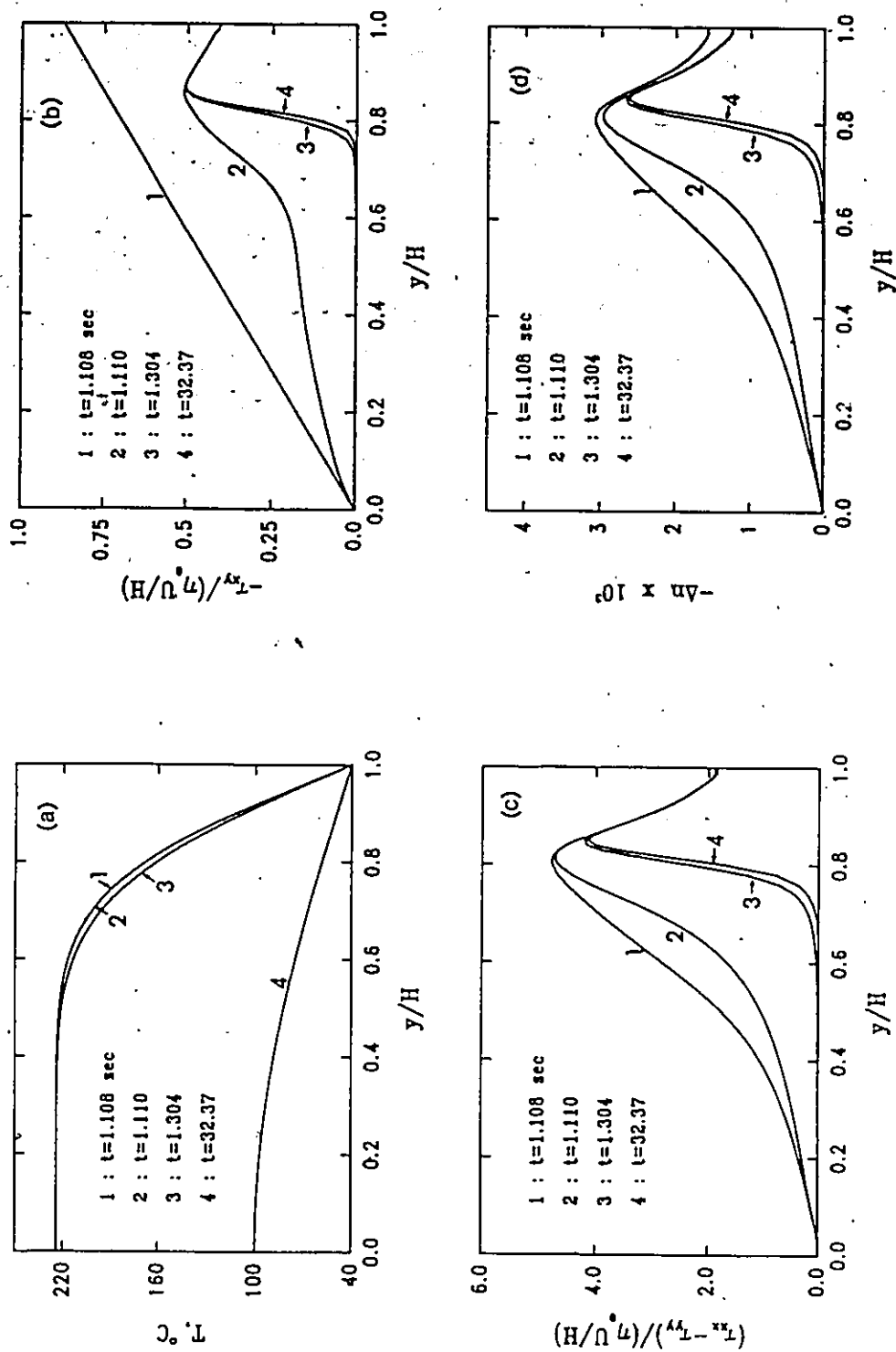
Figure 5.10   Evolution of the profiles of (a) temperature, (b) shear stress, (c) first normal stress difference, and (d) birefringence, during the stress relaxation hase. Parameters as in Figure 5.9

Correspondingly, the Δn profile shown in Figure 5.9f follows the shape of the normal stress profile.

At $t_{fill} = (L-X)/U = 1.108$ seconds the flow front covers the distance from the position X to end the mold L, travelling with average velocity U. The flow is assumed to stop abruptly at $t = t_{fill}$, and the stress relaxation phase begins. The predictions for temperature, shear stress, first normal stress difference and birefringence are shown in Figure 5.10a,b,c,d. When the temperature at a particular point drops below $T_g = 100°C$ the stress is frozen-in and no further relaxation can take place. At the end of relaxation (i.e. when $T < T_g$ throughout the gap), the profiles are depicted by curve 4 in Figures 5.10, and show that complete relaxation has taken place in the region $0 \leq y/H \leq 0.65$.

The predictive capabilities of the above theory (notably the neglect of thermal stresses, packing pressure and fountain flow) have been discussed by Isayev & Hieber (1980) and Isayev (1983). We will consider here the effects of fountain flow.

As was discussed earlier the main effect of fountain flow is on the deformation of fluid elements as they pass through the flow front region directed towards the walls (Figure 5.7). The extreme extension of fluid elements near the wall in Figure 5.7 manifests itself dynamically as a large stress in that region. This is clearly shown by the first normal stress difference profile in Figure 5.8. These observations lead to an approximate way of incorporating the dynamics of fountain flow into the model for frozen-in stress prediction, eq. (5.40-5.44): instead of using as initial values, at $t = 0$, for the components of the elastic strain tensor in eq. (5.44), the fully-developed profiles given in eq. (5.18) (and which imply a prehistory of unidirectional shear flow), we assign as initial values the profiles computed numerically by the finite element solution of the fountain flow problem at $x/H = 0$, $0 \leq y \leq H$ (i.e., the profiles at the plane passing through the contact line). The theory of Isayev & Hieber (1980) was developed by idealizing the mold filling process as an isothermal shear flow at the
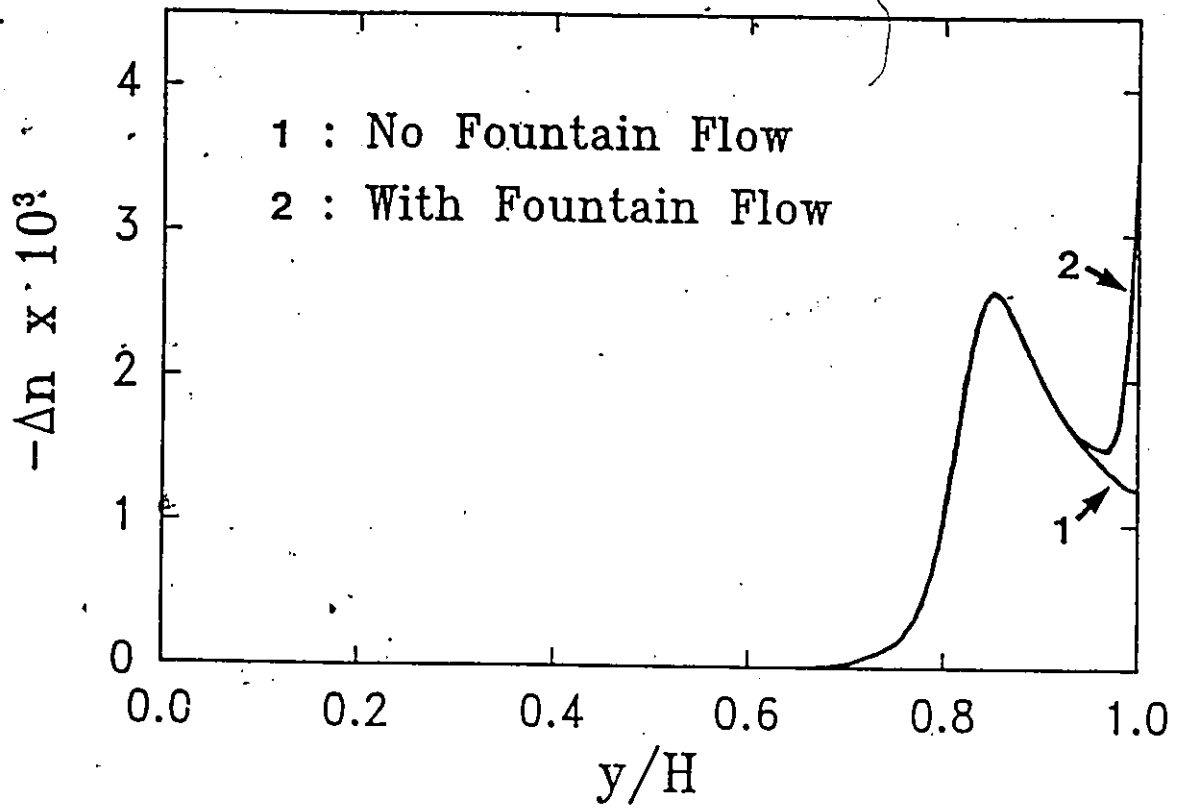
Figure 5.11   Comparison of frozen-in birefringence profiles with (curve 2) and without (curve 1) fountain flow taken into account (parameters as in Figure 5.9)

injection temperature at $t<0$, followed at $t=0$ by a sudden decrease of the wall temperature from T_i to T_w. The present modification can be viewed as an analogous idealization but with a prehistory of isothermal fountain flow at $t<0$, which only serves to offer the profiles of the elastic strain tensor components, to be used as initial conditions for the transient non-isothermal flow, eqs. (5.40-44) at $t>0$.

With the above modification calculations for the conditions of Figures 5.9 & 5.10 were repeated and are presented in Figure 5.11, which shows the profiles of the frozen-in flow birefringence with (curve 2) and without (curve 1) fountain flow taken into account. It is shown that by incorporating the effect of fountain flow the theory does predict the Δn minimum near the wall and the high birefringence at the surface.

Further comparison with published experiments is shown in Figure 5.12. The predictions follow correctly the trend depicted by the experimental data, although they generally underestimate the data. For the data of Isayev (1983) in Figure 5.12a it is shown that the position of the Δn maximum in the subsurface layer is well predicted but not its level. This is probably due to the neglect of the effect of packing pressure which was found (Isayev & Hariharan, 1985) to increase the height of the Δn maximum but not affect its position. For the data of Kamal & Tan (1979) in Figures 5.12b,c the predictions agree better with the experiments at the larger distance from the gate ($X=0.075$ m, Figure 5.12c). This is associated with the heat transfer model which is valid at large distances from the gate; the closer to the gate the more it overpredicts the frozen layer thickness and consequently underpredicts the y/H position of the Δn maximum as shown in Figure 5.12c.

In all cases of Figure 5.12 the predictions and the experimental data show a Δn minimum near the surface and an increasing birefringence between the position of the minimum and the wall. This minimum is created as follows: initially, the fountain flow results in a birefringence profile increasing near the wall (observe the first normal stress difference in
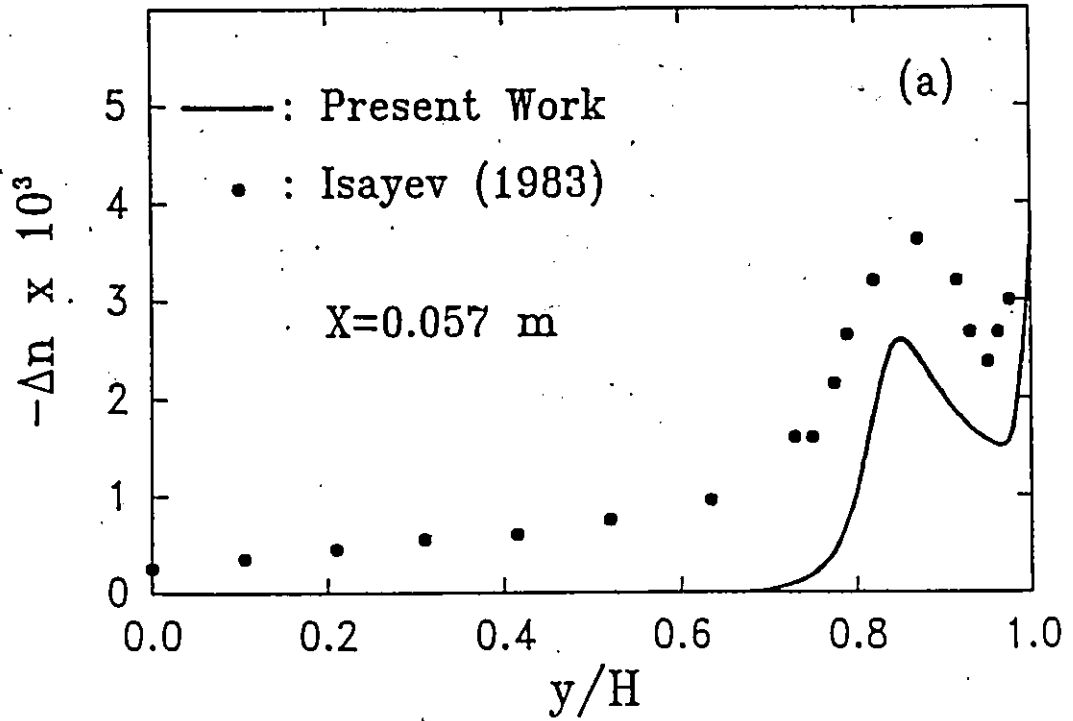
Figure 5.12   Comparison of experimental (symbols) and predicted (solid line) frozen-in birefringence profiles at the indicated distance X from the gate. Parameters of set 1 (Isayev, 1983) for (a), and set 2 (Kamal & Tan, 1979) for (b) and (c)
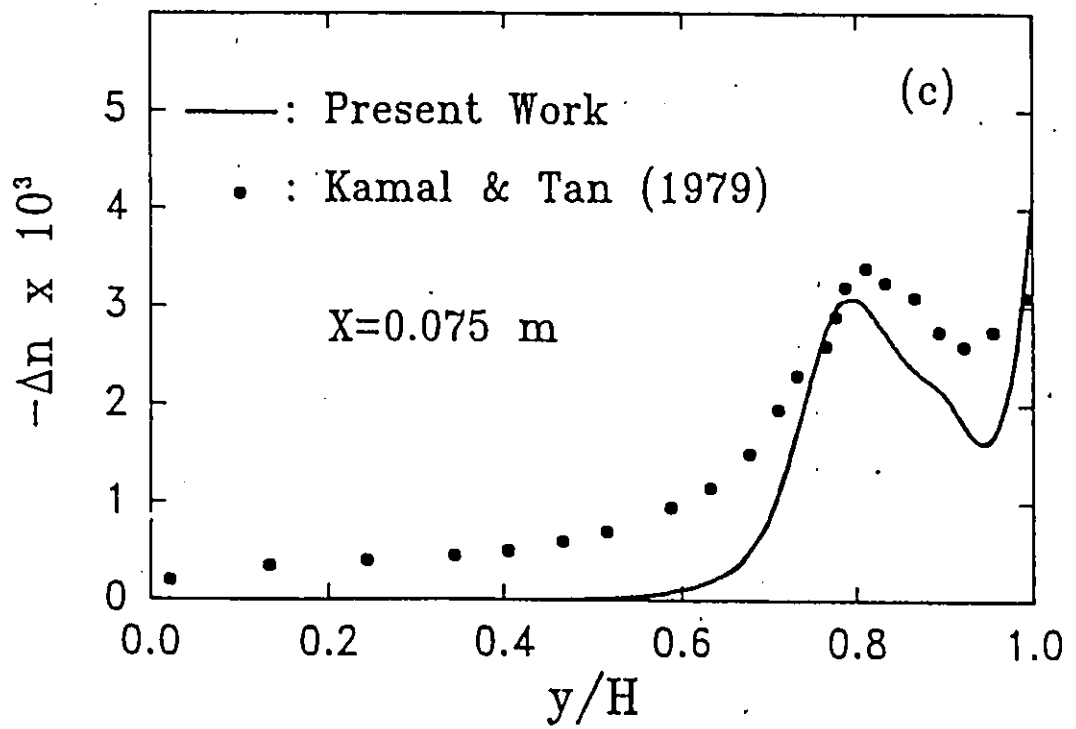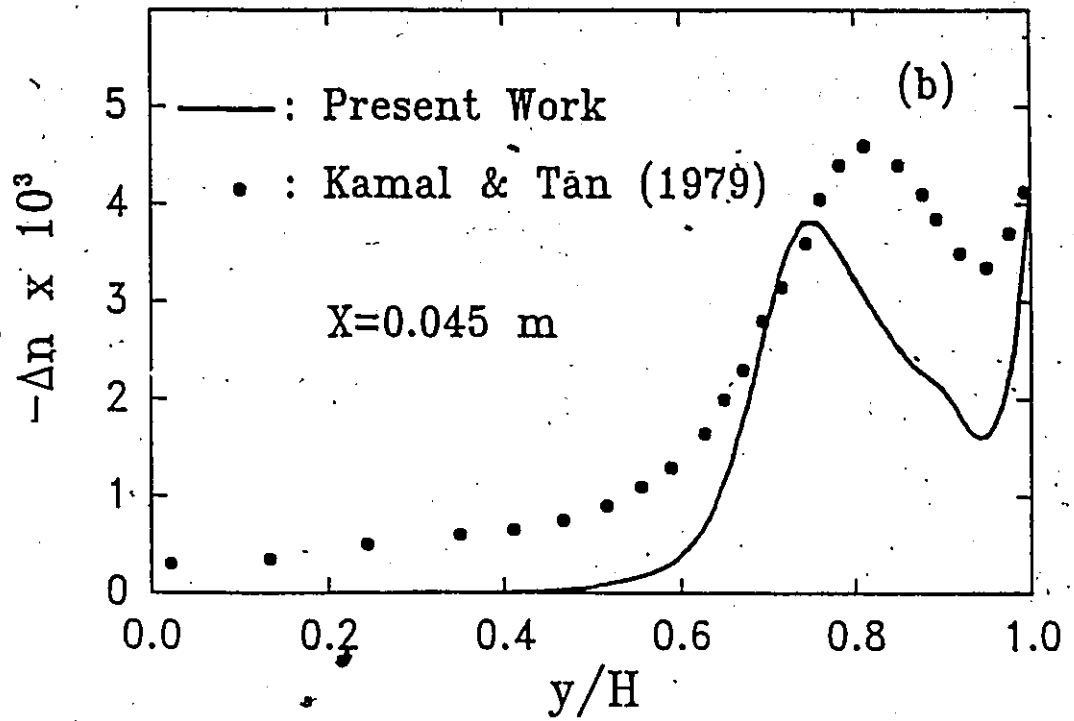
Figure 5.12   (continued)

the wall region in Figure 5.8) while the subsequent development of a solidified layer and the associated stress build-up causes a decreasing birefringence in the same region (Figure 5.10f). The composite effect is a birefringence profile that passes through a maximum and increases again near the surface. Thus the Δn minimum is established by the heat transfer behind the flow front and will therefore appear at the same y/H position for any distance X from the gate, as long as the heat transfer mechanism remains the same and there is sufficient time available for the solidified layer to develop. Kamal & Tan (1979) noted in their experiments that the position of the Δn minimum was nearly constant for all axial positions. For the conditions of set 2 in Table 5.2 the experimentally found position was y/H = 0.92–0.95. The predicted position in the present work (Figure 5.12b,c) was y/H = 0.94, in good agreement with the above experimental findings.

It is evident from the above simulations and experimental observations that the effect of fountain flow consists in the development of a highly oriented surface layer (part BA in Figure 5.2). The present calculations show that this layer extends from y/H = 0.94 to y/H = 1.0 for the conditions studied. It is interesting to note the actual dimensions of this layer: for the conditions of set 2 in Table 5.2 (H = 0.9 mm) the thickness of this layer is 54 microns (54×10^{-6} m). This is so small that sometimes it escapes the attention of experimentalists. Wales and co-workers did observe in their birefringence experiments a high orientation at the surface layer (see the discussion in Janeschitz-Kriegl (1979) and a photograph from Wales' experiments in Han (1976)) but they decided to neglect it, apparently as an artifact of the experimental technique, and did not report or mention it in Wales et al (1972). Isayev (1983) reported experimental birefringence profiles for thin and thick strips. For the thin strip (with thickness 2H = 2.54mm) the birefringence profile does not show the Δn minimum and the increasing birefringence at the surface (the profile for the thick strip is shown in Figure 5.12a). However, Isayev (1983) noted that "*within a distance* $\approx 7 \times 10^{-5}$

meters from the surface, difficulties arose in the birefringence Δn measurement caused by problems in distinguishing isochromatic patterns. Apparently, a surface layer is present in the thin strip which has even a higher orientation than the thick strip" and cited the fountain effect as a possible cause. The present calculations show that the fountain effect is indeed the origin of the orientation of this layer. The layer of $l = 7 \times 10^{-5}$ m in Isayev's (1983) experiments corresponds to $y/H = (H-l)/H = 0.945$. This is the position of the Δn minimum predicted in the present work, in full agreement with the experimental evidence.

5.4   Concluding Remarks

The contribution of frozen-in flow-induced stresses to the molecular orientation of injection molded parts has been examined. A finite element algorithm is presented for the solution of the fountain flow problem with the Leonov viscoelastic model. Finite element solutions are obtained at high levels of elasticity and they converge with mesh refinement, provided a slip boundary condition is employed to alleviate the stress singularity at the contact line. Calculation of stress profiles behind the advancing flow front and numerical tracking of material elements illustrate the effect of fountain flow on the deformation experienced by the fluid. Birefringence distributions are predicted and compare well with available experimental results. It is demonstrated quantitatively that fountain flow is responsible for the orientation pattern of the surface layer of injection molded parts.

CHAPTER 6

CONCLUSIONS AND RECOMMENDATIONS

Flow phenomena associated with the mold filling process have a significant impact on the final properties of injection molded parts. In the present thesis we employed finite element techniques and analyzed the fluid mechanics of mold filling and the effect of the flow conditions on the microstructure development in the molded part.

The mold filling process takes place as a rolling-type advancement of the flow front over the mold walls. The flow field behind the advancing flow front is known as fountain flow, and is the salient feature of mold filling. The fountain flow phenomenon was examined extensively with a finite element method in the steady-state. The u-v-p-h-δ formulation presented in Chapter 3 (also appendix A) is a powerful numerical technique for the simulation of free surface flows and determines simultaneously the flow field (velocities and pressure, u-v-p) and the free surface shape (h-δ parameters). Simulations with Newtonian and shear thinning fluids in planar and axisymmetric geometries were presented. Various features of the flow were described with the aid of velocity vector, pressure, free surface shape, and streamline plots. The effect of slip at the solid wall was also investigated.

The deformation experienced by the fluid due to fountain flow was examined by tracking material elements as they move through the flow domain. It was found that material elements from the centerline migrate towards the walls, extended in the flow direction and forming characteristic V-shapes, fully in agreement with the color tracer experiments of Schmidt (1974).

The general problem of two immiscible fluids displacing each other inside a capillary, i.e. fountain and reverse fountain flow, was also examined. A double-node finite

element method suitable for stratified multiphase flows was described. Simulations with this technique showed that a recirculating vortex appears adjacent to the interface and inside the less viscous fluid, as observed in the experiments of Dussan (1977).

An extension of the finite element technique for transient flows was presented in Chapter 4. Conditions for the contact line motion were derived and their finite element implementation was described. The technique was applied on the start-up flow of a fluid with a free front, in planar and axisymmetric geometries. Good agreement was found with available experimental results for the axisymmetric case (Behrens, 1983). The computational results show that for purely viscous fluids the flow development is completed within a short distance, and the same features of steady fountain flow are present, thus providing further support to the results of the steady-state analysis.

The transient finite element algorithm was also employed to investigate the collision of two flow fronts to form a weldline. It was found that during the collision phase the material elements are stretched and oriented in the transverse direction and oriented parallel to the weldline. However, this stretching is superimposed on a much larger deformation due to fountain flow that preceded the collision. Thus, it appears that fountain flow is mostly responsible for the observed anisotropy near weldlines of injection molded parts.
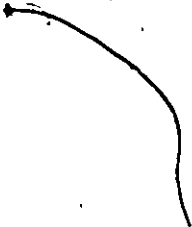
A quantitative evaluation of the effect of fountain flow on the molecular orientation of injection molded parts was undertaken in Chapter 5. The viscoelastic nature of the polymer melt is of primary importance for this purpose and must be accounted for with an appropriate constitutive equation. The multi-mode Leonov viscoelastic model was selected; this model describes well the rheological behavior of polymer melts and yet it has an attractively simple form. A finite element technique for viscoelastic free-surface flows with the Leonov viscoelastic model was described. Fountain flow simulations were performed for material properties and processing conditions corresponding to available experiments. Finite

element solutions were obtained at high levels of elasticity and they converged with mesh refinement, provided a slip boundary condition was applied at the wall to alleviate the stress singularity at the contact line. The calculated stress field was combined with a simple theory to predict frozen-in flow birefringence. Predictions were compared to, and showed good agreement with, published experimental birefringence measurements. It was demonstrated that fountain flow is responsible for the molecular orientation pattern of the surface layer of injection molded parts.

The finite element methodology adopted in the present work proved to be an extremely powerful tool in analyzing small scale fluid mechanical details associated with mold filling, and their impact on the molecular orientation of injection molded parts. Further work with this technique is recommended in the following areas:

(i)   Refinement of the model for predicting frozen-in flow birefringence. This calls for a fully transient and non-isothermal modeling of mold filling, as opposed to the decoupled approach adopted in Chapter 5. The computational cost is expected to be very large, and it may necessitate further improvement of the numerical technique itself, e.g. with the use of adaptive finite elements in order to minimize the required grid density for a given accuracy.

(ii)   Weldline formation. Application of the refined model to predict weldline strength. There is also the need for planned experiments on weldline formation and a better understanding of the physics of bonding of polymer-polymer interfaces.

(iii)   Inclusion of compressibility effects. This requires the use of an appropriate equation of state, and a viscoelastic model for compressible fluids, and will enable the investigation of the packing stage and the effect of packing pressure on the frozen-in birefringence. A notable area of application is the manufacture of

compact disks for which a coordinated attack by theory and experiment is highly desirable.

(iv)   Considerations of morphology in semicrystalline polymers, three dimensional effect and complicated mold shapes.

REFERENCES

Atkinson, A.O., "Design for manufacturability: computer-integrated design and manufacturing for plastic product development", Adv. Polym. Tech., 6, 117 (1986)

Bakerdjian, Z., and Kamal, M.R., "Distribution of some physical properties in injection-molded thermoplastic parts", Polym. Eng. Sci., 17, 96 (1977)

Ballman, R.L., Shusman, T., and Toor, H.L., "Injection molding. Flow of a molten polymer into a cold cavity", Ind. Eng. Chem., 51, 847 (1959a)

Ballman, R.L., Shusman, T., and Toor, H.L., "Injection molding : a rheological interpretation - part I", Mod. Plast., 37(Sep.), 105 (1959b)

Ballman, R.L., Shusman, T., and Toor, H.L., "Injection molding : a rheological interpretation - part II", Mod. Plast., 37(Oct.), 115 (1959c)

Ballman, R.L., and Shusman, T., "Easy way to calculate injection molding set-up time", Mod. Plast., 37(Nov.), 126 (1959)

Ballman, R.L., and Toor, H.L., "Orientation in Injection Molding", Mod. Plast., 38(Oct.), 113 (1960)

Bangert, H., and Menges,G., "Systematic design of injection molds and use of computers", Polym. Eng. Rev., 1, 134 (1981)

Baskharone, E., and Hamed, A., "A New Approach in Cascade Flow Analysis Using the Finite Element Method", AIAA J., 19, 65 (1981)

Behrens, R.A., "Transient domain free surface flows and their applications to mold filling", Ph.D. Thesis, Univ. Delaware, Delaware (1983)

Behrens, R.A., Crochet, M.J., Denson, C.D., and Metzner, A.B., "Transient free-surface flows : motion of a fluid advancing in a tube", AIChE J., 33, 1178 (1987)

Berger, J.L., and Gogos, C.G., "A numerical simulation of the cavity filling process with PVC in injection molding", Polym. Eng. Sci., 13, 102 (1973)

Beris, A.N., "Fluid elements deformation behind an advancing flow front", J. Rheol., 31, 121 (1987)

Bernhardt, E.C., Ed., "CAE, Computer Aided Engineering for Injection Molding", Hanser, Munich (1983)

Bhattacharji, S., and Savic, P., "Real and apparent non-Newtonian behavior in viscous pipe flow of suspensions driven by a fluid piston", Proc. Heat Transf. Fluid Mech. Inst., 248 (1965)

Bigg, D.M., "Application of the Marker-and-Cell technique to polymer processing problems", SPE ANTEC Tech. Papers, 21, 301 (1975)

Bird, R.B., Armstrong, R.C., and Hassager, O., "Dynamics of Polymeric Liquids", Vol. 1, p. 210, Wiley, New York (1977)

Broyer, E., Gutfinger, C., and Tadmor, Z., "A theoretical model for the cavity filling process in injection molding", Trans. Soc. Rheol., 19, 423 (1975)

Brown, R.A., Scriven, L.E., and Silliman, W.J., "Computer-aided analysis of nonlinear problems in transport phenomena", in "New Approaches to Nonlinear Problems in Dynamics", P. Holmes, Ed., SIAM, Philadelphia, p.298 (1980)

Castro, J.W., and Macosko, C.W., "Studies of mold filling and curing in the reaction injection molding process", AIChE J., 28, 250 (1982)

Chauffoureaux, J.C., Dehennau, C., and Van Rijckevorsel, J., "Flow and Thermal Stability of Rigid PVC", J. Rheol., 23, 1 (1979)

Chu, E.S., Goyal, S.K., and Kamal, M.R., "Prediction of microstructure development during injection mold filling", SPE ANTEC Tech. Papers, 45, 280 (1987)

Couniot, A., and Crochet, M.J., "Finite elements for the numerical simulation of injection molding", in "NUMIFORM 86, Numerical Methods in Industrial Forming Processes", K. Mattiason et al., Eds., Balkema, Rotterdam (1986)

Cox, G.L., Fix, G.J., and Gunzburger, M.D., "A least-squares finite element scheme for transonic flow around harmonically oscillating wings", Report No. 19, ICASE NASA Langley Research Center, Hampton, VA (1982)

Coyle, D.J., Blake, J.W., and Macosko, C.W., "The kinematics of fountain flow in mold filling", AIChE J., 33, 1168 (1987)

Crochet, M.J., and Keunings, R., "Die swell of a Maxwell fluid.: numerical prediction", J. Non-Newt. Fluid Mech., 7, 199 (1980)

Crochet, M.J., Davies, A.R., and Walters, K., "Numerical Simulation of Non-Newtonian Flow", Elsevier, Amsterdam (1984)

Dheur, J., and Crochet, M.J., "Numerical simulation of coextrusion", 2nd Ann. Meet. Polym. Processing Soc., Montreal, (Apr., 1986)

Dietz, W., White, J.L., and Clark, E.S., "Orientation development and relaxation in injection molding of amorphous polymers", Polym. Eng. Sci., 18, 273 (1978)

Dietz, W., and White, J.L., "Ein einfaches Modell zur Berechnung des Druckverlustes während des Werkzeugfüllvorganges und der eingefrorenen Orientierung beim Spritzgießen amorpher Kunststoffe", Rheol. Acta, 17, 676 (1978)

Dussan V., E.B., "Immiscible liquid displacement in a capillary tube : the moving contact line", AIChE J., 23, 131 (1977)

Dussan V, E.B., "On the spreading of liquids on solid surfaces : static and dynamic contact lines", Ann. Rev. Fluid Mech., 11, 371 (1979)

Duvaut, G., "Resolution d'un probleme de Stefan", C.R. Acad. Sci. Paris Ser. A, 276, 1461 (1973)

Elliot, C.M., "The numerical solution of an electrochemical machining moving boundary problem via a variational inequality formulation", J. Inst. Math. Appl., 25, 121 (1980)

Elliot, C.M., and Janovsky, V., "A finite element discretization of a variational inequality formulation of a Hele-Shaw moving boundary problem", Proc. of MAFELAP 1978, J.R. Whiteman, Ed., Academic, London (1979)

Elliot, C.M., and Janovsky, V., "A variational inequality approach to Hele-Shaw flow with a moving boundary", Proc. Roy. Soc. Edinburgh, 88A, 93 (1981)

Engelman, M.S., Strang, G., and Bathe, K.J., "The application of quasi-Newton methods in fluid mechanics", Int. J. Num. Meth. Eng., 17, 707 (1981)

Ferry, J.D., "Viscoelastic properties of polymers", 2nd Edition, Wiley, New York (1970)

Finlayson, B.A., "The method of weighted residuals and variational principles", Academic, New York (1972)

Fleissner, M., "Makroskopische und molekulare orientierung in hochpolymeren", Kolloid Z., 251, 1006 (1973)

Gilmore, G.D., and Spencer, R.S., "Role of temperature, pressure and time in the injection molding process", Mod. Plast., 27(Apr.), 143 (1950)

Gilmore, G.D., and Spencer, R.S., Mod. PLast., 28(Apr.), 117 (1951)

Givler, R.C., Crochet, M.J., and Pipes, R.B., "Numerical prediction of fiber orientation in dilute suspensions", J. Comp. Mater., 17, 330 (1983)

Gresho, P.M., Lee, R.L., and Sani, R.L., "On the time-dependent solution of the incompressible Navier-Stokes equations in two and three dimensions", in "Recent Advances in Numerical Methods in Fluids", Vol. 1, C. Taylor and K. Morgan, Eds., Pineridge Press, Swansea, U.K. (1979)

Hagerman, E.M., "Weldline fracture in molded parts", Plastics Eng., 29, 67 (1973)

Han, C.D., "Rheology in Polymer Processing", Academic, New York (1976)

Harry, D.H., and Parrott, R.C., "Numerical simulation of injection mold filling", Polym. Eng. Sci., 10, 209 (1970)

Hieber, C.A., and Shen, S.F., "A finite element / finite difference simulation of the injection molding filling process", J. Non-Newt. Fluid Mech., 7, 1 (1980)

Hieber, C.A., "Coupled flow path method for simulating the injection molding filling stage", SPE ANTEC Tech Papers, 28, 356 (1982)

Hieber, C.A., Socha, L.S., Shen, S.F., Wang, K.K., and Isayev, A.I., "Filling thin cavities of variable gap thickness: a numerical and experimental investigation", Polym. Eng. Sci., 23, 20 (1983)

Huang, C.F., "Simulations of the cavity filling process with the Marker-and-Cell method in injection molding", Ph.D. Thesis, Stevens Institute of Technology, Hoboken, N.J. (1978)

Huang, C.F., Gogos, C.G., and Schmidt, R.L., "The process of cavity filling including the fountain flow in injection molding", Polym. Eng. Sci., 26, 1457 (1986)

Huebner, K.H., and Thornton, E.A., "The finite element method for engineers", 2nd Edition, Wiley, New York (1982)

Huh, C., and Mason, S.G., "The steady movement of a capillary meniscus in a capillary tube", J. Fluid Mech., 81, 401 (1977)

Huh, C., and Scriven, L.E., "Hydrodynamic model of steady movement of a solid/liquid/fluid contact line", J. Colloid Interf. Sci., 35, 85 (1971)

Huilgol, R.R., and Phan-Thien, N., "Recent advances in the continuum mechanics of viscoelastic liquids", Int. J. Eng. Sci., 24, 161 (1986)

Isaacson, E., and Keller, H.B., "Analysis of Numerical Methods", Wiley, New York (1966)

Isayev, A.I., "Orientation development in the injection molding of amorphous polymers", Polym. Eng. Sci., 23, 271 (1983)

Isayev, A.I., and Hieber, C.A., "Toward a viscoelastic modeling of the injection molding of polymers", Rheol. Acta, 19, 168 (1980)

Isayev, A.I., and Hieber, C.A., "Oscillatory shear flow of polymeric systems", J. Polym. Sci., Polym. Phys. Ed., 20, 423 (1982)

Isayev, A.I., and Hariharan, T., "Volumetric effects in the injection molding of polymers", Polym. Eng. Sci., 25, 271 (1985)

Isayev, A.I., and Upadhyay, R.K., "Two-dimensional viscoelastic flows: experimentation and modeling", J. Non-Newt. Fluid Mech., 19, 135 (1985)

Janeschitz-Kriegl, H., "Injection moulding of plastics: some ideas about the relationship between mould filling and birefringence", Rheol. Acta, 16, 327 (1977)

Janeschitz-Kriegl, H., "Injection moulding of plastics II. Analytical solution of heat transfer problem", Rheol. Acta, 18, 693 (1979)

Janeschitz-Kriegl, H., "Polymer melt rheology and flow birefringence", Springer-Verlag, Berlin (1983)

Kafka, F.Y., and Dussan V., E.B., "On the interpretation of contact angles in capillaries", J. Fluid Mech., 95, 539 (1979)

Kalika, D.S., and Denn, M.M., "Wall slip and extrudate distortion in linear low-density polyethylene", J. Rheol., 31, 815 (1987)

Kamal, M.R., and Kenig, S., "The injection molding of thermoplastics, part I : theoretical model", Polym. Eng. Sci., 12, 295 (1972a)

Kamal, M.R., and Kenig, S., "The injection molding of thermoplastics, part II : experimental test of the model", Polym. Eng. Sci., 12, 302 (1972b)

Kamal, M.R., Kuo, Y., Doan, P.H., "The injection molding behavior of thermoplastics in thin rectangular cavities", Polym. Eng. Sci., 15, 863 (1975)

Kamal, M.R., Tan, V., and Ryan, M.E., "Injection molding : a critical profile", in Proc. of the International Conference on Polymer Processing, p. 34, MIT, N.P. Suh and N.H. Sung, Eds., Cambridge, MA (1977)

Kamal, M.R., and Tan, V., "Orientation in injection molded polystyrene", Polym. Eng. Sci., 19, 558 (1979)

Kamal, M.R., Chu, E., Lafleur, P.G., and Ryan, M.E., "Computer simulation of injection mold filling for viscoelastic melts with fountain flow", SPE ANTEC Tech. Papers, 31, 818 (1985)

Kamal, M.R., Goyal, S.K., and Chu, E., "Simulation of injection mold filling of viscoelastic polymer with fountain flow", AIChE J., 34, 94 (1988)

Karagiannis, A., Mavridis, H., Hrymak, A.N., and Vlachopoulos, J., "A finite element convergence study for shear thinning flow problems", Int. J. Num. Meth. Fluids, 8, 123 (1988)

Katti, S.S., and Schultz, J.M., "The microstructure of injection-molded semicrystalline polymers : a review", Polym. Eng. Sci., 22, 1001 (1982)

Keunings, R., "An algorithm for the simulation of transient viscoelastic flows with free surfaces", J. Comput. Phys., 62, 199 (1986a)

Keunings, R., "On the High Weissenberg Number Problem", J. Non-Newt. Fluid Mech., 20, 209 (1986b)

Keunings, R., "Simulation of Viscoelastic Flow", in "Fundamentals of Computer Modeling for Polymer Processing", C.L. Tucker III, Ed., Carl Hanser Verlag, in press (1987)

Kheshgi, H.S., Basaran, O.A., Benner, R.E., Kistler, S.F., and Scriven, L.E., "Continuation in a parameter : experience with viscous and free surface flows", in Proc. of Third Int. Conf. Num. Meth. Laminar and Turbulent Flow, Seatle (1983)

Kheshgi, H.S., and Scriven, L.E., "Penalty finite element analysis of unsteady free surface flows", in "Finite Element Methods in Fluids", Vol. 5, R.H. Galagher et al., Eds., Wiley, New York (1984)

Kim, B.H., and Suh, N.P., "A study of isothermal simple shear flow followed by nonisothermal stress relaxation in a low thermal inertia molding", Polym. Plast. Tech. Eng., 26, 23 (1987)

Kistler, S.F., "The fluid mechanics of curtain coating and related viscous free surface flows with contact lines", Ph.D. Thesis, Univ. Minnesota, Minneapolis (1984)

Kistler, S.F., and Scriven, L.E., "Coating Flows", in "Computational Analysis of Polymer Processing", J.R.A. Pearson and S.M. Richardson, Eds., Applied Science Pub., London (1983)

Krueger, W.L., and Tadmor, Z., "Injection molding into a rectangular cavity with inserts", Polym. Eng. Sci., 20, 426 (1980)

Kuo, Y., and Kamal, M.R., "The fluid mechanics and heat transfer of injection mold filling of thermoplastic materials", AIChE J., 22, 661 (1976)

Lau, H.C. and Schowalter, W.R., "A model for adhesive failure of viscoelastic fluids during flow", J. Rheol., 30, 193 (1986)

Leonov, A.I., "Nonequilibrium thermodynamics and rheology of viscoelastic polymer media", Rheol. Acta, 15, 85 (1976)

Leonov, A.I., "On a class of constitutive equations for viscoelastic liquids", J. Non-Newt. Fluid Mech., 25, 1 (1987)

Liaw, B.M., Kobayashi, A.S., and Emery, A.F., "Double-noding technique for mixed-mode crack propagation studies", Int. J. Num. Meth. Eng., 20, 967 (1984)

Lipscomb, G.G., Keunings, R., and Denn, M.M., "Implications of boundary singularities in complex geometries", J. Non-Newt. Fluid Mech., 24, 85 (1987)

Lord, H.A., and Williams, G., "Mold filling studies for the injection molding of thermoplastics, part II : the transient flow of plastic materials in the cavities of injection molding dies", Polym. Eng. Sci., 15, 569 (1975)

Lynch, D.R., "A unified approach to simulation on deforming elements with application to phase change problems", J. Comput. Phys., 47, 387 (1982)

Mavridis, H., Hrymak, A.N., and Vlachopoulos, J., "Finite element simulation of fountain flow in injection molding", Polym. Eng. Sci., 26, 449 (1986a)

Mavridis, H., Hrymak, A.N., and Vlachopoulos, J., "Deformation and orientation of fluid elements behind an advancing flow front", J. Rheol., 30, 555 (1986b)

Mavridis, H., Hrymak, A.N., and Vlachopoulos, J., "Mathematical modeling of injection mold filling : a review", Adv. Polym. Tech., 6, 457 (1986c)

Mavridis, H., Hrymak, A.N., and Vlachopoulos, J., "Finite element simulation of stratified multiphase flows", AIChE J., 33, 410 (1987)

Mavridis, H., Hrymak, A.N., and Vlachopoulos, J., "Transient free surface flows in injection mold filling", AIChE J., 34, xxx (1988a)

Mavridıs, H., Hrymak, A.N., and Vlachopoulos, J., "The effect of fountain flow on molecular orientation in injection molding", J. Rheol., 32, xxx (1988b)

Menges, G., and Wübken, G., "Influence of processing conditions on molecular orientation of injection molds", Soc. Plastics Eng., 31st Annual Technical Conference, Montreal, Canada (1973)

Menges, G., Wübken, G., and Horn, B., "Einflub der Verarbeitungsbedingungen auf die Kristallinität und Gefügestruktur teilkristalliner Spritzgubteile", Colloid Polym. Sci., 254, 267 (1976)

Menges, G., and Thienel, P., Kunststoffe, 65, 696 (1975)

Michael, D.H., "The separation of a fluid at a straight edge", Mathematika, 5, 82 (1958)

Middleman, S., "Fundamentals of Polymer Processing", McGraw-Hill, New York (1977)

Mirza, F.A., and Olson, M.D., "Energy convergence and evaluation of stress intensity factor K_I for stress singular problems", Int. J. Fracture, 14, 555 (1978)

Mitsoulis, E., "Finite element analysis of two-dimensional polymer melt flows", Ph.D. Thesis, McMaster Univ., Hamilton, Ont., Canada (1984)

Mitsoulis, E., and Vlachopoulos, J., "The finite element method for fluid flow and heat transfer analysis", Adv. Polym. Tech., 4, 107 (1985)

Nickell, R.E., Tanner, R.I., and Caswell, B., "The solution of viscous incompressible jet and free surface flows using finite element methods", J. Fluid Mech., 65, 189 (1974)

Pearson, J.R.A., "Mechanical Principles of Polymer Melt Processing", Pergamon, Oxford (1966)

Pearson, J.R.A., "Mechanics of Polymer Processing", Elsevier, London (1985)

Pismen, L.M., and Nir, A., "Motion of a contact line", Phys. Fluids, 25, 3 (1982)

Ramamurthy, A.V., "Wall slip in viscous fluids and influence of materials of construction", J. Rheol., 30, 337 (1986)

Reddy, K.R., and Tanner, R.I., "On the swelling of extrudate plane sheets", J. Rheol., 22, 661 (1978)

Richardson, S.M., "Hele Shaw flows with a free boundary produced by the injection of fluid into a narrow channel", J. Fluid Mech., 56, 609 (1972)

Richardson, S.M., Pearson, H.J., and Pearson, J.R.A., "Simulation of injection molding", Plast. Rubber Process., 5, 55 (1980)

Rose, W., "Fluid-fluid interfaces in steady motion", Nature, 191, 242 (1961)

Ryan, M.E., and Chung, T.S., "Conformal mapping analysis of injection mold filling", Polym. Eng. Sci., 20, 642 (1980)

Sang-Gook, K., and Suh, N.P., "Performance prediction of weldline structure in amorphous polymers", Polym. Eng. Sci., 26, 1200 (1986)

Schacht, Th., Maler, U., Esser, K., Kretzschmar, O., and Schmidt, Th., "CAE/CAD in injection molding, blow molding and foam molding : the shortest way to mold design", Adv. Polym. Tech., 5, 99 (1985)

Schlichting, H., "Boundary Layer Theory", 4th Edition, McGraw-Hill, New York (1960)

Schmidt, L.R., "A special mold and tracer technique for studying shear and extensional flows in a mold cavity during injection molding", Polym. Eng. Sci., 14, 797 (1974)

Schmidt, L.R., "Experimental studies of injection-mold filling", in Proc. of the International Conference on Polymer Processing, p. 315, MIT, N.P. Suh and N.H. Sung, Eds., Cambridge, MA (1977)

Schmidt, L.R., "The interrelationship of flow, structure and properties in injection molding", in Proc. 2nd World Congress Chem. Eng., Vol. VI, p. 516, Montreal, Canada (1981)

Schwartz, A.M., Rader, C.A., and Huey, E., in "Contact Angles, Wettability and adhesion ", p. 250, R.F. Could, Ed., American Chemical Society, Washington, D.C., (1964)

Shen, S.F., "Simulation of polymeric flows in the injection moulding process", Int. J. Num. Meth. Fluids, 4, 171 (1984)

Silliman, W.J., and Scriven, L.E., "Separating flow near a static contact line : slip at a wall and shape of a free surface", J. Comput. Phys., 34, 287 (1980)

Spencer, R.S., and Gilmore, G.D., Mod. Plast., 28(Dec.), 97 (1950)

Spencer, R.S., and Gilmore, G.D., "Some flow phenomena in the injection molding of polystyrene", J. Colloid Interf. Sci., 6(Dec.), 118 (1951)

Strang, G., and Fix, G.J., "An analysis of the finite element method", Prentice-Hall, N.J. (1973)

Tadmor, Z., "Molecular Orientation in Injection Molding", J. Appl. Polym. Sci., 18, 1753 (1974)

Tadmor, Z., Broyer, E., and Gutfinger, C., "Flow analysis network (FAN) - A method for solving flow problems in polymer processing", Polym. Eng. Sci., 14, 660 (1974)

Tadmor, Z., and Gogos, C.G., "Principles of Polymer Processing", Wiley, New York (1979)

Taylor, C., and Hughes, T., "Finite element modeling of the Navier-Stokes equations", Pineridge Press, Swansea, U.K. (1981)

Thienel, P., and Menges, G., "Mathematical and experimental determination of temperature, velocity and pressure fields in flat molds during the filling process in injection molding of thermoplastics", Polym. Eng. Sci., 18, 314 (1978)

Toor, H.L., Ballman, R.L., and Cooper, L., "Predicting mold flow by electronic computer", Mod. Plast., 38(Dec.), 117(1960)

Upadhyay, R.K., "Study of bubble growth in foam injection molding", Adv. Polym. Tech., 5, 55 (1985)

Upadhyay, R.K., Isayev, A.I., and Shen, S.F., "Transient shear flow behavior of polymeric fluids according to the Leonov model", Rheol. Acta, 20, 443 (1981)

Upadhyay, R.K., Isayev, A.I., and Shen, S.F., "Modeling of stresses in multistep-shear deformation of polymeric liquids", J. Rheol., 27, 155 (1983)

Upadhyay, R.K., and Isayev, A.I., "Elongational flow behavior of polymeric fluids according to the Leonov model", Rheol. Acta, 22, 557 (1983)

Upadhyay, R.K., and Isayev, A.I., "Nonisothermal elongational flow of polymeric fluids according to the Leonov model", J. Rheol., 28, 581 (1984)

Upadhyay, R.K., and Isayev, A.I., "Simulation of two-dimensional planar flow of viscoelastic fluid", Rheol. Acta, 25, 80 (1986)

Van Wijngaarden, H., Dijksman, J.F., and Wesseling, P., "Non-isothermal flow of a molten polymer in a narrow rectangular cavity", J. Non-Newt. Fluid Mech., 11, 175 (1982)

Viriyayuthakorn, M., and Deboo, R.V., "A finite element model for cable jacketing simulation", SPE ANTEC Tech. Papers, 41, 178 (1983)

Wales, J.L.S., Van Leeuwen, J., and Van Der Vijgh, R., "Some aspects of orientation in injection molded objects", Polym. Eng. Sci., 12, 358 (1972)

Wales, J.L.S., "The application of flow birefringence to rheological studies of polymer melts", Delft University Press (1976)

Wang, K.K. et al., "Cornell Injection Molding Project", in Proc. of the International Conference on Polymer Processing, p. 293, MIT, N.P. Suh and N.H. Sung, Eds., Cambridge, MA (1977)

Wang, K.K. et al., "Computer-Aided Injection Molding System", Report 5, Cornell Univ. (1978)

Wang, K.K. et al., "Computer-Aided Injection Molding System", Report 6, Cornell Univ. (1979)

Wang, K.K. et al., "Computer-Aided Injection Molding System", Report 11, Cornell Univ. (1985)

West, G.D., "On the resistance to the motion of a thread of mercury in a glass tube", Proc. Roy. Soc. London Ser. A, 86, 20 (1911)

White, J.L., "Fluid mechanical analysis of injection molding", Polym. Eng. Sci., 15, 44 (1975)

White, J.L., and Dietz, W., "Considerations of the freezing-in of flow-induced orientation in polymer melts by vitrification with application to processing", J. Non-Newt. Fluid Mech., 4, 299 (1979)

Williams, G., and Lord, H.A., "Mold filling studies for the injection molding of thermoplastics, part I : the flow of plastic materials in hot- and cold-walled circular channels", Polym. Eng. Sci., 15, 553 (1975)

Wu, P.C., Huang, C.F., and Gogos, C.G., "Simulation of the mold filling process", Polym. Eng. Sci., 14, 223 (1974)

Yarnold, G.D., "The motion of a mercury index in a capillary tube", Proc. Phys. Soc. (London), 50, 540 (1938)

Zienkiewicz, O.C., "The finite element method", 3rd Edition, McGraw-Hill, New York (1977)

APPENDIX A

The Finite Element Equations for u-v-p-h-δ

Formulation of Free-Surface Flow

The Galerkin weighted residual equations for u-v-p-h-δ formulation of free surface flow derived in Section 3.2.2 (eqs. 3.14-17) are:

$$R^i_m = \int_\Omega \{\phi^i \, Re \, V \cdot \nabla V + \nabla \phi^i \cdot \sigma - \phi^i S^{-1} g\} d\Omega - \int_{\partial\Omega} n \cdot \sigma \, \phi^i \, d\ell = 0 \qquad (A.1)$$

$$R^i_c = \int_\Omega \nabla \cdot V \, n^i \, d\Omega = 0 \qquad (A.2)$$

$$R^i_k = \int_{F.S.} n \cdot V \, \phi^i(\xi, \eta = 1) \, d\ell = 0 \qquad (A.3)$$

$$R^i_\delta = \int_{-1}^{0} (x^2_\xi + y^2_\xi)^{1/2}_{|\eta=1} \, d\xi - \int_0^1 (x^2_\xi + y^2_\xi)^{1/2}_{|\eta=1} \, d\xi = 0 \qquad (A.4)$$

The finite element basis functions $\phi^i(\xi,\eta)$ and $n^i(\xi,\eta)$ are defined in terms of the local coordinates ξ-η over the parent element onto which the deformed element is mapped isoparametrically. The 9-node quadrilateral and 6-node triangular elements used in this work and their isoparametric transformations are shown in Figure A.1. The explicit form of the finite element basis functions is given in Table A.1.

The $(x,y) \longleftrightarrow (\xi,\eta)$ isoparametric transformation is (Strang & Fix, 1973; Zienkiewicz, 1977):

$$x = \sum_{j=1}^{N_e} x^j \, \phi^j(\xi, \eta), \qquad y = \sum_{j=1}^{N_e} y^j \, \phi^j(\xi, \eta) \qquad (A.5)$$

where x^j, y^j are the coordinates of the nodal points and N_e is the number of nodes per element.
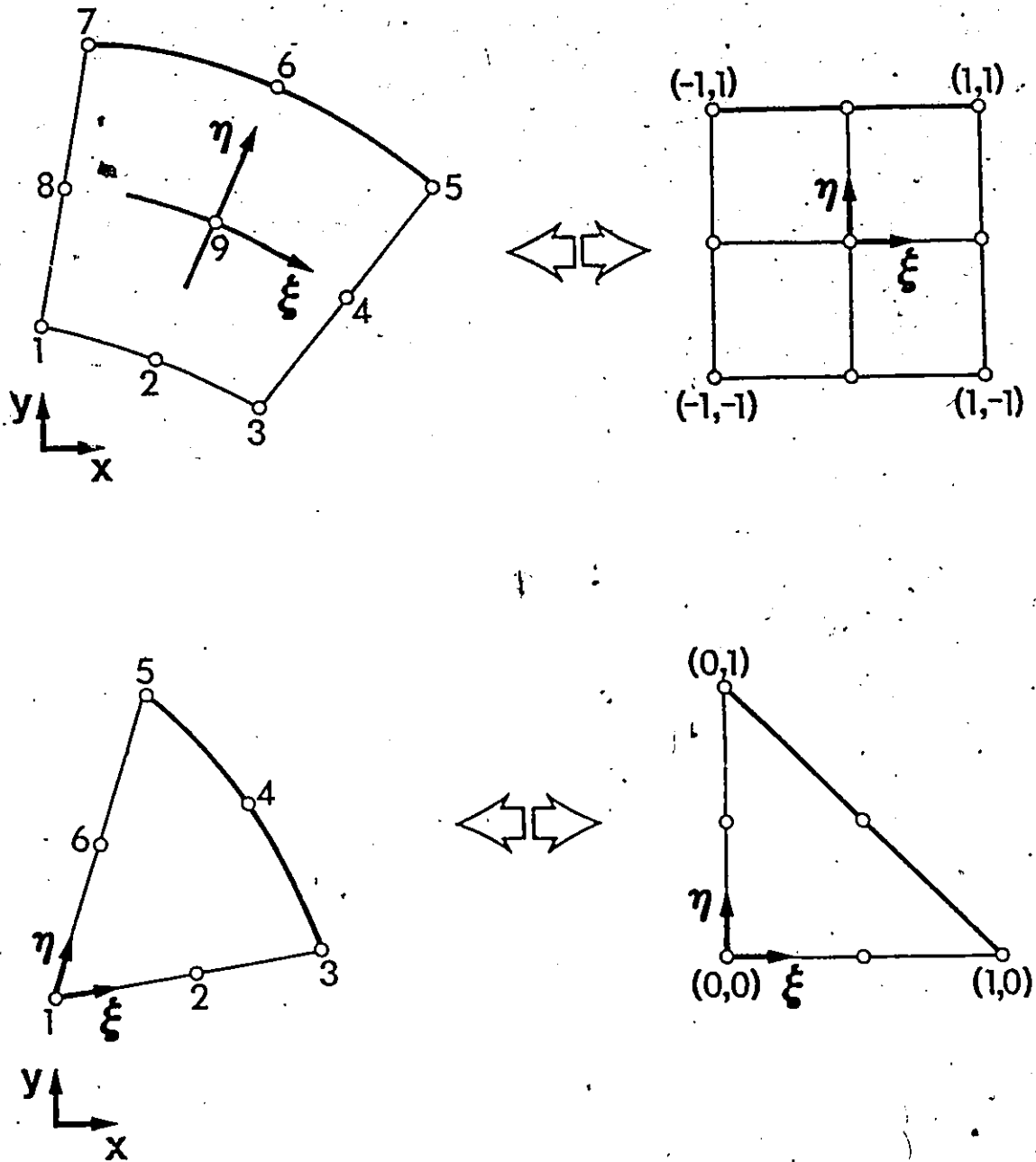
171

Figure A.1   9-node quadrilateral and 6-node triangular finite elements and their isoparametric transformations

Table A.1   Basis functions for 9-node and 6-node elements

9-node quadrilateral

6-node triangular

$\phi^1 = \frac{1}{4}(\xi - \xi^2)(\eta - \eta^2)$ $n^1 = \frac{1}{4}(1-\xi)(1-\eta)$ $\phi^1 = 1 - 3\xi - 3\eta + 2\xi^2 + 4\xi\eta + 2\eta^2$

$\phi^2 = -\frac{1}{2}(1-\xi^2)(\eta - \eta^2)$ $n^3 = \frac{1}{4}(1+\xi)(1-\eta)$ $\phi^2 = 4(\xi - \xi^2 - \xi\eta)$

$\phi^3 = -\frac{1}{4}(\xi + \xi^2)(\eta - \eta^2)$ $n^5 = \frac{1}{4}(1+\xi)(1+\eta)$ $\phi^3 = 2\xi^2 - \xi$

$\phi^4 = \frac{1}{2}(\xi + \xi^2)(1 - \eta^2)$ $n^7 = \frac{1}{4}(1-\xi)(1+\eta)$ $\phi^4 = 4\xi\eta$

$\phi^5 = \frac{1}{4}(\xi + \xi^2)(\eta + \eta^2)$ $\phi^5 = 2\eta^2 - \eta$

$\phi^6 = \frac{1}{2}(1-\xi^2)(\eta + \eta^2)$ $\phi^6 = 4(\eta - \xi\eta - \eta^2)$

$\phi^7 = -\frac{1}{4}(\xi - \xi^2)(\eta + \eta^2)$ $n^1 = 1 - \xi - \eta$

$\phi^8 = -\frac{1}{2}(\xi - \xi^2)(1 - \eta^2)$ $n^3 = \xi$

$\phi^9 = (1-\xi^2)(1-\eta^2)$ $n^5 = \eta$

The evaluation of the integrals in the residuals and the corresponding Jacobian entries is performed with Gaussian quadrature over the parent element. Area and line integrals over the physical (x,y) domain are transformed to integrals in the computational (ξ,η) domain with the aid of the following relations resulting from the isoparametric map:

$$d\Omega = dx\,dy = |J|\,d\xi\,d\eta \qquad (A.6)$$

$$d\ell = (x_\xi^2 + y_\xi^2)^{1/2}\big|_{\eta=1}\,d\xi \qquad (A.7)$$

where $|J| = x_\xi y_\eta - x_\eta y_\xi$ is the determinant of the Jacobian of the $(x,y)\longleftrightarrow(\xi,\eta)$ transformation.

The limits of integration of the Galerkin weighted residual equations are freed from any dependence on free surface location with eqs. (A.6), (A.7). Any such dependence of derivatives in the integrands can also be removed with:

$$\frac{\partial}{\partial x} = \frac{1}{|J|}\left(y_\eta \frac{\partial}{\partial \xi} - y_\xi \frac{\partial}{\partial \eta}\right) \qquad (A.8)$$

$$\frac{\partial}{\partial y} = \frac{1}{|J|}\left(-x_\eta \frac{\partial}{\partial \xi} + x_\xi \frac{\partial}{\partial \eta}\right) \qquad (A.9)$$

The isoparametric map also offers convenient evaluation of the unit normal and tangential vectors to the free surface:

$$\mathbf{n} = \frac{-y_\xi \mathbf{e}_x + x_\xi \mathbf{e}_y}{(x_\xi^2 + y_\xi^2)^{1/2}}\bigg|_{\eta=1} \qquad (A.10)$$

$$\mathbf{t} = \frac{x_\xi \mathbf{e}_x + y_\xi \mathbf{e}_y}{(x_\xi^2 + y_\xi^2)^{1/2}}\bigg|_{\eta=1} \qquad (A.11)$$

The explicit expressions of the Galerkin weighted residual equations and the corresponding Jacobian entries are listed in Table A.2. These expressions were implemented into a computer program that utilizes the frontal technique (Taylor & Hughes, 1981) to assemble and solve the equations. The code consists of approximately 3500 FORTRAN lines. Typical problem sizes and run times are given in Table 3.1 of Section 3.2.3.1.

The Newton-Raphson iterative scheme was employed for the solution of the nonlinear algebraic set of equations. The frontal solver calls sequentially an element routine which evaluates the contributions of this element to the global Jacobian matrix and vector of residuals. The correctness of the Jacobian matrix is crucial for the Newton-Raphson scheme. A particularly useful way to check for the correctness of the Jacobian and identify possible differentiation or implementation mistakes is to compare an element Jacobian matrix with its finite difference analog. The element Jacobian J_e is:

$$(J_e)_{ij} \equiv \partial R_e^i / \partial X_e^j \qquad (A.12)$$

where R_e and X_e are the vectors of residuals and unknowns respectively at the element level. The Jacobian entries $(J_e)_{ij}$ are listed in Table A.2. The central finite difference analog of eq. (A.12) is:

$$(J_e')_{ij} = \frac{R_e^i(X_e^j + \Delta X_e^j) - R_e^i(X_e^j - \Delta X_e^j)}{2\Delta X_e^j} \qquad (A.13)$$

For a small perturbation ΔX_e (e.g. $\Delta X_e = 0.001\ X_e$) eq. (A.13) provides an accurate approximation to the exact Jacobian. Comparison of $(J_e)_{ij}$ and $(J_e')_{ij}$ will then identify any incorrect entries.

Table A.2 Galerkin Weighted Residual Equations and Jacobian Entries

<u>Preliminaries</u>

$$u = \sum_i \phi^i u^i, \quad v = \sum_i \phi^i v^i, \quad P = \sum_i \pi^i P^i, \quad x = \sum_i \phi^i x^i, \quad y = \sum_i \phi^i y^i$$

$$u_\xi = \sum_i \phi_\xi^i u^i, \quad v_\xi = \sum_i \phi_\xi^i v^i, \quad x_\xi = \sum_i \phi_\xi^i x^i, \quad y_\xi = \sum_i \phi_\xi^i y^i$$

$$u_\eta = \sum_i \phi_\eta^i u^i, \quad v_\eta = \sum_i \phi_\eta^i v^i, \quad x_\eta = \sum_i \phi_\eta^i x^i, \quad y_\eta = \sum_i \phi_\eta^i y^i$$

$$|J| = x_\xi y_\eta - x_\eta y_\xi, \quad \xi_x = y_\eta / |J|, \quad \xi_y = -x_\eta / |J|, \quad \eta_x = -y_\xi / |J|, \quad \eta_y = x_\xi / |J|$$

$$\phi_x^i = \phi_\xi^i \xi_x + \phi_\eta^i \eta_x, \quad u_x = u_\xi \xi_x + u_\eta \eta_x, \quad v_x = v_\xi \xi_x + v_\eta \eta_x$$

$$\phi_y^i = \phi_\xi^i \xi_y + \phi_\eta^i \eta_y, \quad u_y = u_\xi \xi_y + u_\eta \eta_y, \quad v_y = v_\xi \xi_y + v_\eta \eta_y$$

$$|\dot{\gamma}| = [2u_x^2 + 2v_y^2 + (u_y + v_x)^2]^{1/2}, \quad \mu = \mu(|\dot{\gamma}|)$$

$$\frac{\partial \mu}{\partial u^j} = \frac{\partial \mu}{\partial |\dot{\gamma}|} \left[\frac{2u_x}{|\dot{\gamma}|} \phi_x^j + \frac{(u_y + v_x)}{|\dot{\gamma}|} \phi_y^j \right]$$

$$\frac{\partial \mu}{\partial v^j} = \frac{\partial \mu}{\partial |\dot{\gamma}|} \left[\frac{(u_y + v_x)}{|\dot{\gamma}|} \phi_x^j + \frac{2v_y}{|\dot{\gamma}|} \phi_y^j \right]$$

Table A.2 (continued)

x-Momentum Equation

$$R^i_{mx} = \int_{-1}^{1} \int_{-1}^{1} \{(-P+2\mu u_x)\phi^i_x + \mu(u_y+v_x)\phi^i_y + Re\,\phi^i(uu_x+vu_y) - S^{-1}g_x\phi^i\}|J|\,d\xi\,d\eta$$

$$\frac{\partial R^i_{mx}}{\partial u^j} = \int_{-1}^{1} \int_{-1}^{1} \{\mu(2\phi^i_x\phi^j_x+\phi^i_y\phi^j_y) + [2u_x\phi^i_x+(u_y+v_x)\phi^i_y]\frac{\partial \mu}{\partial u^j} + Re\,\phi^i(u_x\phi^j+u\phi^j_x+v\phi^j_y)\}$$

$$\cdot |J|\,d\xi\,d\eta$$

$$\frac{\partial R^i_{mx}}{\partial v^j} = \int_{-1}^{1} \int_{-1}^{1} \{\mu\phi^i_y\phi^j_x + [2u_x\phi^i_x+(u_y+v_x)\phi^i_y]\frac{\partial \mu}{\partial v^j} + Re\,\phi^i\phi^j u_y\}|J|\,d\xi\,d\eta$$

$$\frac{\partial R^i_{mx}}{\partial P^j} = \int_{-1}^{1} \int_{-1}^{1} \{-\phi^i_x\,\pi^j\}|J|\,d\xi\,d\eta$$

Table A.2 (continued)

y-Momentum Equation

$$R^i_{my} = \int_{-1}^{1} \int_{-1}^{1} \{\mu(u_y + v_x)\phi^i_x + (-P + 2\mu v_y)\phi^i_y + \text{Re}\,\phi^i(uv_x + vv_y) - S^{-1}g_y\phi^i\}|J|\,d\xi\,d\eta$$

$$\frac{\partial R^i_{my}}{\partial u^j} = \int_{-1}^{1} \int_{-1}^{1} \{\mu\phi^i_x\phi^j_y + [(u_y + v_x)\phi^i_x + 2v_y\phi^i_y]\frac{\partial \mu}{\partial u^j} + \text{Re}\,\phi^i\phi^j v_x\}|J|\,d\xi\,d\eta$$

$$\frac{\partial R^i_{my}}{\partial v^j} = \int_{-1}^{1} \int_{-1}^{1} \{\mu(\phi^i_x\phi^j_x + 2\phi^i_y\phi^j_y) + [(u_y + v_x)\phi^i_x + 2v_y\phi^i_y]\frac{\partial \mu}{\partial v^j} + \text{Re}\,\phi^i(u\phi^j_x + \phi^j v_y + v\phi^j_y)\}$$

$$\cdot |J|\,d\xi\,d\eta$$

$$\frac{\partial R^i_{my}}{\partial P^j} = \int_{-1}^{1} \int_{-1}^{1} \{-\phi^i_y\,\pi^j\}|J|\,d\xi\,d\eta$$

Table A.2 (continued)

Continuity Equation

$$R_c^i = \int_{-1}^{1} \int_{-1}^{1} \{u_x + v_y\} n^i |J| \, d\xi \, d\eta$$

$$\frac{\partial R_c^i}{\partial u^j} = \int_{-1}^{1} \int_{-1}^{1} \{\phi_x^j\} n^i |J| \, d\xi \, d\eta$$

$$\frac{\partial R_c^i}{\partial v^j} = \int_{-1}^{1} \int_{-1}^{1} \{\phi_y^j\} n^i |J| \, d\xi \, d\eta$$

Kinematic Equation

$$R_k^i = \int_{-1}^{1} \{-y_\xi u + x_\xi v\} \phi^i (\xi, \eta = 1) \, d\xi$$

$$\frac{\partial R_k^i}{\partial u^j} = \int_{-1}^{1} \{-y_\xi \phi^j\} \phi^i (\xi, \eta = 1) \, d\xi$$

$$\frac{\partial R_k^i}{\partial v^j} = \int_{-1}^{1} \{x_\xi \phi^j\} \phi^i (\xi, \eta = 1) \, d\xi$$

δ-Equation

$$R_\delta = \int_{-1}^{0} (x_\xi^2 + y_\xi^2)_{|\eta=1}^{1/2} \, d\xi - \int_{0}^{1} (x_\xi^2 + y_\xi^2)_{|\eta=1}^{1/2} \, d\xi$$

Table A.2 (continued)

<u>Free Surface Derivatives</u> (w.r.t. h_i. Similarly w.r.t. δ_i.)

$$\frac{\partial x_\xi}{\partial h^j} = \sum_i \phi_\xi^i \frac{\partial x^i}{\partial h^j}, \quad \frac{\partial x_\eta}{\partial h^j} = \sum_i \phi_\eta^i \frac{\partial x^i}{\partial h^j}, \quad \frac{\partial y_\xi}{\partial h^j} = \sum_i \phi_\xi^i \frac{\partial y^i}{\partial h^j}, \quad \frac{\partial y_\eta}{\partial h^j} = \sum_i \phi_\eta^i \frac{\partial y^i}{\partial h^j}.$$

$$\frac{\partial |J|}{\partial h^j} = y_\eta \frac{\partial x_\xi}{\partial h^j} + x_\xi \frac{\partial y_\eta}{\partial h^j} - y_\xi \frac{\partial x_\eta}{\partial h^j} - x_\eta \frac{\partial y_\xi}{\partial h^j}$$

$$\frac{\partial \xi_x}{\partial h^j} = \left(|J| \frac{\partial y_\eta}{\partial h^j} - y_\eta \frac{\partial |J|}{\partial h^j} \right) / |J|^2 \qquad \frac{\partial \xi_y}{\partial h^j} = -\left(|J| \frac{\partial x_\eta}{\partial h^j} - x_\eta \frac{\partial |J|}{\partial h^j} \right) / |J|^2$$

$$\frac{\partial \eta_x}{\partial h^j} = -\left(|J| \frac{\partial y_\xi}{\partial h^j} - y_\xi \frac{\partial |J|}{\partial h^j} \right) / |J|^2 \qquad \frac{\partial \eta_y}{\partial h^j} = \left(|J| \frac{\partial x_\xi}{\partial h^j} - x_\xi \frac{\partial |J|}{\partial h^j} \right) / |J|^2$$

$$DHPXJ \equiv \frac{\partial}{\partial h^j}(\phi_x^i |J|) = \phi_\xi^i \frac{\partial y_\eta}{\partial h^j} - \phi_\eta^i \frac{\partial y_\xi}{\partial h^j}$$

$$DHPYJ \equiv \frac{\partial}{\partial h^j}(\phi_y^i |J|) = -\phi_\xi^i \frac{\partial x_\eta}{\partial h^j} + \phi_\eta^i \frac{\partial x_\xi}{\partial h^j}$$

$$DHXX \equiv \frac{\partial u_x}{\partial h^j} = u_\xi \frac{\partial \xi_x}{\partial h^j} + u_\eta \frac{\partial \eta_x}{\partial h^j}$$

$$DHYY \equiv \frac{\partial v_y}{\partial h^j} = v_\xi \frac{\partial \xi_y}{\partial h^j} + v_\eta \frac{\partial \eta_y}{\partial h^j}$$

$$DHXY \equiv \frac{\partial}{\partial h^j}(u_y + v_x) = u_\xi \frac{\partial \xi_y}{\partial h^j} + u_\eta \frac{\partial \eta_y}{\partial h^j} + v_\xi \frac{\partial \xi_x}{\partial h^j} + v_\eta \frac{\partial \eta_x}{\partial h^j}$$

Table A.2 (continued)

$$\frac{\partial R^i_{mx}}{\partial h^j} = \int_{-1}^{1}\int_{-1}^{1}\left\{(-P + 2\mu u_x)\,DHPXJ + \mu(u_y + v_x)\,DHPYJ + \mu|J|\right.$$

$$\cdot(2\phi^i_x\,DHXX + \phi^i_y\,DHXY) + |J|\cdot VISCH\cdot[2u_x\phi^i_x + (u_y + v_x)\phi^i_y]$$

$$\left.+ Re\,\phi^i(u\cdot DHUXJ + v\cdot DHUYJ) - S^{-1}\phi^i g_x\frac{\partial|J|}{\partial h^j}\right\}d\xi\,d\eta$$

$$\frac{\partial R^i_{my}}{\partial h^j} = \int_{-1}^{1}\int_{-1}^{1}\left\{\mu(u_y + v_x)\,DHPXJ + (-P + 2\mu v_y)\,DHPYJ\right.$$

$$+ \mu|J|(\phi^i_x\,DHXY + 2\phi^i_y\,DHYY) + |J|\cdot VISCH\cdot[(u_y + v_x)\phi^i_x + 2v_y\phi^i_y]$$

$$\left.+ Re\,\phi^i(u\cdot DHVXJ + v\cdot DHVYJ) - S^{-1}\phi^i g_y\frac{\partial|J|}{\partial h^j}\right\}d\xi\,d\eta$$

$$\frac{\partial R^i_c}{\partial h^j} = \int_{-1}^{1}\int_{-1}^{1}\{DHUXJ + DHVYJ\}n^i\,d\xi\,d\eta$$

$$\frac{\partial R^i_k}{\partial h^j} = \int_{-1}^{1}\left\{-u\frac{\partial y_\xi}{\partial h^j} + v\frac{\partial x_\xi}{\partial h^j}\right\}\phi^i(\xi, \eta = 1)d\xi$$

$$\frac{\partial R_\delta}{\partial h^j} = \int_{-1}^{0}\left\{(x_\xi^2 + y_\xi^2)^{-\frac12}\left(x_\xi\frac{\partial x_\xi}{\partial h^j} + y_\xi\frac{\partial y_\xi}{\partial h^j}\right)\right\}\Bigg|_{\eta=1}d\xi$$

$$-\int_{0}^{1}\left\{(x_\xi^2 + y_\xi^2)^{-\frac12}\left(x_\xi\frac{\partial x_\xi}{\partial h^j} + y_\xi\frac{\partial y_\xi}{\partial h^j}\right)\right\}\Bigg|_{\eta=1}d\xi$$

Table A.2 (continued)

$$\text{VISCH} \equiv \frac{\partial \mu}{\partial h^j} = \frac{\partial \mu}{\partial |\dot{Y}|} \left[\frac{2u_x}{|\dot{Y}|} \text{DHXX} + \frac{2v_y}{|\dot{Y}|} \text{DHYY} + \frac{u_y + v_x}{|\dot{Y}|} \text{DHXY} \right]$$

$$\text{DHUXJ} \equiv \frac{\partial}{\partial h^j} (u_x |J|) = u_\xi \frac{\partial y_\eta}{\partial h^j} - u_\eta \frac{\partial y_\xi}{\partial h^j}, \quad \text{DHUYJ} \equiv \frac{\partial}{\partial h^j} (u_y |J|) = -u_\xi \frac{\partial x_\eta}{\partial h^j} + u_\eta \frac{\partial x_\xi}{\partial h^j}$$

$$\text{DHVXJ} \equiv \frac{\partial}{\partial h^j} (v_x |J|) = v_\xi \frac{\partial y_\eta}{\partial h^j} - v_\eta \frac{\partial y_\xi}{\partial h^j}, \quad \text{DHVYJ} \equiv \frac{\partial}{\partial h^j} (v_y |J|) = -v_\xi \frac{\partial x_\eta}{\partial h^j} + v_\eta \frac{\partial x_\xi}{\partial h^j}$$